공학박사 학위논문

Study on silicon-based MEMS acceleration switch with low threshold acceleration

낮은 임계 가속도를 가지는 실리콘 기반 MEMS 가속도 스위치에 관한 연구

2017 년 8 월

서울대학교 대학원

전기 컴퓨터 공학부

황 정 기

Study on silicon-based MEMS acceleration switch with low threshold acceleration

지도 교수 김 용 권

이 논문을 공학박사 학위논문으로 제출함
2017 년 8 월

서울대학교 대학원
전기 컴퓨터 공학부
황 정 기

황정기의 공학박사 학위논문을 인준함
2017 년 8 월

위 원 장 _____ (인)

부위원장 _____ (인)

위 원 _____ (인)

위 원 _____ (인)

위 원 _____ (인)

Abstract

In this paper, MEMS acceleration switch with low threshold acceleration below 10 g and fine environmental characteristics are developed. Limits of the previously reported low-g MEMS switches were addressed in terms of environmental test issues and the solutions for them were suggested and integrated in the proposed low-g MEMS acceleration switch. Fabrication process consists of one silicon-on-insulator substrate and two glass substrates for base and package, respectively. Single-crystalline silicon was chosen as the structural material for high thermal stability and stress-free structure. After the fabrication, height profiles of the free-hanging proof masses were measured to show that the fabricated switches does not suffer from stress problems. The size of single switch was measured as 2150 x 4240 x 1180 μm^3 and the average proof mass, initial gap, and the spring constant was 307.38 μg, 6.39 μm, and 3.29 N/m, respectively. The calculated threshold acceleration thus was 6.98 g. In the electrostatic operation test, the response time of the switch was measured to be shorter than 1.2 ms and the minimum contact resistance was 8.5 Ω at the contact force of 284 μN. Life cycle test was carried out to show that the developed switch could operate more than 10,000 cycles without failure. Rotation-table experiment was carried out in sequence to reveal that the switch operates at 6.61 g. The error analysis was carried out in the consideration of the off-axis force generated during the rotation-table experiment. From the experimental values, the off-axis force was

calculated as 2.091 μN and the resulting reduction in the initial switching gap was simulated as 0.236 μm. The reduced threshold acceleration thus was estimated to be 6.512 g, which agrees well with the measured threshold acceleration value of 6.61 g. Rotation-table test using another switch was conducted to model the relation between the off-axis force and the operating acceleration of the developed switch. Least squares method was used in the analysis and the original threshold acceleration (a_{th}) of the switch was calculated as 6.16325 g. The error rate (ε) due to the off-axis force was calculated as -0.22693 g/μN. The modeled operating acceleration of the switch in terms of the off-axis force matched well with the measurements, showing the maximum error less than 1.6%. Heating, sealing, high-g, and impact tests were conducted in sequence to validate the environmental characteristics of the switch. Test condition of 80 °C for 6 hours were adopted for heating test and the tested switch operated more than 200 cycles normally after the test. For sealing test, gross leak test using penetrant dye (Rhodamine B) and fine leak test using tracer gas (helium) were conducted sequentially. 10 samples were put into both of the tests. In the gross leak test, no signs of dye penetration were observed after pressurizing the samples in the dye solution. The tested switches were then put into the fine leak test. In the fine leak test, helium leak rates were measured and all of the tested samples showed leak rate lower than 5.8×10^{-8} atm cc/s He, which is the reject limit provided by MIL-STD-883E. High-g test and drop impact test were also performed to validate the

effectiveness of the displacement-restricting structure. As a result of the high-g test, the developed switch was able to operate without breaking after experiencing the acceleration of 300 g in the $\pm\hat{x}$, $\pm\hat{y}$, and $\pm\hat{z}$ axes. In addition, the drop impact test has proved that the developed switch can withstand an impact as high as 1000 g. The MEMS acceleration switch developed throughout this study is the first to attain low threshold and good environmental characteristics at the same time. Therefore, the author believes that the switch developed in this study is the most suitable one for safety arm unit application among the low-g switches developed so far.

Keywords: MEMS (Microelectromechanical Systems), Acceleration Switch, Inertial Switch, Low-g, Low Threshold Acceleration, Safety Arm Unit.
Student Number: 2013-30974

Table of contents

List of tables

List of figures

1. Introduction

1.1. Sensing of acceleration

In the fast-moving applications such as automobiles, airplanes, spacecraft, and missiles, the acceleration of the system is an important information for the following tasks: airbag / anti-lock braking operation for automobiles [1-3] or ignition, control, drive, disconnect of mechanical parts of the projectiles [4, 5]. This is because the acceleration level the system is undergoing implies that the system is under a certain situation. For example, acceleration of 30 g or above applied to a car may mean that the vehicle has collided with something and the airbag has to operate to protect the driver. According to this sense, the airbag deployment system has acceleration sensors inside it (Figure 1.1 (a)). Also, information on acceleration is actively used in the missile applications for their operation [5]. Most of the missiles and projectiles have safety arming device and INS (inertial navigation system) for safety issue and flight guidance, respectively (Figure 1.1 (b)). The use of acceleration is not limited to those applications above but is inclusive to fighter jet, parachute, and shock or drop monitoring of consumer electronics [6, 7]. Some of the applications that experiences acceleration between 0.1 g to 1000 g are shown in Figure 1.2.

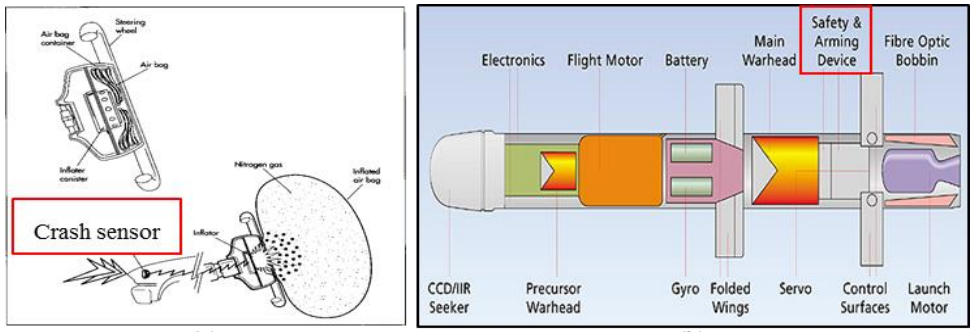

(a) (b)

Figure 1.1. (a) Airbag system with crash sensor and (b) missile with safety arming device.

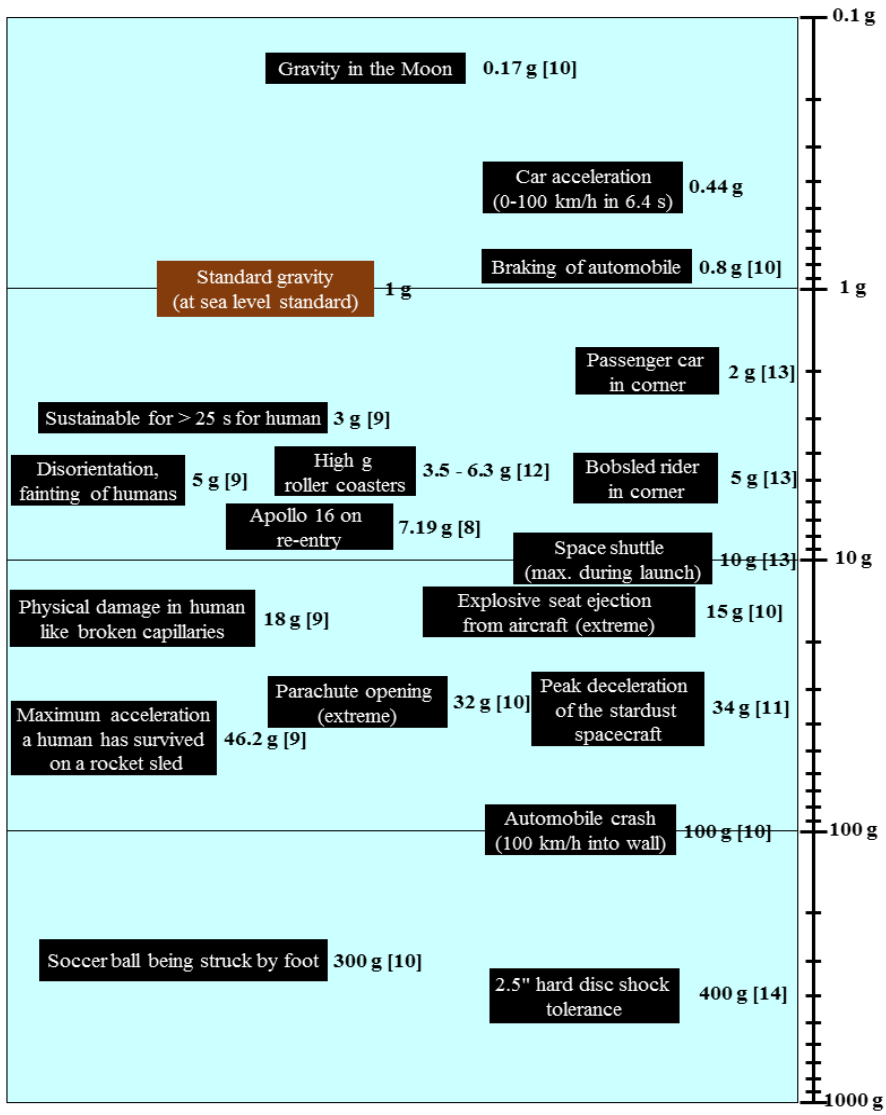

Figure 1.2. Ranges of acceleration for various applications [8-14].

The acceleration level can be detected with accelerometers or acceleration switches. Accelerometers are type of electromechanical devices that measure the proper acceleration, which is the acceleration relative to freefall and is the acceleration felt by objects and human [15].

Accelerometers are often used for navigation and transportation applications because accelerometers can read real-time acceleration continuously. The accelerometers consist of spring, damper, and the proof mass (or the seismic mass). When external acceleration is applied, the proof mass is displaced from its neutral position under the influence of the damper and spring. The displacement of proof mass is then read to the device by transduction, which is from mechanical input (deflection or displacement) to electrical signal. According to the transducing mechanism, accelerometers are classified and the majorities are piezo-electric, piezo-resistive, and capacitive types [13, 16]. Piezo-types (piezo-electric and piezo-resistive types) use the stress created in the piezo-film deposited on the flexural structure. These types have advantages of high impact resistance, wide bandwidth, and wide dynamic range because electrical readout is possible with a small deflection of piezo-materials and one can make the flexural structure mechanically rigid enough. However, piezo-types are rather costly to fabricate and suffer problems such as low resolution, poor long-term stability and low temperature stability. For this reason, the piezo-material MEMS technology is still in developing phase and the application of the piezo-type accelerometers is yet limited [13]. Capacitive type accelerometers read the capacitance change made between the movable and fixed electrodes. Unlike the piezo-electric type devices, capacitive type can provide true DC response, high resolution, high thermal stability, and is cheap. The limits of capacitive accelerometers include small sensing signal, low bandwidth, electromagnetic wave

sensitivity, and limited dynamic range. In addition, capacitive type need rather complex readout circuitry, which increases the cost and size in the practical use.

Acceleration switches, also known as inertial switches or g-switches, are kind of switches that turn on and off by external acceleration. The basic configuration of acceleration switches is the same as that of accelerometers: a mass-damper-spring system. The operation principle of acceleration switches is as shown in Figure 1.3. When the external acceleration is applied, the proof mass, which is suspended in the frame, moves in the opposite direction to the applied acceleration. An electrical connection is then made when the proof mass moves the pre-defined distance, which is the initial gap.

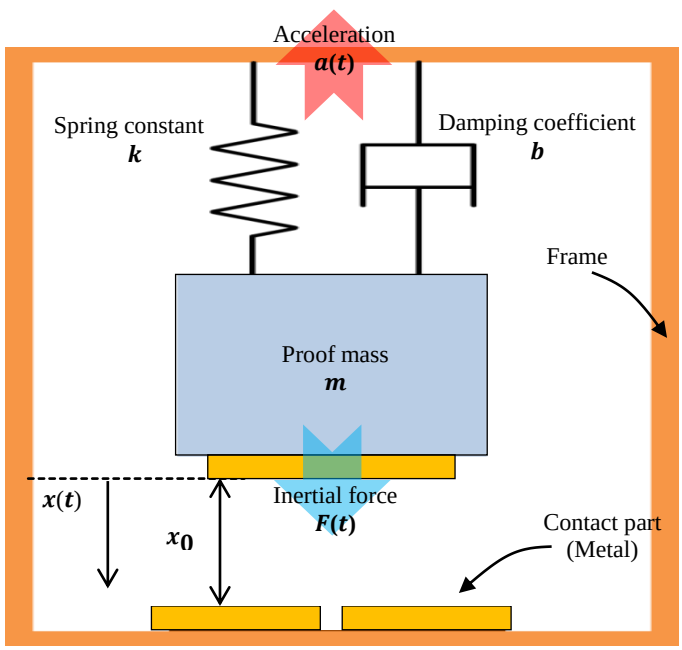

Figure 1.3. Schematic view of acceleration switch.

The minimum input acceleration that makes the proof mass to move the distance of initial gap is called as the threshold acceleration of the switch. The switch

is on/off device and one can only confirm that whether the acceleration above the threshold value is at presence or not by checking whether the electrical path is constructed or not. Therefore, acceleration switches can be adopted to shock-detecting applications where continuous or real-time measurement of acceleration is not necessary. In the performance view, being incapable of real-time measurement, acceleration switches have advantages like long-term stability, high temperature stability, compact readout circuitry, and resistance to electromagnetic wave since acceleration switches do not need piezo-materials or capacitive readout.

In simple shock-detecting applications, such as drop detection of small-size or low-power electronics, using accelerometers would not be a proper choice because of superfluous power consumption and data generation. Furthermore, need for complex and expensive readout circuitry would be a bottleneck in size and cost reduction. In those applications, one can expect order-or-magnitude reduction in power consumption and data generation with the use of acceleration switches [7, 17, 18]. Figure 1.4 shows the comparison of battery lifetime in the cases of using analogue, digital accelerometers and acceleration switch [7]. It can be shown that the acceleration switch has lifetime more than 100 times longer despite the comparison were carried out with commercially available low-power accelerometers. This is because acceleration switches are generally designed to be normally-off and are activated only when the shock event occurs.

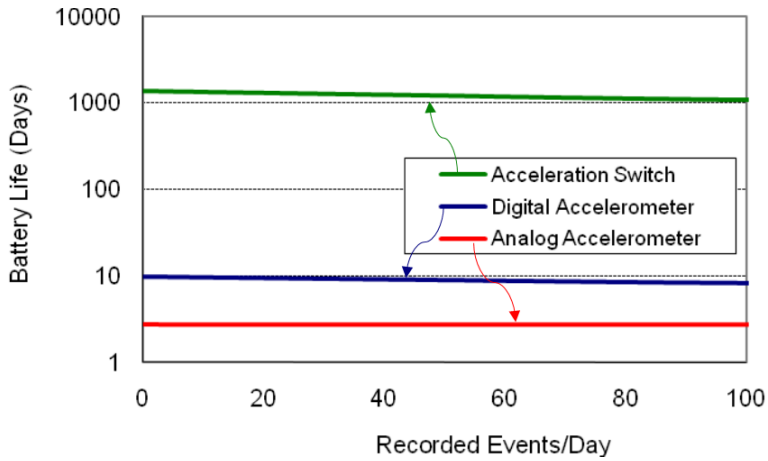

Figure 1.4. Estimated battery lifetime comparison for acceleration recording systems using analog accelerometer (freescale MMA7331LC), digital accelerometer (ADISI6204), and acceleration switch array. Accelerometers were chosen as representative of low-power commercially-available sensors [7].

In large and sophisticated applications, however, the size and power issues of accelerometer barely concern. In those systems, it would be a clever choice to employ acceleration switch and accelerometer together. This is because the accelerometer could produce erroneous output due to electromagnetic noise. In the sense that the invalid output of accelerometer would fail the overall operation process of airbag or missile launching, the genuineness of the accelerometer output must be guaranteed. This can be done with acceleration switch. By checking the state of the acceleration switch when the accelerometer produces output signal, it is possible to confirm whether the signal of the accelerometer is caused by real acceleration or the electromagnetic noise [3]. Figure 1.5 shows the example flow chart of missile launching system using the concept described above. This kind of concept does not only apply to missile but also the airbag deployment system.

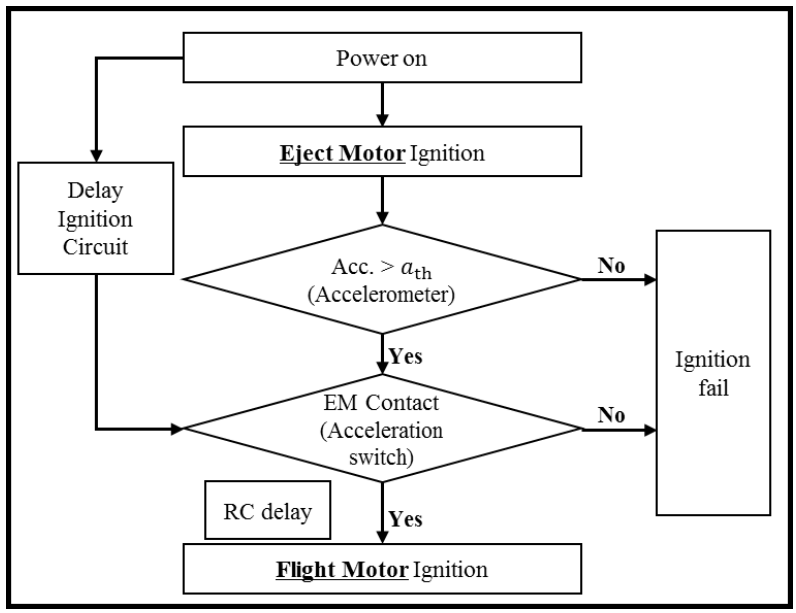

Figure 1.5. Operation flow chart of missile launching system using accelerometer and acceleration together.

1.2. Safety arm unit and MEMS acceleration switches

SAU (safety arm unit), also known as ISD (ignition safety device), is an electromechanical device equipped to missile and the research for safety arm unit is firstly started in 1960 [19]. The role of safety arm unit is to guarantee that the launched missile is under proper situation (altitude, mostly) for the next operation of missile (posture control and flight motor ignition, mostly). Therefore, the failure of safety arm unit is directly related to the failure of missile launch system. In this sense, safety arm device is one of the core parts in missile system and the related technologies are classified as export-restricted technologies in many countries.

In the past, hot-launching technic was mainly used for missile launching. In this launching technique, the flight motor ignites in the launch cell, which damages the launcher and leaves safety issues to the people behind. As the launch technology evolves, however, the use of cold-launching has been expanding worldwide. In the cold-launching technic, the missile is expelled by gas ejection system and the flight motor of missile does not ignites before the missile is far distant from its launcher. This technic is practically used in submarine-launched ballistic missiles since the hot exhaust of flight motor in submarine could lead to a catastrophic result. In the cold-launching process, the point of time (or the distance of the missile from the launcher) to activate the main explosives for flight motor is confirmed with the acceleration applied to the missile. This is possible because the flight distance (or the altitude) of the missile can be inferred by the magnitude and duration of applied acceleration. The measurement of acceleration and the generation of the activation signal are carried out by safety arm unit with acceleration sensors inside.

For safe and successful launching of missile, value and genuineness of the acceleration must be reliably identified. Accelerometers can be used in safety arm

unit to measure the magnitude and duration of acceleration. However, since accelerometers can generate false output signal by electromagnetic noise, additional device is needed to determine whether the acceleration input is genuine or not. To do so, acceleration switches can be used along with accelerometers. This is because acceleration switches do not operate by the electromagnetic noise. Therefore, a more reliable safety arm unit can be realized when acceleration switch is applied.

The example of readout circuitry for acceleration switch is shown in Figure 1.6. When external acceleration above threshold is applied, the acceleration switch turns on to close the electrical circuit. The sensing voltage ($V_{sensing}$) is then applied to the circuit and divided to switch resistance (R_{switch}) and load resistance (R_1). It is preferred to set the value of the load resistance sufficiently large in order to obtain a constant output voltage regardless of the switch resistance value. The output voltage (V_{out}) is then applied to the capacitor through the voltage follower. Then the capacitor starts charging and when the voltage level reaches the pre-defined value, the activation signal is generated and delivered to the missile. Figure 1.7 shows the changes in the applied acceleration, output voltage, and capacitor voltage over time with the illustration of cold-launching process. After the missile is ejected at t_0, it experiences the eject acceleration and the switch is turned on after the response time of the switch, which is at t_1. Between the time period of t_1 and t_2, the capacitor is charged to reach the pre-defined voltage level and this charging time can be engineered with RC (resistive-capacitive) delay. This voltage is then read by the safety arm unit to generate the activation signal for the next operation. With the proper design of acceleration switch and the readout circuit, it is possible to determine not only the genuineness of the acceleration but also the flight distance (or altitude) of the missile.

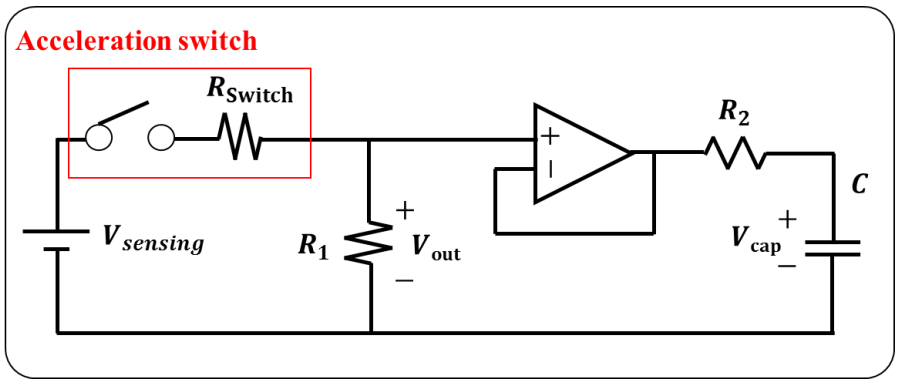

(a)

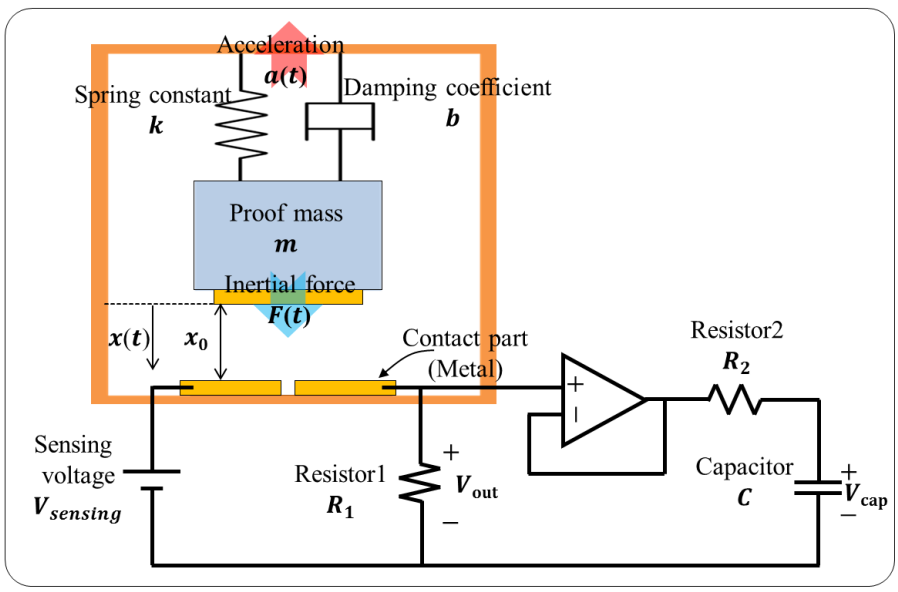

(b)

Figure 1.6. Example of readout circuitry for acceleration switch: (a) equivalent circuit and (b) circuit with acceleration switch shown.

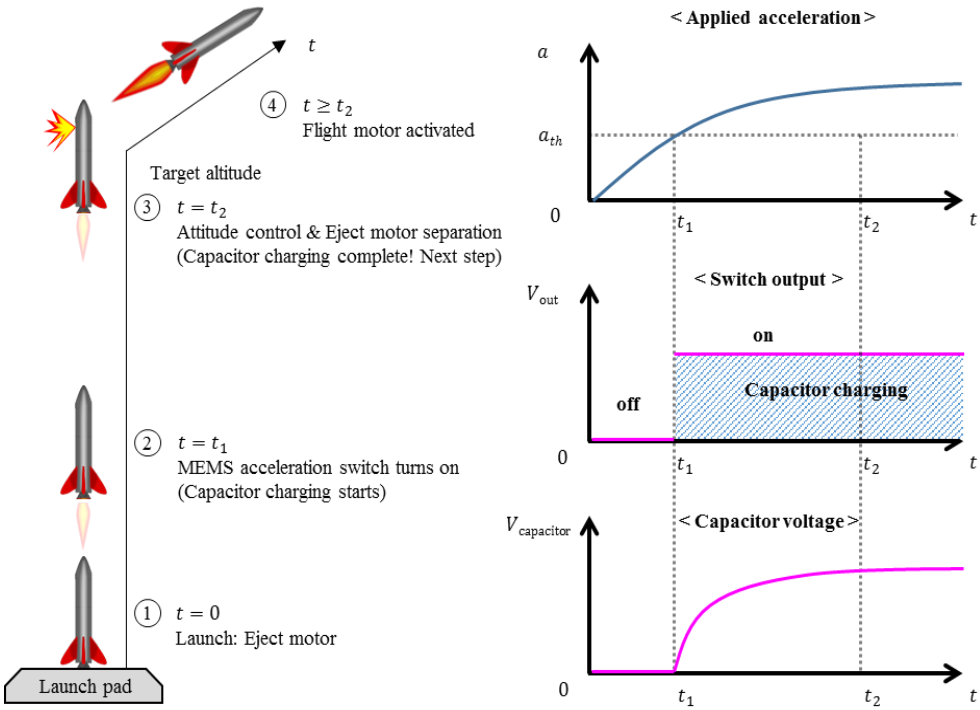

Figure 1.7. (a) Illustration of cold-launching process and (b) acceleration, output voltage, and capacitor voltage versus time.

Most of the modern ICBMs (intercontinental ballistic missiles) and SLBMs (submarine-launched ballistic missiles) are known to use cold-launching. In cold-launching, minimizing the ejection acceleration is important to prevent abnormal operation and breakage of various components (mechanical, chemical, and electrical) inside the missile [20]. In this sense, the maximum ejection acceleration applied to the missile at the initial launch time (~ 0.1 second after launch) is allowed to be less than 15 g [21]. Therefore, the safety arm unit to be equipped in such missiles are required to have an acceleration switch with threshold acceleration below 15 g or less.

The acceleration of missile is determined by its mass and thrust force as shown

in Equation 1.1. In general, acceleration level of long-range missile is low due to the large amount of propellant fuel while the acceleration level is high for short- and medium-range missiles. Figure 1.8 shows orders of threshold acceleration for some of flight and missile applications. It should be noted that the listed acceleration value is typical propulsion accelerations, not the ejection accelerations. As shown in the figure, SAMs (surface-to-air missiles) and ICBMs have a propulsion acceleration of less than 10 g.

$$a_{missile} = \frac{F_{thrust} - F_{gravity}}{m_{missile}} = \frac{F_{thrust} - m_{missile} * \mathrm{g}}{m_{missile}} \qquad \text{(Equation 1.1)}$$

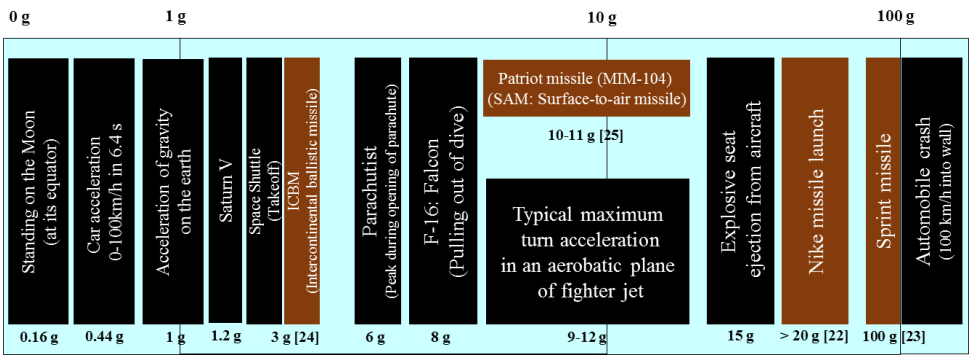

Figure 1.8. Orders of acceleration for flight & missile applications [22-25].

In missile applications, efforts to utilize inertial MEMS (microelectromechanical systems) devices are in active progress due to their extremely small size and low power consumption [26-29]. MEMS acceleration switch is a promising candidate for safety arm unit because one can greatly reduce the size of the module. The miniaturized safety arm unit can be used in small caliber projectile of OICWs (objective individual combat weapons) [30, 31]. Furthermore, unlike the conventional acceleration switches, MEMS switches can provide variety

of functionalities such as self-test capability, latching, set-reset mechanism, damped response, threshold tuning, anti-stiction mechanism [3, 17, 32-34]. With MEMS acceleration switches, therefore, safety arm unit is expected to cope with various requirements of smart weapon systems.

1.3. Literature review

Researches on MEMS acceleration switch can be divided by the structural materials: silicon or metal. After Frobenius et al. firstly reported the all-metal micro-cantilever inertial switch in 1972 [35], there have been many researches on metallic MEMS switches [7, 18, 32, 36-41] and their key strength is the freedom to implement structures by using electroplating process. On the other hand, their primary weakness is the residual stress created during the electroplating process, which deflects the spring structure initially and changes the operation point of the switch. This would reduce the fabrication yield and reliability of the device. Even though there are little residual stresses after fabrication, the stress problem may arise in hot temperature environment. Therefore, stress and temperature control during fabrication and in-use are of necessary requirements for this type of switches. Silicon-based MEMS acceleration switches, however, is relatively free from thermal issues and known to show stress-free structures [3, 17, 33, 34, 42, 43].

Another categorization for MEMS switch is the direction of operation, which can be divided into horizontal (in-plane) and vertical (out-of-plane) direction. The majority of the reported MEMS acceleration switches are horizontally-driven ones because horizontal types provide simple fabrication process and high degree of freedom in design [17, 18, 28, 32-34, 36, 37, 39, 40]. However, fine control of the contact surface is very difficult since the contact surface is constructed on the sidewall of photoresist-mold or the etched sidewall of silicon. Vertically-driven MEMS switches, in contrast, has the opposite pros and cons [3, 38, 41, 42]. They have complex fabrication processes but are capable of adjusting the contact surface.

As mentioned in the previous chapter, MEMS acceleration switches for safety arm unit application should operate under acceleration value below 15 g. In addition

to this, various types of missiles are known to thrust with acceleration values below 10 g [44]. Therefore, MEMS acceleration switch that has low threshold acceleration below 10 g can be used in safety arm unit and various missile applications. However, a few researches were reported for low-g MEMS acceleration switches till now [18, 32, 33, 45]. In 2013, low-g MEMS acceleration switch made of nickel was reported by Wang et al [18]. Multiple electroplating process was used in the fabrication and the switch has threshold acceleration of 38 g. The switch is horizontally-driven type and elastic beam contact was implemented as shown in Figure 1.9. (c). This switch is not considered suitable for missile application since the military standard for missile-equipped device requires maximum temperature range between -51 to 75 °C [46]. This is because the operating point of the switch can be easily changed due to the residual and thermal stresses. In this sense, SCS (single-crystalline silicon) MEMS switch fabricated with bulk micromachining process is advantageous choice since SCS has low CTE (coefficient of thermal expansion) of 2.33 ppm/°C and barely suffers from stress problems [47].

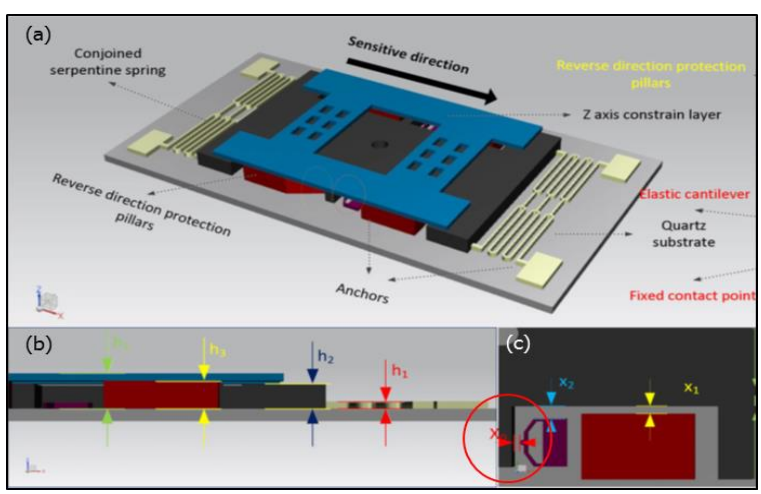

Figure 1.9. Scheme and geometric parameters of the inertia micro-switch device: (a) perspective, (b) side, and (c) top view of contacting structure (red circle) [18].

Kim et al. successfully demonstrated silicon-based lateral MEMS acceleration switch with threshold tuning capability (2 ~ 17.25 g) [33]. The proposed switch is fabricated with conventional SiOG (silicon on glass) process and has normal threshold acceleration of 10.25 g. By installing comb-drive actuators that operates the proof mass in forward and backward of the operating directions, the threshold acceleration can be tuned (Figure 1.10). The weakness of this switch (especially for military use) is that the comb structures are fragile and may break if off-axis impact comes in. In addition, since the sidewall of etched silicon is used as the contact surface, it is difficult to finely control the contact characteristic. Provided that the performance of the MEMS switch strongly depends on the contact surface characteristics [48-50], vertical type is advantageous one because improving the surface characteristic is much easier in the vertical configuration.

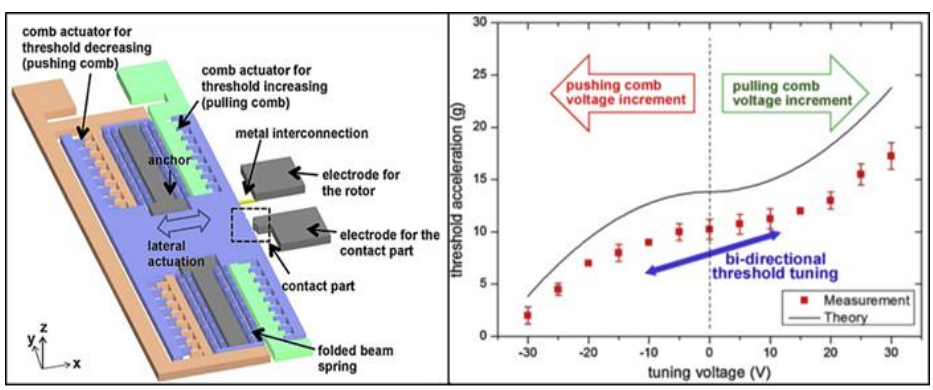

Figure 1.10. (a) Schematic view of threshold-tunable MEMS acceleration switch and (b) measured and theoretical threshold acceleration according to the tuning voltage [33].

The most recent one reported by Xiong et al. is fabricated with double buried-oxide SOI (silicon on insulator) and two glass substrates and its threshold acceleration is 7.42 g [45]. Fabrication schematic and SEM (scanning electron microscope) image are shown in Figure 1.11. This switch is expected to overcome the weaknesses of the two switches introduced before (stress problems, contact surface control) since it is made of silicon and is vertically operating. The main limit of this switch is that the switch does not have proper displacement-restricting structures. In low-g switch, the spring structures are generally very long and thin and they can easily break when acceleration with large magnitude comes in. Overly complicated fabrication process, absence of self-test mechanism, and need for special substrate are also the limitations of this switch. Table 1.1 summarizes the specifications of the low-g MEMS acceleration switches reviewed above.

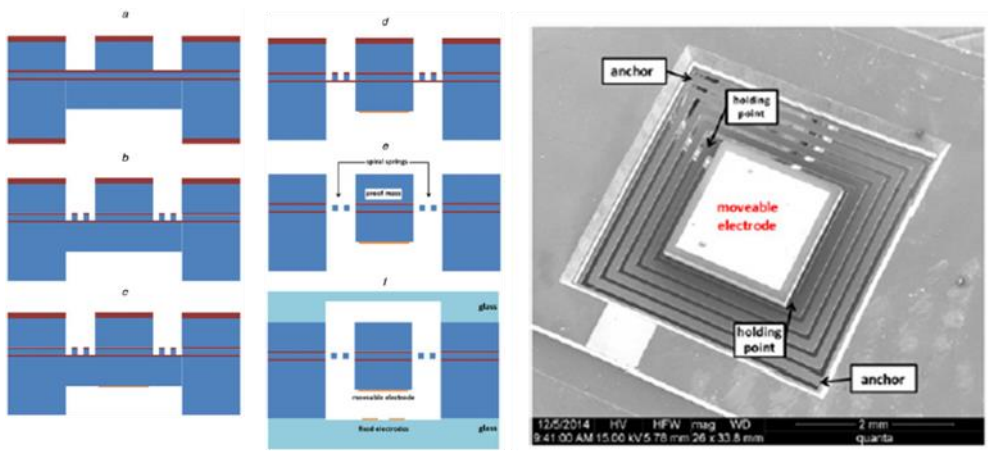

Figure 1.11. (a) Fabrication process of the silicon-based MEMS inertial switch and (b) SEM image of the proposed MEMS switch [45].

Table 1.1. Comparison between the reported low-g MEMS switches.

	[18] Wang et al., 2013	[33] Kim et al., 2014	[45] Xiong et al., 2015
Threshold acceleration	32 g	2.0 ~ 17.25 g	7.42 g
Operating direction	Horizontal	Horizontal	Vertical
Structural material	Ni (electroplated)	Silicon	Silicon
Contact surface	Ni (PR mold)	Silicon (DRIE)	Au
Self-test capability (electrical)	X	O	X
Displacement-restricting structure	O	X	X
Stress-free structure	NA	NA	NA
Lifecycle test	> 1,000 cycles	NA	NA
Thermal stability	NA	NA	NA
Sealing test	NA (not certain on the wafer-level package)	NA (unpackaged)	NA (unpackaged)
High-g test result	X	NA	NA
Impact test	O (up to 800 g)	NA	NA
Notes	- Weak to thermal problems - Stress control issues - Difficult to control contact surface	- Operation voltage needed for threshold tuning - Difficult to control contact surface	- Double-BOX SOI - Complex fabrication - Vulnerable to off-axis impact - No stopper structure

1.4. Motivation and purpose

The purpose of this paper is to develop MEMS acceleration switch that distinct the genuineness of the low acceleration in the safety arm unit. This is necessary because there exists a possibility of accelerometers giving false output due to electromagnetic noise, large off-axis input, etc. In detail, for military use, the developed MEMS acceleration switch should overcome the limitations of previously reported low-g MEMS acceleration switches. The limitations of the MEMS switch reported so far include the risk of stress problems due to the use of metal structure, infeasibility of improving the contact surface, absence of self-test capability, and absence of displacement limiting structures. To overcome the residual and thermal stress problems, we aim to develop MEMS switch that is made with single-crystalline silicon. Also, vertically-driven type is selected to enable fine control of the contact surface. Displacement-restricting structures for $\pm x$, $\pm y$, and $\pm z$ directions are to be included in the switch to prevent breakage of the spring due to excessive travel of the proof mass. Also, the proposed switch has to have self-test capability, which is mandatory to guarantee the reliability before the use of the devices. The fabricated switch is to be packaged hermetically to protect the switch from environmental factors such as dust and moisture. The fabricated switches are to be tested both electrically and mechanically to validate its low threshold acceleration value. Also, environmental tests including thermal, sealing, high-g and drop impact tests are to be performed to validate the switch's environmental stability.

1.5. Contribution

This research focuses on the development of MEMS acceleration switch having low threshold value below 10 g and fine environmental test characteristics at the same time. In the previously reported low-g MEMS switches, multiple electroplating process or comb-drive actuators were introduced to lower the threshold acceleration, which lowers the rigidity of the switch and makes it difficult to obtain fine environmental characteristics for practical use. In the proposed MEMS acceleration switch, each limitation from the reported switches were verified and according solutions were integrated. As a result, low threshold characteristic and good environmental test results including heat, seal, high-g, and impact tests were firstly obtained at the same time. For stress-free structure and consistent operation characteristics in the wide temperature range, silicon-based acceleration switch was designed and fabricated. Design concerns and fabrication issues were addressed in detail. The measured fabrication results verified that the heavy proof mass and flexural spring does not have initial stress problems. Wafer-level packaging were successfully carried out with the through-glass-via electrode made by sandblasting process.

The proposed MEMS acceleration switch demonstrated low threshold characteristic in the rotation-table experiment. With the measurement results, error analysis for the off-axis force was carried out. As far as the author knows, the relation between angular acceleration of the rotation-table and the operating acceleration of MEMS acceleration switch was firstly analyzed in this study. This analysis started from the observation that the center axis of springs and the proof mass's center of mass is not in a line, which makes the proof mass to tilt by the lateral force. Least

squares method was used in the analysis and the error of the operating acceleration due to the tilting of the proof mass was simulated and modeled. For proof-of-concept, rotation-table experiments were conducted using different angular accelerations. The modeled relation between operating acceleration and the off-axis force (thus, the tilting of the proof mass) matched well to show the maximum error less than 1.58 %.

As for environmental tests, heating, sealing, high-g, and impact characteristics were verified to show that the switch could survive and normally operate after all the tests mentioned above. Detailed comparisons were carried out against the previously reported low-g MEMS switches. The comparison result shows that the MEMS acceleration switch developed in this study is the first low-g MEMS acceleration switch that passed heat, sealing, and impact tests altogether and is best suitable for military applications as compared to others.

1.6. Composition of thesis

In Chapter 2 of this thesis, basic theories and design details of the MEMS acceleration switches are described. Theoretical analyses on the serpentine spring and plate damper are also described in this chapter. FEM simulation results, which include force-displacement, displacement-stress characteristic, and the modal analysis are also included in this chapter. Numerical analysis codes for MEMS switches created using MATLAB are also described and provided in this chapter.

Chapter 3 describes the fabrication process of the designed switch and its results. The fabrication process consists of one silicon-on-insulator substrate and two glass substrates. Details on the fabrication process and some of issues to be considered in the process are described. Run sheets are also provided after each of the substrate process. Fabrication results include scanning electron microscope and optical images, fabricated dimensions, and free-hanging posture of the proof mass.

In Chapter 4, the characteristics of the fabricated switches are provided. The results of the electrostatic and acceleration driven experiments are provided. Lifecycle test result and according changes in the contact resistance are provided. The environmental test results of the switch, which include temperature test, sealing test, high-g test, and impact test are described with the detailed test methodologies.

2. Theory and design of low-g MEMS acceleration switch

2.1. Basic theories on acceleration switch

2.1.1. Static threshold acceleration

Figure 2.1 shows the schematic of the acceleration switch. It is basically a mass-damper-spring system in which the proof mass is suspended in the frame by the spring and damper. When the external acceleration is applied, the proof mass moves in the opposite direction to the input acceleration. The displacement of the proof mass $(x(t))$ for the input acceleration $(a(t))$ satisfies the following governing equation [51]:

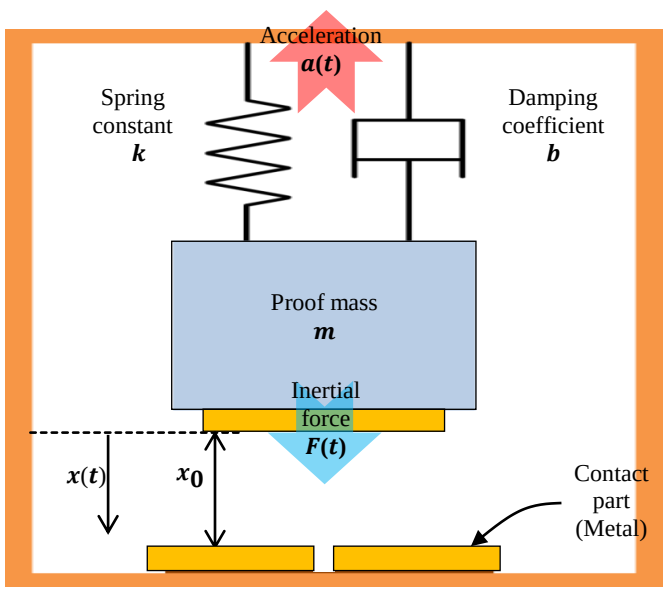

Figure 2.1. Schematic of MEMS acceleration switch.

$$m\frac{d^2x}{dt^2} + c\frac{dx}{dt} + kx(t) = ma(t) \qquad \text{(Equation 2.1)}$$

where m, c, k are the proof mass, damping coefficient, and the spring constant, respectively. The threshold acceleration (a_{th}) means the smallest acceleration input that makes the switch to turn on. However, especially in the transient state, the motion (acceleration, velocity, and displacement) of the proof mass is affected not only by the magnitude but also the waveform and the period of the input acceleration. Therefore, in the transient state, the threshold acceleration cannot be determined as one specific acceleration. Furthermore, the bouncing effect may occur in the transient state, which makes the state of the MEMS switch undistinguishable. Therefore, constant acceleration value that allows the switch to maintain its on-state is used in this study. In the steady-state, the derivative terms in the equation (1) are eliminated to give the threshold acceleration as:

$$a_{th} = \frac{kx_{ini}}{m} \qquad \text{(Equation 2.2)}$$

where x_{ini} is the initial switching gap of the switch.

In order to obtain low threshold acceleration, the spring constant (k) should be lowered, the initial gap (x_{ini}) should be narrowed, and the proof mass (m) should be increased. However, if the spring constant is excessively lowered, the impact resistance of the switch would be decreased and the risk of stiction would be increased. Excessively narrowing down the initial gap also causes issues such as dielectric breakdown during the fabrication process and large variation of the threshold acceleration. This is because the threshold value would change greatly due

to small fabrication error if the initial gap is very small. Raising the mass of the proof mass does not cause a relatively big problem, but it can increase the size of the device or lower the resonance frequency. Therefore, to design low threshold acceleration, it is necessary to design the proper lower limit values of the spring constant and the initial gap first, then determine the value of the proof mass.

2.1.2. Determining the initial gap

As mentioned above, low spring constant, narrow initial switching gap, and heavy proof mass are required at the same time in order to achieve threshold acceleration value as low as 10 g. Among them, it is desirable to determine firstly the initial switching gap in the low-g switch design. This is because the dielectric breakdown may occur during the fabrication process and fail the device if the initial gap is too narrow. When dielectric breakdown occurs, arc current flows, which may cause oxidation, melting and breakage of the metal lines. Figure 2.2 shows the situation in which dielectric breakdown occurs during anodic bonding process. Dielectric breakdown phenomenon in the gap of a few to tens of micrometers follow the modified Paschen's curve [52]. Figure 2.3 shows the modified Paschen's curve reported by Tirumala et al. The minimum fabrication voltage was set to 300 V in the anodic bonding process, and the minimum electrode gap to prevent the dielectric breakdown was confirmed to be greater than 5 μm. Considering the fabrication irregularity, the initial gap was set to 6.5 μm.

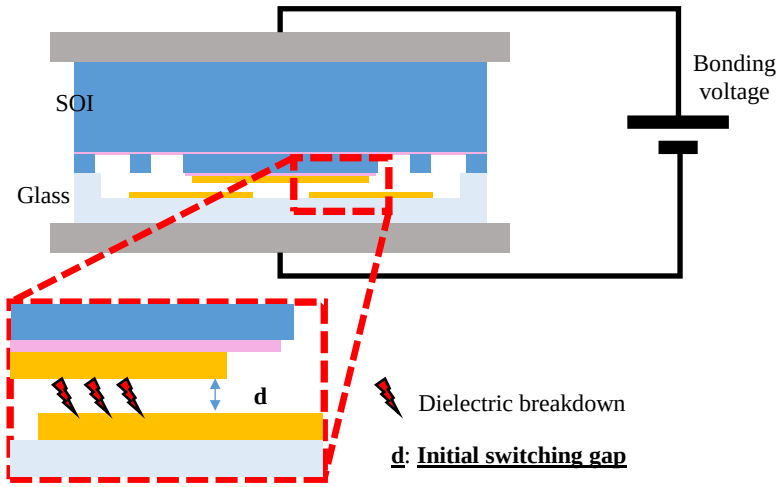

Figure 2.2. Dielectric breakdown during the anodic bonding process.

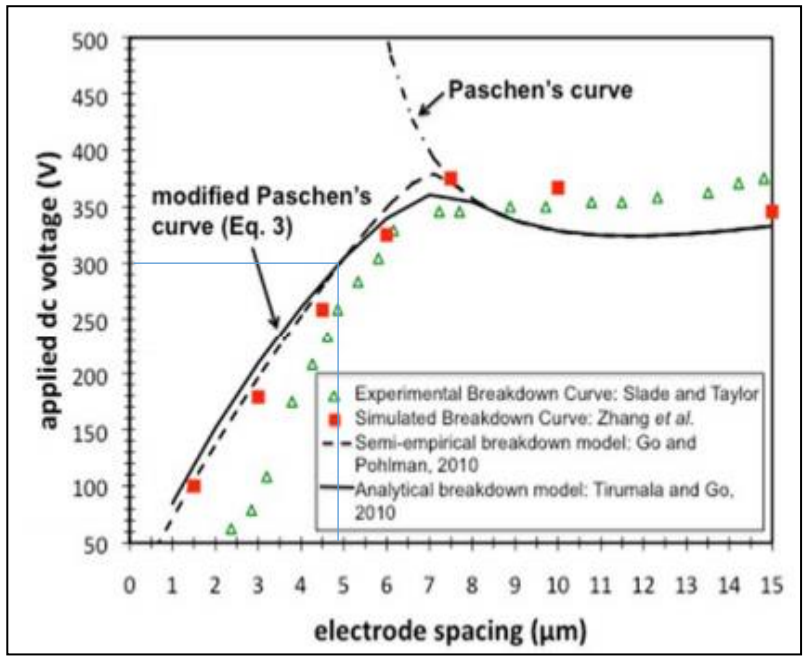

Figure 2.3. Modified Paschen's curve for dielectric breakdown [52].

2.1.3. Serpentine spring

After setting the initial switching gap, the spring constant was designed. To obtain low spring constant with minimum footprint, serpentine spring was adopted in this switch. Figure 2.4 shows the structure of the serpentine spring, and Equation 2.3 is the associated spring constant equation [53].

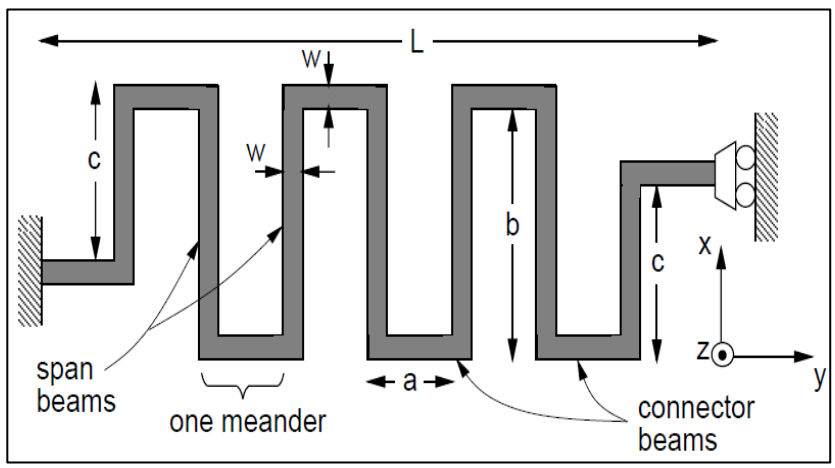

Figure 2.4. Schematic of serpentine spring [53].

The interpretation in Equation 2.3 is based on the assumption that all the lengths of the meander are the same ($b = c$). The elastic stiffness of component a (meander length = shin) and b (meander width = thigh) are represented as S_{ea} and S_{eb} (Equation 2.4 and 2.5). Likewise, S_{ga} and S_{gb} denote the torsional stiffness of a and b (Equation 2.6. and 2.7).

$$k_z = \frac{48\, S_{ea}S_{eb}S_{ga}S_{gb}}{S_{eb}S_{ga}a^2\left(S_{gb}a + S_{ea}b\right)n^3 - 3S_{ea}S_{eb}S_{ga}a^2bn^2 + S_{ea}b\left(2S_{eb}S_{ga}a^2 + 3S_{eb}S_{gb}ab + S_{ga}S_{gb}b^2\right)n - S_{ea}S_{ga}S_{gb}b^3} \quad \text{(Equation 2.3)}$$

$$S_{ea} = E \times I_{x,a} \quad \text{(Equation 2.4)}$$

$$S_{eb} = E \times I_{x,b} \quad \text{(Equation 2.5)}$$

$$S_{ga} = G \times J_a \quad \text{(Equation 2.6)}$$

$$S_{gb} = G \times J_b \quad \text{(Equation 2.7)}$$

The elastic stiffness is the product of Young's modulus and the second moment of inertia. Likewise, the torsional stiffness is the product of shear modulus and the torsion constant. For beam with rectangular cross section, the second moment of inertia and torsion constant is given as:

$$I_{x,a} = I_{x,b} = \frac{wt^3}{12} \quad \text{(Equation 2.8)}$$

$$J_a = J_b = \frac{1}{3}t^3 w\left(1 - \frac{192}{\pi^5}\frac{t}{w}\sum_{i=1,\,odd}^{\infty}\frac{1}{i^5}\tanh\left(\frac{i\pi w}{2t}\right)\right) \quad \text{(Equation 2.9)}$$

where w is the width of the beam and t is the thickness of the beam components.

Detailed design values of the serpentine spring and the calculated spring constant are listed in Table 2.1. The resulting static threshold acceleration (using Equation 2.2) is also listed with the dimensions of the proof mass. From the static design, the threshold acceleration was calculated to be 9.76 g, which is slightly lower than the target value of 10 g. It should be noted that by designing the threshold acceleration slightly lower than the target value, one can obtain additional contact

force and fine contact characteristics.

TABLE 2.1. Detailed design values of the proposed MEMS acceleration switch.

Parts	Symbol	Quantity	Value
Proof mass	l_{pm}	Length of the proof mass	910 μm
	w_{pm}	Width of the proof mass	910 μm
	t_{pm}	Thickness of the proof mass	180 μm
	ρ_{SCS}	Density of SCS	2330 kg/m^3
Serpentine spring	l_{shin}	Length of shin	33 μm
	l_{thigh}	Length of thigh	530 μm
	t_{spr}	Thickness of spring	12.5 μm
	w_{spr}	Width of spring	15 μm
	n	Number of meanders	15
	E_{SCS}	Young's modulus of SCS	179 GPa
	ν_{SCS}	Poisson's ratio of SCS	0.23
MEMS switch	m_{pm}	Mass of the proof mass	307.38 μg
	k_Z	$\hat{z}$-axis spring constant	4.52 N/m
	x_{ini}	Initial switching gap	6.5 μm
	a_{th}	Threshold acceleration	9.76 g
	f_{res}	Resonant frequency	610.31 Hz

The resonant frequency of the designed switch can be obtained using Equation 2.10, and the obtained value was 610.31 Hz. It is preferable to set the resonance frequency of the switch away from the frequency of the input acceleration because resonance phenomenon occurs and the proof mass will move a larger distance when the frequency of the input acceleration is the same with the resonant frequency of

the switch. This should be avoided because the acceleration switch would operate at lower acceleration than threshold when the resonance occur. For use in the safety arm unit in cold-launching process, by referring [21], the time the missile takes to accelerate from zero to the maximum acceleration was found to be 0.05 second (Figure 2.5). The according frequency of the input acceleration was calculated as 5 Hz ($T/4 = 1/(4 * f_{res})$).

$$f_{res} = \frac{1}{2\pi}\sqrt{\frac{k}{m}} \qquad \text{(Equation 2.10)}$$

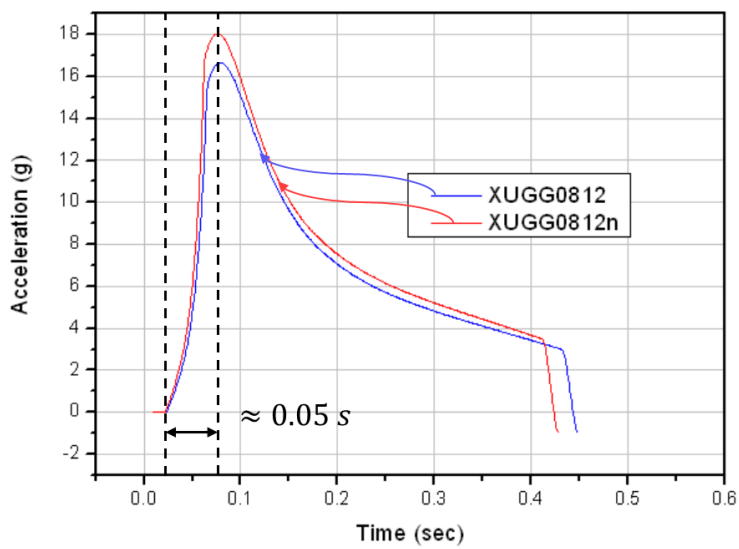

Figure 2.5. Acceleration-time curve of gas-generator-ejected projectiles [21].

2.1.4. Parallel plate damper

The schematic diagram of the plate damper is shown in Figure 2.6. The damping coefficient (c) can be expressed by the following Equations 2.11 - 2.16 according to the analysis reported in [54]. The damping coefficient is dependent of the temporary distance between moving and fixed plates and gets the largest when the distance between the two electrodes is the smallest. In our switch design, moving and fixed plates are the proof mass and bottom metals of glass substrates, respectively. The design parameters are summarized in Table 2.2.

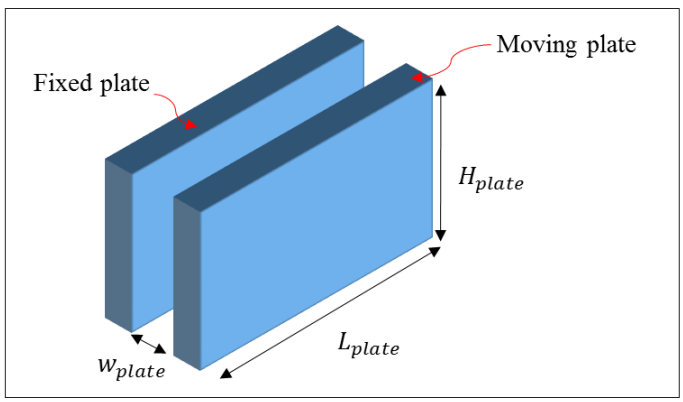

Figure 2.6. Schematic of parallel plate damper [54].

In the calculation of the damping coefficient, nitrogen was selected as an ambient gas and atmospheric pressure is assumed. The mean free path of a gas molecule is then defined as:

$$\lambda = \frac{RT}{\pi\sqrt{2}d^2 N_A P_{Amb}} \qquad \text{(Equation 2.11)}$$

where R, T, d, N_A, P_{Amb} stands for gas constant, ambient temperature, molecular diameter, the Avogadro number, and the ambient pressure, respectively. Then the Knudsen number is defined as:

$$K_n = \frac{\lambda}{w} \qquad \text{(Equation 2.12)}$$

where w is the initial gap between the moving and fixed plates. With the obtained Knudsen number, the relative flow rate coefficient can be calculated as shown in Equation 2.13.

$$Q_{pr} = \frac{1 + 6K_n}{1 + j\omega \frac{\rho h^2 (1 + 10K_n + 30K_n^2)}{10\eta(1 + 6K_n)}} \qquad \text{(Equation 2.13)}$$

The damping coefficients then can be expressed as shown in Equation 2.14 – 2.16, where m and n are odd integers and M and N should be chosen sufficiently large.

$$c = \sum_{m=odd}^{M} \sum_{n=odd}^{N} \frac{1}{Q_{pr} G_{m,n} + j\omega C_{m,n}} \qquad \text{(Equation 2.14)}$$

$$G_{m,n} = \frac{\pi^6 h^3 (mn)^2}{768\eta LH} \left(\frac{m^2}{L^2} + \frac{n^2}{H^2}\right) \qquad \text{(Equation 2.15)}$$

$$C_{m,n} = \frac{\pi^4 h (mn)^2}{64 P_a LH} \qquad \text{(Equation 2.16)}$$

TABLE 2.2. Detailed design values of the parallel plate damper.

Symbol	Quantity	Value
λ	Mean free path length of a gas molecule	65.4 nm
R	Gas constant	8.3144 J/(mol*K)
T	Temperature	300 K
d	Molecule diameter	375 pm
N_A	Avogadro number	6.02E+23 1/mol
P_{Amb}	Ambient pressure	101325 Pa
K_n	Knudsen number	0.0082
Q_{pr}	Relative flow rate coefficient	1.0491
h	Momentary position of the plate	-
ρ	Density of the fluid	1.138 kg/m^3
η	Viscosity of the fluid	17.91E-06 Pa/s
w	Initial distance between plates	6.5 µm
H	Height of the plate	910 µm
L	Length of the plate	910 µm

2.2. Model description

Figure 2.7 and 2.8 show the perspective and cross-sectional schematics of the proposed switch, respectively.

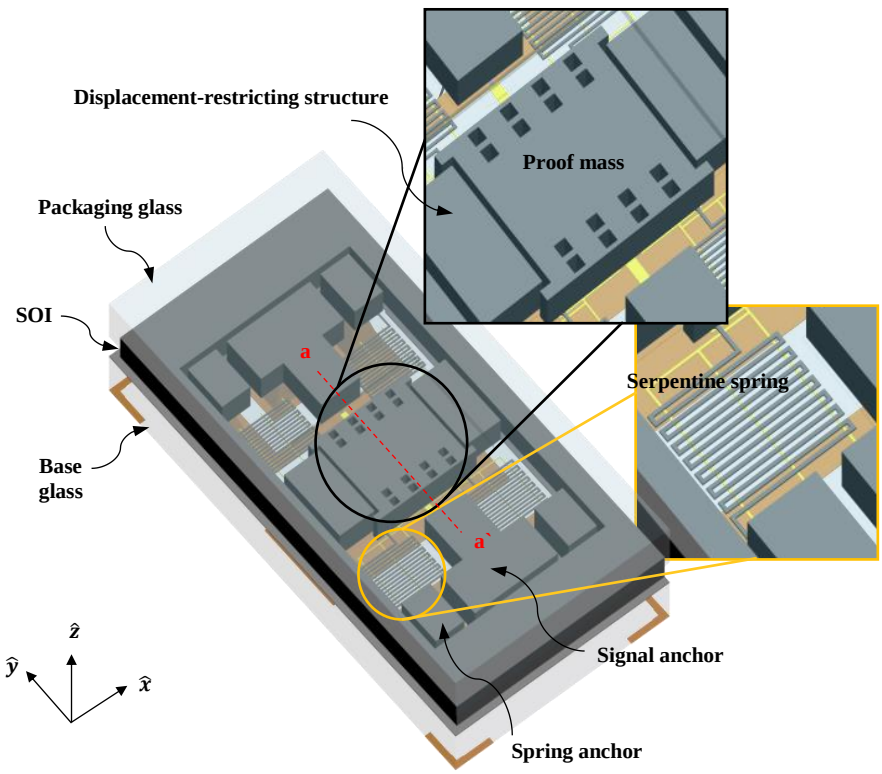

Figure 2.7. Perspective schematic of the proposed MEMS acceleration switch. Insets show the proof mass with displacement-restricting structure and serpentine spring.

The proposed switch can be divided into three layers: base glass, SOI, and packaging glass. The proof mass is in the SOI layer and suspended by four serpentine springs. The contact metal is constructed under the proof mass. Below the contact metal, there are two physically disconnected signal lines on the base glass layer. The gap between the contact metal and the signal lines is the initial switching gap. When the $\hat{z}$-axis acceleration input is greater than the threshold value, the proof mass

comes down to make an electrical connection with the two signal lines (on-state). As soon as the applied acceleration becomes smaller than the threshold value, the proof mass returns to its initial position and the switch goes into the off-state.

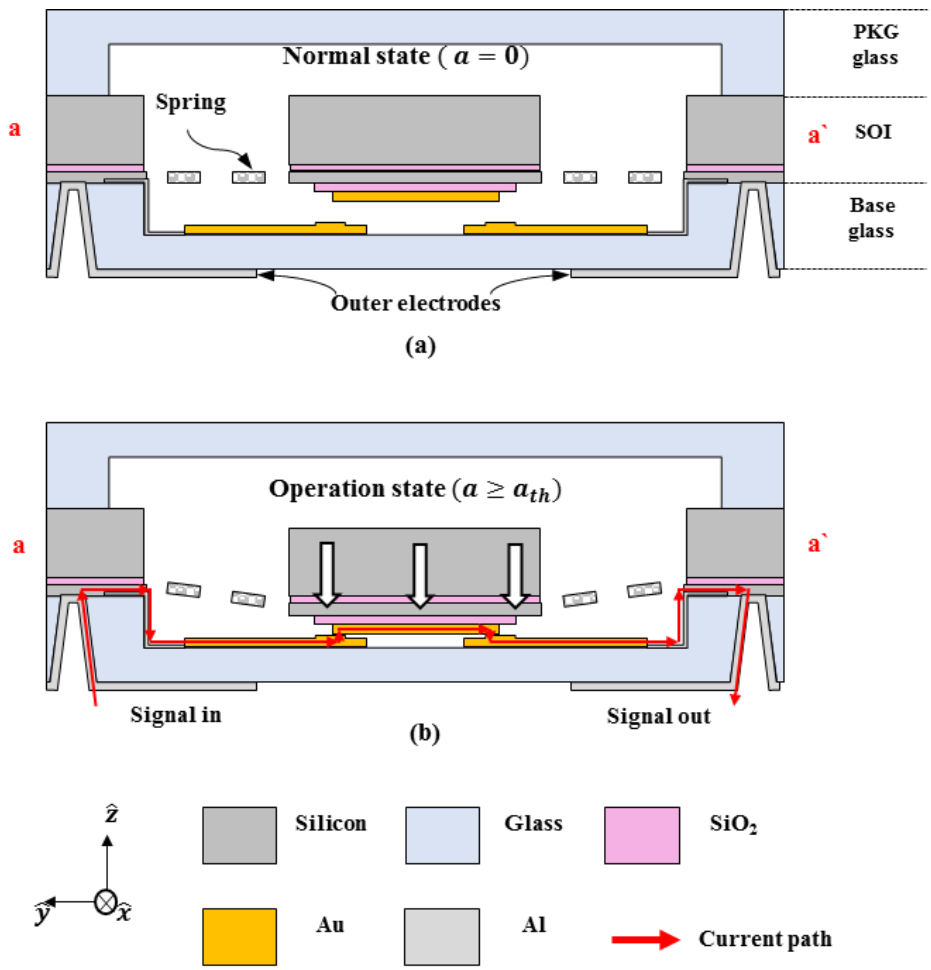

Figure 2.8. Cross-sectional schematic of the proposed MEMS acceleration switch: (a) normal state (switch off) and (b) operation state (switch on). Note that the spring structures are represented by shading.

2.2.1 Base glass substrate

The base glass substrate consists of trench, signal lines, electrostatic pads, and other metal lines for the current path. Two physically disconnected signal lines are formed inside the trench and are electrically connected to the outer electrode through bias line and through-glass via (Figure 2.8). The electrostatic pads are formed around the signal lines and provide electrical self-test capability after fabrication. Since the proposed acceleration switch uses heavy mass and flexural spring, features to prevent stiction phenomenon is adopted. The first one is dimple patterns to reduce the effective contact area between contacting metals (Figure 3.3). The other one is anti-stiction strip, which prevents full collapse of serpentine spring (Figure 3.4). The proposed MEMS switch can be directly soldered to the surface of PCB (printed circuit board) since the electrodes are formed flat on the bottom of the base glass substrate. Furthermore, the switch can be packaged with anodic bonding process since there are no obstructions on the bonding surface.

2.2.2 SOI substrate

The SOI substrate contains anchors, the proof mass, displacement-restricting structures, and four serpentine springs. The proof mass is square-shaped and located at the center. On both sides of the proof mass, displacement-restricting structures are constructed at specific intervals. Four serpentine springs are attached near the four bottom vertices of the proof mass. The contact metal is formed at the bottom of the proof mass. In order to realize high proof mass and low spring constant at the same time, the proof mass uses both the handling and device layer of the SOI substrate,

while the spring uses the device layer only.

2.2.3 Packaging glass substrate

The packaging glass has relatively deep trench. This trench acts as displacement-restricting structure for the proof mass in the $\hat{z}$-axis direction. The depth of this trench should be determined carefully because too deep or too shallow trench would lead to failure of the switch. If the trench is too shallow, the proof mass may be sticked to the packaging substrate due to the electrostatic force generated during the anodic bonding process, which makes the switch inoperable. On the contrary, if the trench is too deep, the proof mass may travel too far and the spring structure would be broken when impact comes in.

2.3. FEM simulation

2.3.1. Force, displacement, stress simulation

Figure 2.9 shows the result of force-displacement simulation under steady-state condition. Total force of 30.14 μN was applied on the topside of the proof mass to simulate 10 g acceleration input. When the force according to 10 g is applied, the proof mass moved 6.76 μm downward and the according spring constant was 4.46 N/m, which agreed well with the analytic value.

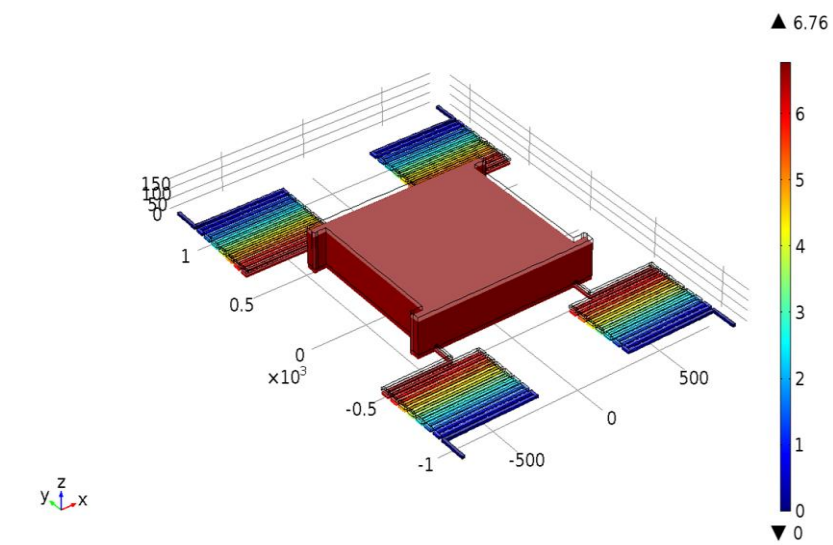

Figure 2.9. Displacement-force simulation result of the proposed MEMS acceleration switch under steady-state condition (10 g acceleration).

Next, simulation on the displacement-principal stress characteristic was carried out. This is necessary because the maximum principal stress theory states that the breakage of brittle material occurs when the magnitude of first or third principal stress exceeds the yield strength of the brittle material [55]. For the $\hat{z}$-axis movement,

the maximum principal stress was observed at the connecting part of the spring and the anchor. The magnitude of the principal stress increased with the displacement of the proof mass (Figure 2.10). Thus the permissible displacement of the proof mass should be limited less than to a certain point which makes the applied principal stress equal to the yield strength of the silicon (7 GPa). Stress concentration factor of 33 was applied since the spring-mass connecting part has sharp-shaped corner [56]. The resulting critical fracture stress was 212 MPa (7 GPa/33). The maximum principal stress acting on the spring structure exceeded 212 MPa when the proof mass traveled more than 150 μm. Based on this result, the depth of trench in the packaging glass was designed to be shallower than 150 μm.

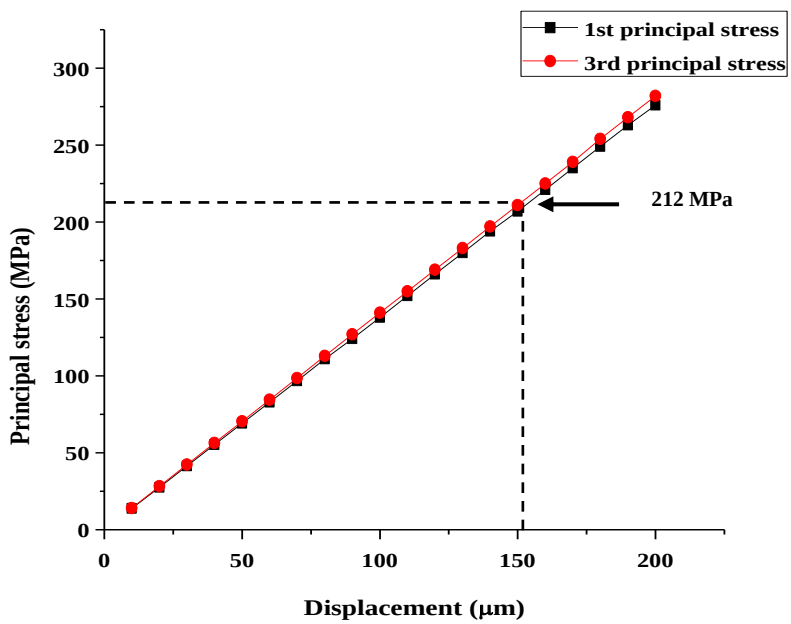

Figure 2.10. Displacement-principal stress simulation result of the proposed MEMS switch under steady-state condition.

‘

2.3.2. Modal analysis – Resonant frequency

Modal analysis was performed to verify the frequency-vibration characteristics of the designed switch. Modal analysis is necessary because it causes the displacement of the proof mass to be amplified by resonance when the frequency of the input acceleration (or noise vibration) has frequency similar to the resonant frequency of the switch. In general, the vibrational system produces an output proportional to the input for an input signal with a frequency lower than the resonant frequency. However, the system would produce a higher output for an input with a frequency similar to the resonant frequency (Figure 2.11). On the other hand, the system would produce a lower output for an input with a frequency higher than the resonant frequency. This is because the Laplace domain transfer function $H(s)$, which relates the displacement and force $X(s) = H(s)F(s)$, is equal to the inverse of the dynamic stiffness as shown in Equation 2.17. The magnitude of displacement is dependent on the frequency of the input force. Note that the roots of the denominator in the transfer function are the poles of the system.

$$H(s) = \frac{1}{ms^2 + cs + k} \qquad \text{(Equation 2.17)}$$

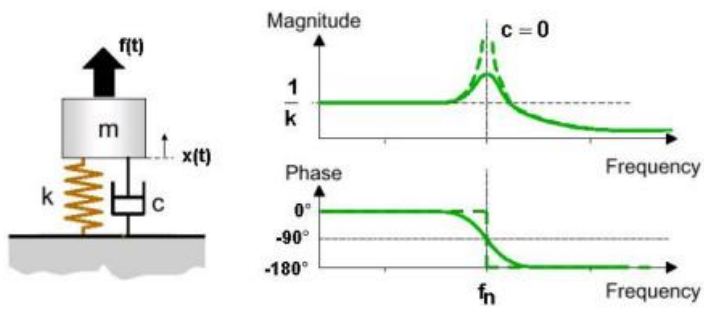

Figure 2.11. Single-degree-of-freedom system.

In actual situations, vibrational noise is the sum of vibrations with various frequencies. To deal with the vibration problem, it is important to know the dominant frequency of the vibration. The dominant frequency of the vibration is the frequency of the vibration that has the greatest amplitude among the whole. As shown in Figure 2.5, the dominant frequency in the missile ejection was revealed to be about 5 Hz. Therefore, the acceleration switch should have a resonant frequency greater than 5 Hz for input-proportional characteristic of the switch. In the design process, the resonant frequency for the operation direction ($\pm\hat{z}-\text{direction}$) of the switch was confirmed to be about 610 Hz. Figure 2.12 shows the first three order modes of the designed switch. The first mode is in the operational direction and its resonant frequency was verified to be 594.25 Hz, which corresponds to 2.70 % error compared with the calculated result. This allows us to verify that the acceleration switch would produce a normal output proportional to the input acceleration. The second and third modes are in $\pm\hat{y}$ and $\pm\hat{x}$ directions and their resonant frequencies are 965.94 and 973.02 Hz, respectively. Figure 2.13 shows the fourth, fifth, and sixth order modes and they are in $\pm\widehat{\Omega_y}$, $\pm\widehat{\Omega_x}$, and $\pm\widehat{\Omega_z}$ directions, respectively.

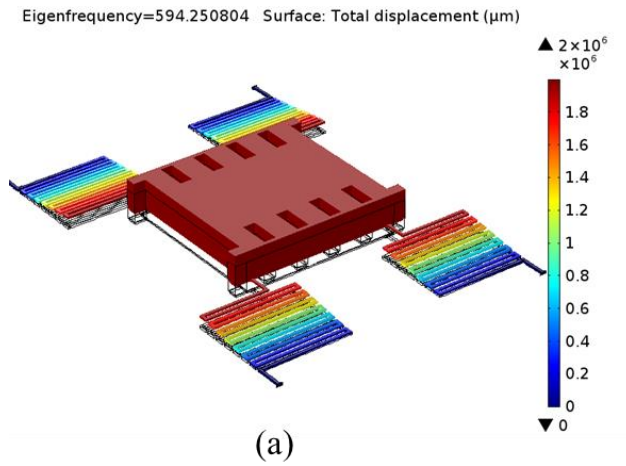

(a)

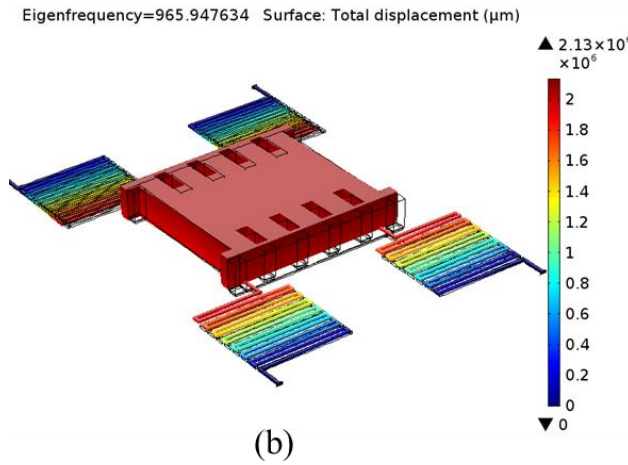

(b)

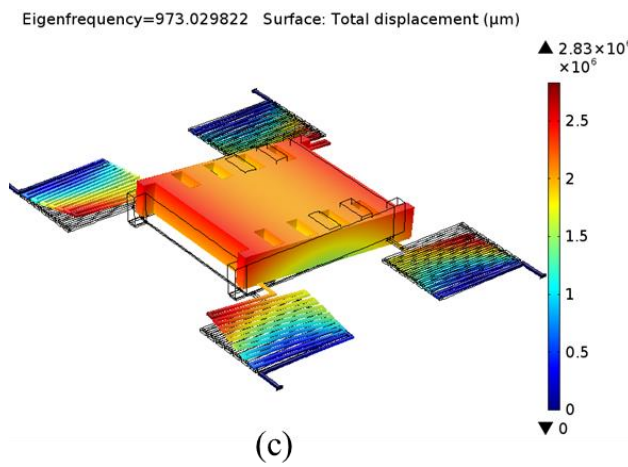

(c)

Figure. 2.12. Results of modal analysis: (a) 1st ($\pm\hat{z}$), (b) 2nd ($\pm\hat{y}$), and (c) 3rd ($\pm\hat{x}$) resonant modes.

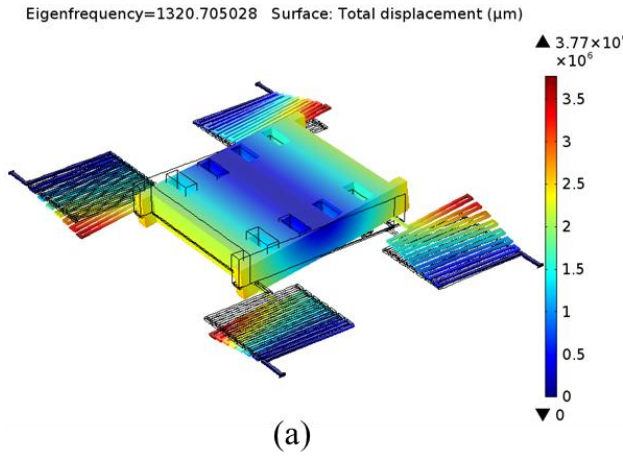

(a)

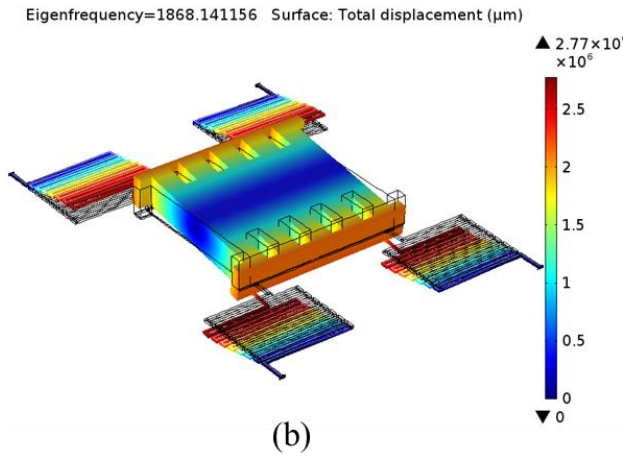

(b)

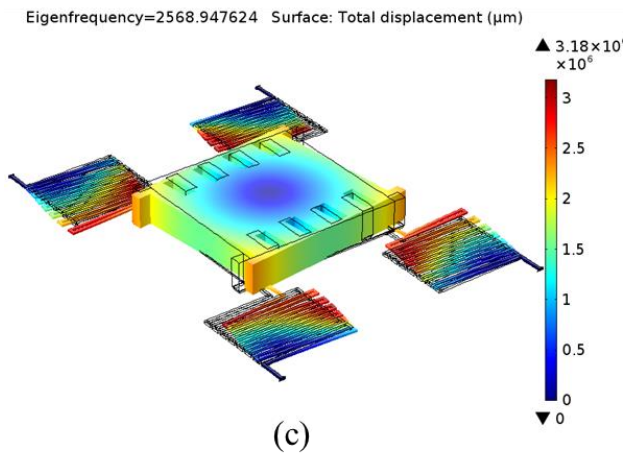

(c)

Figure. 2.13. Results of modal analysis: (a) 4th ($\pm\widehat{\Omega_y}$), (b) 5th ($\pm\widehat{\Omega_x}$), and (c) 6th ($\pm\widehat{\Omega_z}$) resonant modes.

In general submarine environments, the dominant frequency of vibration varies depending on the location (i.e., source) and is known to range from tens to 1.6 kHz. Therefore, the resonant frequency of the acceleration switch should be lower than 1.6 kHz. This gives the permissible range of the resonant frequency for acceleration switch to be greater than 5 and lower than 1.6 kHz. However, it is not easy to set all the resonance frequencies of the higher order modes within 1.6 kHz. Therefore, it is preferable to use a noise absorber, an isolator, or the like in the actual situations [57].

2.4. MATLAB code for MEMS switch

Numerical analysis is practically used to analyze the behavior of proof mass of MEMS acceleration switch. This is because the conditions, such as the damping coefficient, the surface forces, and the collision force, varies with the movement of the proof mass and this situation cannot be expressed simply within a single mathematical expression. Also, considering that the waveform of the input acceleration is actually a combination of half-sine wave (or half-saw tooth) and constant inputs, numerical method has the advantage of being able to apply various type of inputs immediately. Therefore, in this work, we developed MATLAB-based numerical analysis code. The flowchart for the code is shown in Figure 2.14.

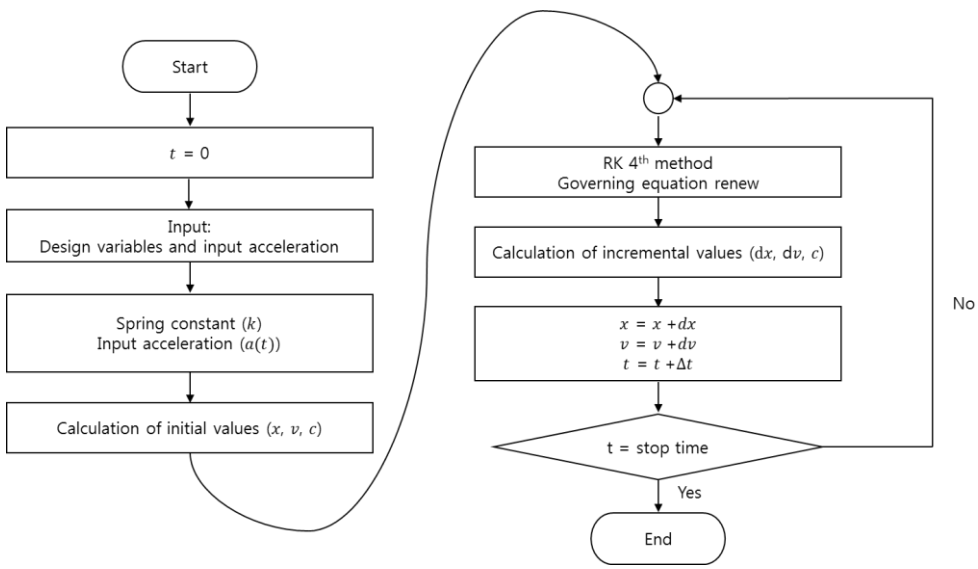

Figure 2.14. The flowchart of the MATLAB code developed in this study.

When the code is started, the user inputs the design variables and information about the input acceleration first. Then, spring constant is calculated and the waveform of input acceleration is generated. Next, initial values are calculated with

the equations given above to complete the governing equation expressed in Equation 2.1. The displacement and velocity of the proof mass after time interval (dt) is numerically calculated using the RK 4th (Runge-Kutta 4th) method. When the incremental values are calculated, the system coefficients (damping coefficient, acceleration, velocity) are replaced with new ones and the governing equation is renewed. The equation sets used for Runge-Kutta 4th method in this study are listed as below.

$$\frac{d^2x}{dt^2} = F(t, x, \dot{x}) = \frac{ma(t) - c\frac{dx}{dt} - kx}{m} = \frac{ma(t) - c\frac{dx}{dt} - kx}{m} \quad \text{(Equation 2.18)}$$

$$k_{\dot{x}1} = F(n) = F\left(t(n),\ x(n), \dot{x}(n)\right), \qquad k_{x1} = \dot{x}(n)$$

$$k_{\dot{x}2} = F\left(t(n) + \frac{h}{2},\ x(n) + \frac{h}{2}k_{x1}, \dot{x}(n) + \frac{h}{2}k_{\dot{x}1}\right),\ k_{x2} = \dot{x}(n) + \frac{h}{2}k_{\dot{x}1}$$

$$k_{\dot{x}3} = F\left(t(n) + \frac{h}{2},\ x(n) + \frac{h}{2}k_{x2}, \dot{x}(n) + \frac{h}{2}k_{\dot{x}2}\right),\ k_{x3} = \dot{x}(n) + \frac{h}{2}k_{\dot{x}2}$$

$$k_{\dot{x}4} = F\left(t(n) + h,\ x(n) + hk_{x3}, \dot{x}(n) + k_{\dot{x}3}\right), \qquad k_{x4} = \dot{x}(n) + hk_{\dot{x}3}$$

$$d\dot{x} = \frac{h}{6}(k_{\dot{x}1} + 2k_{\dot{x}2} + 2k_{\dot{x}3} + k_{\dot{x}4}), \qquad dx = \frac{h}{6}(k_{x1} + 2k_{x2} + 2k_{x3} + k_{x4})$$

$$\dot{x}(n+1) = \dot{x}(n) + d\dot{x}, \qquad x(n+1) = x(n) + dx$$

Figure 2.15 shows the results of the MATLAB code developed in this study. The proof mass, initial gap, and the spring constant of the switch was 3.0738 E-07 kg (or 307.38 μg), 6.5 μm, and 4.54 N/m, respectively. The input acceleration has a sine wave shape in the rising period ($0 < t < 25$ ms) and is maintained constant thereafter (Figure 2.15. top). The magnitude and period of the input acceleration were 12 g and 10 Hz, respectively. The results of the code show the generated acceleration, displacement and velocity of the proof mass, and varying damping coefficient, ordering from the top of Figure 2.15. As predicted in the modal analysis, the displacement of the proof mass well followed the waveform of the input acceleration. The MATLAB source code is provided in the end of this chapter.

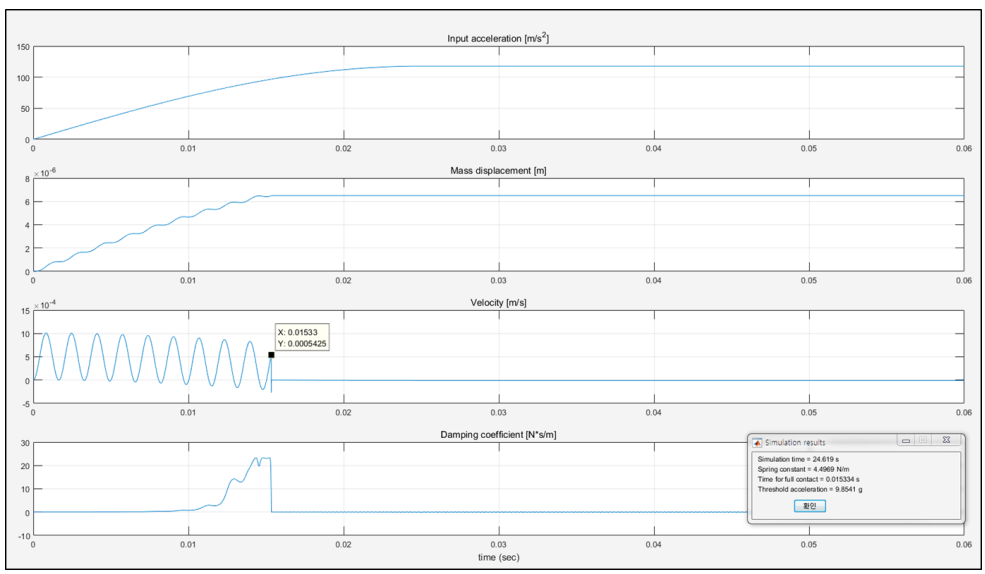

Figure 2.15. The results of the MATLAB analysis code (input acceleration is the combination of (1/4)*T sine wave and constant input: peak magnitude / frequency = 12 g / 10 Hz).

```
function MEMS_ACC_SW_V1

clc


%% Material properties of single - crystalline silicon

PoissonRatio = 0.23;

YoungsModulus = 179e9;

TorsionModulus = YoungsModulus / (2 * (1 + PoissonRatio));


%% Current design values of serpentine spring

ShinLeng = 33e-6;              % Length of shin (m)

ThighLeng = 530e-6;            % Length of thigh (m)

SprWid = 15e-6;                % Width of spring (shin and thigh) (m)

SprThi = 12.5e-6;              % Thickness of spring (shin and thigh) (m)

NumofShin = 15;                % Number of shin

NumofThigh = 15;               % Number of thigh

ProofMass = 3.0738e-7;         % Mass of the proof mass (kg)

IniGap = 6.5e-6;               % Initial gap (m)

COR = 0.5;                     % Coefficient of restitution 0< = COR = <1

StopTime = 0.06;               % Analysis time


%% Current design values of plate damper

GC = 8.314472;                 % Gas constant (J / (mol * K))

Temp = 300;                    % Temperature (K)

MD = 375e-12;                  % Molecule diameter of nitrogen (m)

NAvo = 6.02214086e23;          % Avogadro number (1 / mol)
```

```
PAmb = 101325;                  % Ambient pressure (N / m^2)
GapDist = 6.5e-6;               % Damper gap distance (m)
Den = 1.1384671105;             % Density of fluid (kg / m^3)
Visco = 17.913785625e-6;        % Viscosity of fluid (Pa / s)
ProofMassLeng = 910e-6;         % Damper (proof mass) length (m)
ProofMassWid = 910e-6;          % Damper (proof mass) width (m)

%% Current setting of the input acceleration
AccMag = 12;                    % Magnitude of input acceleration (g)
AccFreq = 10;                   % Frequency of acceleration (Hz)
TypeofInputAcc = 's';           % Waveform of input acceleration

%% Input dialogs for spring dimension, proof mass, initial gap, CoR, and stop time
Title1 = 'Silicon - based vertical MEMS switch model (V1)';

prompt1 = {'Shin length (in micron): ', 'Thigh length (in micron): ', 'Spring width (in micron): ', 'Spring thickness (in micron): ', 'Number of Shin: ', 'Number of Thigh: ', 'Proofmass (in kilogram): ', 'Initial gap (in micron): ', 'Coefficient of restitution: ', 'Observe time (in second): '};

size_wind1 = [1 90; 1 90; 1 90; 1 90; 1 90; 1 90; 1 90; 1 90; 1 90; 1 90];

defaultans1 = {num2str(ShinLeng * 1e6, 5), num2str(ThighLeng * 1e6, 5), num2str(SprWid * 1e6, 5), num2str(SprThi * 1e6, 5), num2str(NumofShin, 5), num2str(NumofThigh, 5), num2str(ProofMass, 5), num2str(IniGap * 1e6, 5),
```

```
num2str(COR, 5), num2str(StopTime, 5)};

Answer1 = inputdlg (prompt1, Title1, size_wind1, defaultans1, 'on');

ShinLeng = str2double (Answer1{1}) * 1e-6;
ThighLeng = str2double (Answer1{2}) * 1e-6;
SprWid = str2double (Answer1{3}) * 1e-6;
SprThi = str2double (Answer1{4}) * 1e-6;
NumofShin = str2double (Answer1{5});
NumofThigh = str2double (Answer1{6});
ProofMass = str2double (Answer1{7});
IniGap = str2double (Answer1{8}) * 1e-6;
COR = str2double (Answer1{9});
StopTime = str2double (Answer1{10});

%% Input dialogs for the input acceleration
Title2 = 'Generation of acceleration';

prompt2 = {'Magnitude of Acceleration (in g): ', 'Frequency of Acceleration (in Hz):
', 'Type of Acceleration (s - > sine, t - > saw tooth, u - > unit step)'};

size_wind2 = [1 90; 1 90; 1 90;];

defaultans2 = {num2str(AccMag, 5), num2str(AccFreq, 5), TypeofInputAcc};
```

```
Answer2 = inputdlg (prompt2, Title2, size_wind2, defaultans2);

AccMag = str2double (Answer2{1}) * 9.81; % Magnitude of input acceleration
AccFreq = str2double (Answer2{2});          % Frequency of input acceleration
TypeofInputAcc = Answer2{3};                % Waveform of input acceleration

%% Input dialogs for plate damper
Title3 = 'Parallel plate damping';

prompt3 = {'Gas constant (in J / (mol * K)): ', 'Temperature (in K): ', 'Molecule
diameter of Nitrogen (in m): ', 'Avogadro number (in 1 / mol): ', 'Ambient pressure
(in N / m^2): ', 'Damper gap distance (in micron): ', 'Density of the fluid (in kg / m^3):
', 'Viscousity of the fluid (in Pa / s): ', 'Proofmass length (in micron): ', 'Proofmass
width (in micron): '};

size_wind3 = [1 90; 1 90; 1 90; 1 90; 1 90; 1 90; 1 90; 1 90; 1 90;];

defaultans3 = {num2str(GC, 5), num2str(Temp, 5), num2str(MD, 5), num2str(NAvo,
5), num2str(PAmb, 5), num2str(GapDist * 1e6, 5), num2str(Den, 5), num2str(Visco,
5), num2str(ProofMassLeng * 1e6, 5), num2str(ProofMassWid * 1e6, 5)};

Answer3 = inputdlg (prompt3, Title3, size_wind3, defaultans3);

GC = str2double (Answer3{1});
Temp = str2double (Answer3{2});
```

```
MD = str2double (Answer3{3});

NAvo = str2double (Answer3{4});

PAmb = str2double (Answer3{5});

MFP = (GC * Temp) / (pi () * sqrt (2) * MD^2 * NAvo * PAmb);

% Mean free path (m)

GapDist = str2double (Answer3{6}) * 1e-6;

NKnudsen = MFP / GapDist;                    % Knudsen number

Den = str2double (Answer3{7});

Visco = str2double (Answer3{8});

ProofMassLeng = str2double (Answer3{9}) * 1e-6;

ProofMassWid = str2double (Answer3{10}) * 1e-6;


tic                                % Simulation time measurement start


%% Calculation of spring constant

Ixa = SprWid * SprThi^3/12; % Bending momentum of inertia of shin about x-axis

Ixb = SprWid * SprThi^3/12; % Bending momentum of inertia of thigh about x-axis

Sea = YoungsModulus * Ixa; % Elastic stiffness of shin

Seb = YoungsModulus * Ixb; % Elastic stiffness of thigh


if SprWid > SprThi

   syms n;

   SigFunc1 = double (symsum (1 / (2 * n + 1)^5 * tanh ( (2 * n + 1) * pi * SprWid

   / (2 * SprThi)), n, 0, 999));

   Ja = (1 / 3) * SprThi^3 * SprWid * (1 - (192 / (pi)^5) * SprThi / SprWid *
```

```
    SigFunc1);                          % Torsion constant of shin
    Jb = (1 / 3) * SprThi^3 * SprWid * (1 - (192 / (pi)^5) * SprThi / SprWid *
    SigFunc1);                          % Torsion constant of thigh
    Sga = Ja * TorsionModulus;          % Torsional stiffness of shin
    Sgb = Jb * TorsionModulus;          % Torsional stiffness of thigh
else
    syms n;
    SigFunc2 = double (symsum (1 / (2 * n + 1)^5 * tanh ( (2 * n + 1) * pi * SprThi /
    (2 * SprWid)), n, 0, 999));
    Ja = (1 / 3) * SprWid^3 * SprThi * (1 - (192 / (pi)^5) * SprWid / SprThi *
    SigFunc2);                          % Torsion constant of shin
    Jb = (1 / 3) * SprWid^3 * SprThi * (1 - (192 / (pi)^5) * SprWid / SprThi *
    SigFunc2);                          % Torsion constant of thigh
    Sga = Ja * TorsionModulus;          % Torsional stiffness of shin
    Sgb = Jb * TorsionModulus;          % Torsional stiffness of thigh
end

Iza = SprThi * SprWid^3/12; % Bending momentum of inertia of shin about z-axis
Izb = SprThi * SprWid^3/12; % Bending momentum of inertia of thigh about z-axis

if rem (NumofThigh, 2) == 0         % n = even for y- and z- axis movement
    ky = (48 * YoungsModulus * Izb * ( ( (Izb * ShinLeng / Iza) + ThighLeng) *
    NumofThigh^2 - 3 * ThighLeng * NumofThigh + 2 * ThighLeng)) /
    (ThighLeng^2 * ( ( (3 * (Izb * ShinLeng / Iza)^2 + 4 * (Izb * ShinLeng / Iza) *
    ThighLeng + ThighLeng^2) * NumofThigh^3) - (2 * ThighLeng * (5 * (Izb *
```

```
ShinLeng / Iza) + 2 * ThighLeng) * NumofThigh^2) + ( (5 * ThighLeng^2 + 6 *
(Izb * ShinLeng / Iza) * ThighLeng - 9 * (Izb * ShinLeng / Iza)^2) * NumofThigh)
- (2 * ThighLeng^2)));

kz = (48 * Sea * Seb * Sga * Sgb) / ( (Seb * Sga * ShinLeng^2 * (Sgb * ShinLeng
+ Sea * ThighLeng) * NumofThigh^3) - (3 * Sea * Seb * Sga * ShinLeng^2 *
ThighLeng * NumofThigh^2) + (Sea * ThighLeng * (2 * Seb * Sga * ShinLeng^2
+ 3 * Seb * Sgb * ShinLeng * ThighLeng + Sga * Sgb * ThighLeng^2) *
NumofThigh) - (Sea * Sga * Sgb * ThighLeng^3));

else        % n = odd for y- and z- axis movement
ky = (48 * YoungsModulus * Izb * ( ( (Izb * ShinLeng / Iza) + ThighLeng) *
NumofThigh - ThighLeng)) / ( (ThighLeng^2 * (NumofThigh - 1)) * ( ( (3 * (Izb
* ShinLeng / Iza)^2 + 4 * (Izb * ShinLeng / Iza) * ThighLeng + ThighLeng^2) *
NumofThigh) + (3 * (Izb * ShinLeng / Iza)^2) - (ThighLeng^2)));

kz = (48 * Sea * Seb * Sga * Sgb * (Sga * ThighLeng * (NumofThigh - 1) + Seb
* ShinLeng * NumofThigh)) / ( (Seb * Sga * ShinLeng^2 * (Seb * Sgb *
ShinLeng^2 + (Sea * Seb + Sga * Sgb) * ShinLeng * ThighLeng + Sea * Sga *
ThighLeng^2) * NumofThigh^4) - (Seb * Sga * ShinLeng^2 * ThighLeng * ( (3
* Sea * Seb + Sga * Sgb) * ShinLeng + 4 * Sea * Sga * ThighLeng) *
NumofThigh^3) + (Sea * ThighLeng * (2 * Seb^2 * Sga * ShinLeng^3 + (5 * Seb
* Sga^2 + 3 * Seb^2 * Sgb) * ShinLeng^2 * ThighLeng + 4 * Seb * Sga * Sgb *
ShinLeng * ThighLeng^2 + Sga^2 * Sgb * ThighLeng^3) * NumofThigh^2) - 2 *
Sea * Sga * ThighLeng^2 * (Seb * Sga * ShinLeng^2 + 2 * Seb * Sgb * ShinLeng
```

```
    * ThighLeng + Sga * Sgb * ThighLeng^2) * NumofThigh + Sea * Sgb *
    ThighLeng^2 * (Sga^2 * ThighLeng^2 - 3 * Seb^2 * ShinLeng^2));
end

if rem (NumofShin, 2) == 0          % n = even for x axis movement
    kx = (48 * YoungsModulus * Izb) * ( (3 * Izb * ShinLeng / Iza + ThighLeng) *
    NumofShin - ThighLeng) / ( (ShinLeng^2 * NumofShin) * ( ( (3 * (Izb * ShinLeng
    / Iza)^2 + 4 * (Izb * ShinLeng / Iza) * ThighLeng + ThighLeng^2) * NumofShin^3)
    - (2 * ThighLeng * (5 * (Izb * ShinLeng / Iza) + 2 * ThighLeng) * NumofShin^2)
    + ( (5 * ThighLeng^2 + 6 * (Izb * ShinLeng / Iza) * ThighLeng - 9 * (Izb *
    ShinLeng / Iza)^2) * NumofShin) - (2 * ThighLeng^2)));
else                                % n = odd for x axis movement
    kx = (48 * YoungsModulus * (1 / 12 * (SprThi * SprWid^3))) / (ShinLeng^2 *
    NumofShin * ( ( ( (Izb * ShinLeng / Iza) + ThighLeng) * NumofShin^2) - (3 *
    ThighLeng * NumofShin) + (2 * ThighLeng)));
end

SprConstant = kz;                   % Spring constant

%% Generation of input acceleration
h = 0.000001;                       % Sampling period
t = 0.000001:h:StopTime;            % Time specifications
```

```
% Generation of the input acceleration
InputAccFlag = 0;
while InputAccFlag == 0
  if TypeofInputAcc == 's'          % Sine wave
    InputAccFlag = 1;
    idx1 = t<0;
    idx2 = t>= (1 / (4 * AccFreq));
    InputAcc = AccMag * sin (2 * pi * AccFreq * (t)); % Make full sine wave
    InputAcc (idx1) = 0;            % Make acceleration 0 for t<0
    InputAcc (idx2) = AccMag;       % Make acceleration constant for t>=T/4
  elseif TypeofInputAcc == 't'      % Sawtooth wave
    InputAccFlag = 1;
    idx1 = t<0;
    idx2 = t>= (1 / (2 * AccFreq));
    InputAcc = AccMag * sawtooth (2 * pi * AccFreq * (t + 1 / (2 * AccFreq)));
    % Make full tooth wave
    InputAcc (idx1) = 0;            % Make acceleration 0 for t<0
    InputAcc (idx2) = AccMag;       % Make acceleration constant for t>=T/4
  elseif TypeofInputAcc == 'u'      % Step function
    InputAccFlag = 1;
    idx1 = t<0;
    idx2 = t>= 0;
    InputAcc = AccMag;              % Make constant input
    InputAcc (idx1) = 0;            % Make acceleration 0 for t<0
    InputAcc (idx2) = AccMag;       % Make acceleration constant for t>=T/4
```

```
    else
        disp ('wrong input, type again');
    end
end

%% Initial system; Damping coefficient
% Initial damping coefficient
Qpr = (1 + 6 * NKnudsen) / (1 + (1i * sqrt (SprConstant / ProofMass) * (Den *
(GapDist)^2 * (1 + 10 * NKnudsen + 30 * NKnudsen^2)) / (10 * Visco * (1 + 6 *
NKnudsen))));     % Relative flow rate coefficient

TempM = 20;
TempN = 20;
DampMat = zeros (TempM, TempN);
DampCoeff = zeros (size (t));
Qfactor = zeros (size (t));

for Tempm = 1:1:TempM
    for Tempn = 1:1:TempN
        Gmn = (pi ()^6 * (GapDist)^3 * ( (2 * Tempm - 1) * (2 * Tempn - 1))^2 / (768
        * Visco * ProofMassLeng * ProofMassWid) * ( ( (2 * Tempm - 1) /
        ProofMassLeng)^2 + ( (2 * Tempn - 1) / ProofMassWid)^2));
        Cmn = (pi ()^4 * (GapDist) * ( (2 * Tempm - 1) * (2 * Tempn - 1))^2) / (64 *
        PAmb * ProofMassLeng * ProofMassWid);
```

```
        TempDampCoeff = 1 / (Qpr * Gmn + 1i * sqrt (SprConstant / ProofMass) *
        Cmn);
        DampMat (Tempm, Tempn) = TempDampCoeff;
    end
end

DampCoeff (1) = real (sum (DampMat (:)));
Qfactor (1) = sqrt (ProofMass * SprConstant) / DampCoeff (1);

Contactflag = zeros (size (t));
Contactflag (1) = 1;


%% RK 4th - start
% Initialization
RK4 = @ (tVal, xVal, vVal, nVal) (ProofMass * InputAcc (nVal) - DampCoeff
(nVal) * vVal - SprConstant * xVal) / ProofMass;

x = zeros (size (t));
v = zeros (size (t));

x (1) = 0;                  % Initial position
v (1) = 0;                  % Initial velocity

% Iteration
```

```
for n = 1: (length (t) - 1)

    kx1 = v (n);
    kv1 = RK4 (t (n), x (n), v (n), n);

    kx2 = v (n) + h / 2 * kv1;
    kv2 = RK4 (t (n) + h / 2, x (n) + h / 2 * kx1, v (n) + h / 2 * kv1, n);

    kx3 = v (n) + h / 2 * kv2;
    kv3 = RK4 (t (n) + h / 2, x (n) + h / 2 * kx2, v (n) + h / 2 * kv2, n);

    kx4 = v (n) + h * kv3;
    kv4 = RK4 (t (n) + h, x (n) + h * kx3, v (n) + h * kv3, n);

    dx = h / 6 * (kx1 + 2 * kx2 + 2 * kx3 + kx4);
    dv = h / 6 * (kv1 + 2 * kv2 + 2 * kv3 + kv4);

    x (n + 1) = x (n) + dx;
    v (n + 1) = v (n) + dv;

% Damping coefficient for next iteration
    Qpr = (1 + 6 * NKnudsen) / (1 + (1i * sqrt (SprConstant / ProofMass) * (Den *
    (GapDist - x (n + 1))^2 * (1 + 10 * NKnudsen + 30 * NKnudsen^2)) / (10 * Visco
    * (1 + 6 * NKnudsen)))); %Relative flow rate coefficient
    TempM = 20;
```

```
TempN = 20;
DampMat = zeros (TempM, TempN);

for Tempm = 1:1:TempM
    for Tempn = 1:1:TempN
    Gmn = (pi ()^6 * (GapDist - x (n + 1))^3 * ( (2 * Tempm - 1) * (2 * Tempn -
    1))^2 / (768 * Visco * ProofMassLeng * ProofMassWid) * ( ( (2 * Tempm -
    1) / ProofMassLeng)^2 + ( (2 * Tempn - 1) / ProofMassWid)^2));
    Cmn = (pi ()^4 * (GapDist - x (n + 1)) * ( (2 * Tempm - 1) * (2 * Tempn -
    1))^2) / (64 * PAmb * ProofMassLeng * ProofMassWid);
    TempDampCoeff = 1 / (Qpr * Gmn + 1i * sqrt (SprConstant / ProofMass) *
    Cmn);
    DampMat (Tempm, Tempn) = TempDampCoeff;
    end
  end

  DampCoeff (n + 1) = real (sum (DampMat (:)));
  Qfactor (n + 1) = sqrt (ProofMass * SprConstant) / DampCoeff (n + 1);
  Contactflag (n + 1) = 1;

   if x (n + 1) > IniGap - (5e-9)
    % If the gap between contact metals is less than 5 nm, we assume it is
    contacted.
    v (n + 1) = - v (n + 1) * COR;
    x (n + 1) = IniGap - v (n + 1) * (x (n) - IniGap) / (v (n));
```

```
        Contactflag (n + 1) = 0;
    end

    RK4 = @ (tVal, xVal, vVal, nVal) (ProofMass * InputAcc (nVal) - DampCoeff
    (nVal + 1) * vVal - SprConstant * xVal) / ProofMass; % Renewal of the governing
    equation for the next iteration.

end

% Contact point evaluation
[~, locs] = find (Contactflag == 0, 1, 'first');
Contacttime = locs (end, end);

SimTime = toc; % Simulation time measurement end

%% Plot
note1 = msgbox ({['Simulation time = ' num2str(SimTime, 5) ' s'], ['Spring constant
= ' num2str(SprConstant, 5) ' N / m'], ['Time for full contact = ' num2str(Contacttime
* h, 5) ' s'], ['Threshold acceleration = ' num2str(InputAcc (Contacttime) / 9.81, 5) '
g']}, 'Simulation results');

set (note1, 'position', [950 400 250 80]); %[xPointLB yPointLB xLength yHeight]
```

```
figure

subplot (4, 1, 1);
plot (t, InputAcc)
grid on
title ('Input acceleration [m / s^2]')

subplot (4, 1, 2);
plot (t, x)
grid on
title ('Mass displacement [m]')

subplot (4, 1, 3);
plot (t, v)
grid on
title ('Velocity [m / s]')

subplot (4, 1, 4);
plot (t, DampCoeff)
grid on
title ('Damping coefficient [N * s / m]')

xlabel ('time (sec)
```

3. Fabrication of low-g MEMS acceleration switch

3.1. Overall fabrication process

Figure 3.1 shows the overall fabrication process of the proposed MEMS acceleration switch. The fabrication process of the proposed switch consists of a single SOI substrate and two glass substrates. The SOI substrate process consists of forming an insulating layer (Figure 3.1 S.a), forming a contact metal (Figure 3.1 S.b), and etching the device layer (Figure 3.1 S.c). The process of base glass substrate consists of glass etching process (Figure 3.1 G.a) for initial gap formation followed by two metal patterning processes (Figure 3.1 G.b and G.c). The prepared base glass substrate and the SOI substrate are anodically bonded, and sandblast process is proceeded on the glass side to form a cavity for electrical connection. Then, the thickness of the handling layer of the SOI substrate is adjusted through CMP (chemical mechanical polishing) process (Figure 3.1 B.a). The handling layer of the SOI substrate is patterned and etched using DRIE (deep reactive ion-etching) process to construct a proof mass having a high thickness (Figure 3.1 B.b). In the DRIE process, the BOX layer of the SOI substrate is used as the etch stop layer and prevent damages to the spring structure. This BOX layer is later removed and the switch structure is released (Figure 3.1 B.c). Meanwhile, the package glass substrate is wet-etched to form cavity for the switch structure (Figure 3.1 P.a). The SOI-base glass bonded substrate is anodically bonded with the package glass substrate (Figure 3.1 P.b). At last, shadow evaporation process is proceeded on the base glass side to form electrical path that connects the inside and the outside (Figure 3.1 P.c).

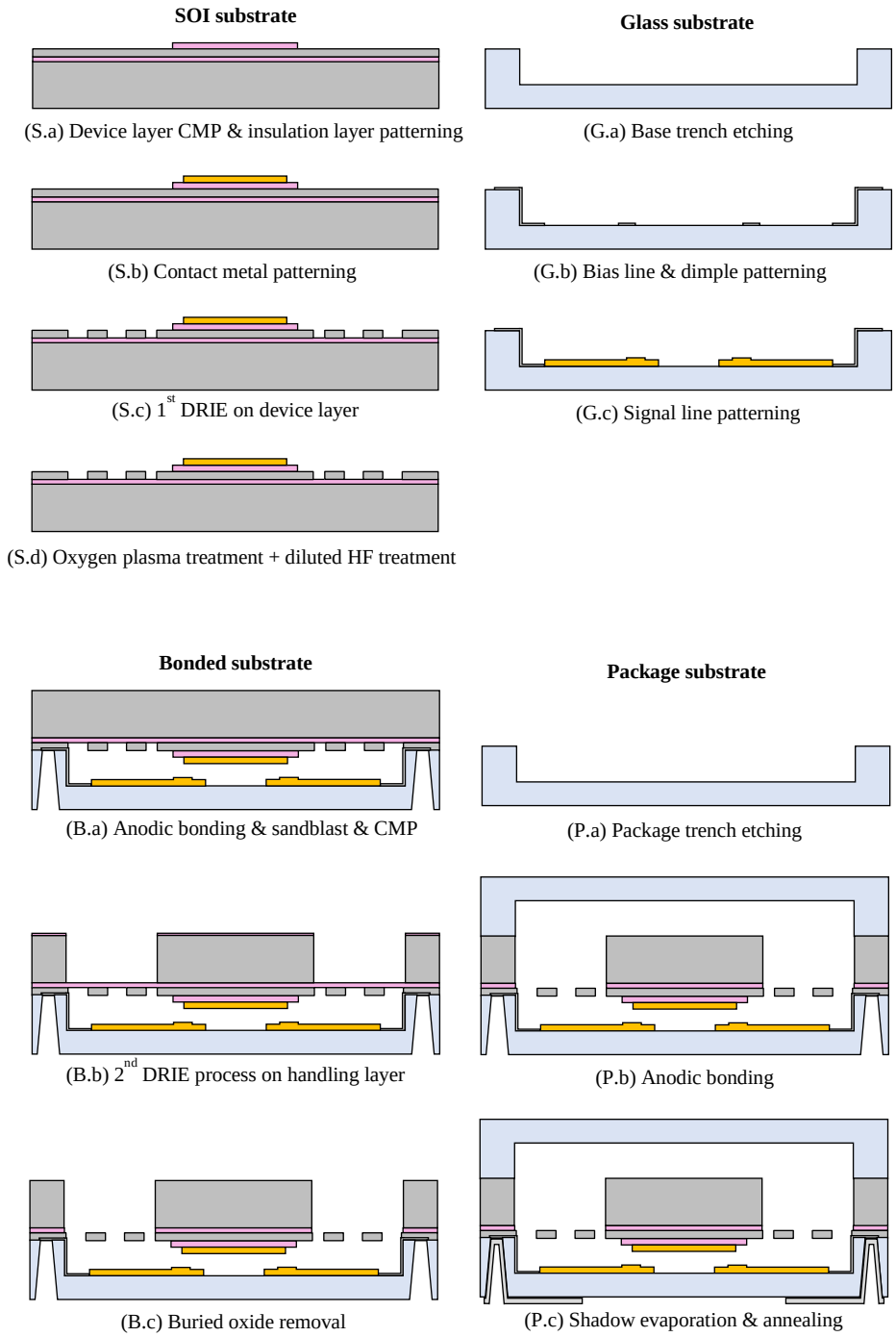

Figure 3.1. Overall fabrication process of the proposed MEMS acceleration switch.

3.2. Base glass substrate

On the base glass substrate, wet etching process was performed first in order to define the initial switching gap (Figure 3.1 G.a). 0.4 μm-thick poly silicon was used as an etch mask. The concentration of the etchant was adjusted to a ratio of HF (49%):NH_4F (40 wt%) = 1:1 since the etching rate of the hydrofluoric acid solution is very high (about 7 μm/min). At the room temperature, the etching rate was as low as 0.522 μm/min, which is low enough to adjust the etching depth. The etching time was 16 minutes and the etched trench had average depth of 8.355 μm. Figure 3.2 shows the (a) schematic and (b) fabrication results of base glass etching process.

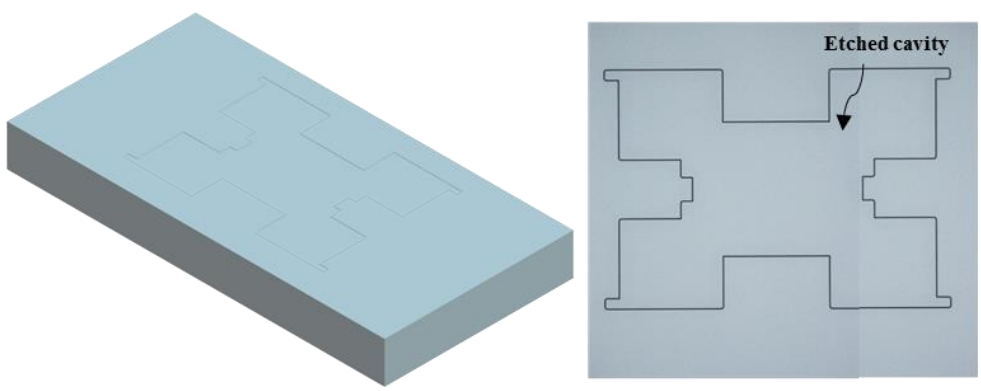

Figure 3.2. (a) Schematic and (b) fabrication result of base glass etching process.

The etched depths and metal thicknesses hereafter were all measured with profiler equipment (P-15, KLA-Tencor) except for spring thickness. Spring thickness was measured with SEM (scanning electron microscope equipment) equipment of S-4800, Hitachi. After wet etching process, poly silicon mask was removed completely with KOH etching at 80 °C. Next, bias line and dimple patterns were

created with evaporation process (Figure 3.1 G.b). The dimple patterns allow some portion of the bottom signal lines to protrude upward, thereby reducing the effective contact surface and the surface force generated during the contact. The surface force, which plays an important role in the contact characteristic, can be adjusted by modifying the height and area of the dimple patterns. The bias line was made of nickel and the average thickness was measured as 96.8 nm. Figure 3.3 shows the (a) schematic and (b) fabrication results of dimple & bias line formation process.

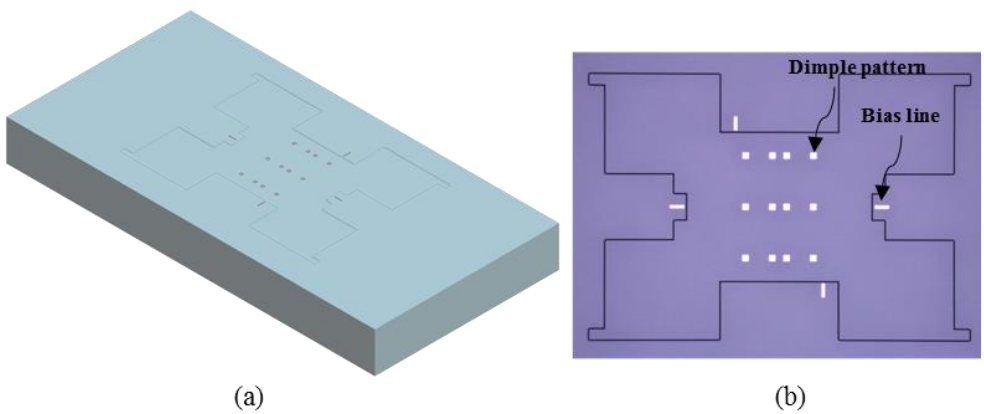

Figure 3.3. (a) Schematic and (b) fabrication result of dimple & bias line formation process.

Bottom signal lines were then patterned with another evaporation process (Figure 3.1 G.c). The bottom signal lines were formed of gold for intimate contact characteristics and the average thickness was measured as 696 nm. It should be noted that additional deposition of refractory metal, such as ruthenium or rhodium, can be performed on the gold signal line to improve the contact characteristics. Figure 3.4 shows the (a) schematic and (b) fabrication results of signal line / electrostatic operation pad / anti-stiction structure formation process.

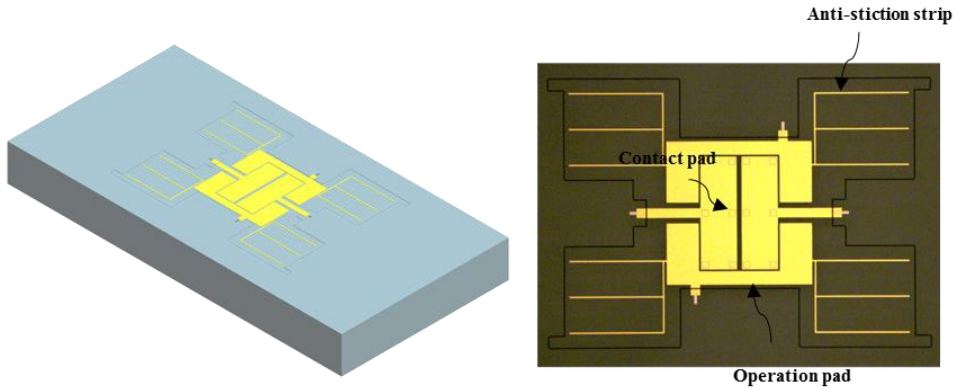

Figure 3.4. (a) Schematic and (b) fabrication result of signal line / electrostatic operation pad / anti-stiction structure formation process.

TABLE 3.1. Runsheet for base glass substrate.

#	**Process**	**Process detail**
10	Wafer preparation & Cleaning	Wafer: 500 μm-thick borosilicate glass (Poly-Si deposited on the both sides) / Poly-Si thickness : 4000 Å Cleaning: SC-1 (Standard cleaning-1), SC-2 (Standard cleaning-1), SPM (Sulfuric Peroxide Mixture)
20	Photolithography - Cavity etching	Equip.: MA6-III (SUSS) / TSA (Top Side Alignment) / PR: DNR-L300 (40) (4 μm thick-4000 rpm / 40 s) / Soft bake: 90 °C for 90 s / Exposure: 70 mJ / PEB (Post Exposure Bake): 100 °C for 90 s / Contact: Soft contact / Develop: 60 sec
30	Poly-Si RIE - Cavity etching	Equip.: AMS 200 I-Speeder (ALCATEL) / Target etch depth: > 4000 Å / Etching mask: DNR-L300 PR (40)
40	PR removal - Cavity etching	Acetone immersion in ultrasonicator (5 min) → SPM (10 min) → QDR (Quick Dump Rinse) (5 min) → SRD (Spin Rinse Dry)
50	Glass wet-etching - Cavity etching	Etchant: BHF (HF (49%) : NH_4F (40wt%) = 1 : 1) @ R.T. / Target etch depth: 4.5 μm / Etch mask: Poly-Si 0.4 μm / Etch rate: 0.522 μm/min / Cleaning: QDR (20 min) → SRD
60	Poly-Si wet-etching - Cavity etching	Etchant: KOH @ 80 °C Target etch depth: > 4000Å / Etch rate: 11 nm/min Cleaning: QDR (5 min) → SRD
70	Photolithography - Bias line	Equip.: MA6-III (SUSS) / TSA / PR: DNR-L300 (40) (6 μm thick-2000 rpm / 40 s) / Soft bake: 90 °C for 90 s / Exposure: 100 mJ / PEB: 100 °C for 100 s / Contact: Soft / Develop: 70 sec
80	E-beam evaporation - Bias line	Equip.: ULVAC ei-5 (ULVAC) E-beam evaporation / Cr 200Å + Ni 800Å
90	PR removal - Bias line	Lift-off process
100	Photolithography - Bottom line	Equip.: MA6-III (SUSS) / TSA / PR: DNR-L300 (40) (6 μm thick-2000 rpm / 40 s) / Soft bake: 90 °C for 90 s / Exposure: 100 mJ / PEB: 100 °C for 100 s / Contact: Soft contact / Develop: 70 sec
110	E-beam evaporation - Bottom line	Equip.: ULVAC ei-5 (ULVAC) E-beam evaporation / Cr 150Å + Au 4850Å
120	PR removal - Bottom line	Lift-off process

3.3. SOI substrate

Firstly, insulation layer and contact metal were patterned sequentially on the device layer of the SOI substrate (Figure 3.1 S.a and S.b). The average thicknesses of the insulation layer and contact metal were 475 and 692 nm, respectively. The insulation layer serves to electrically shield the silicon and the contact metal in the electrostatic operation tests. Figure 3.5 shows the (a) schematic and (b) fabrication results of insulation layer and contact metal formation process.

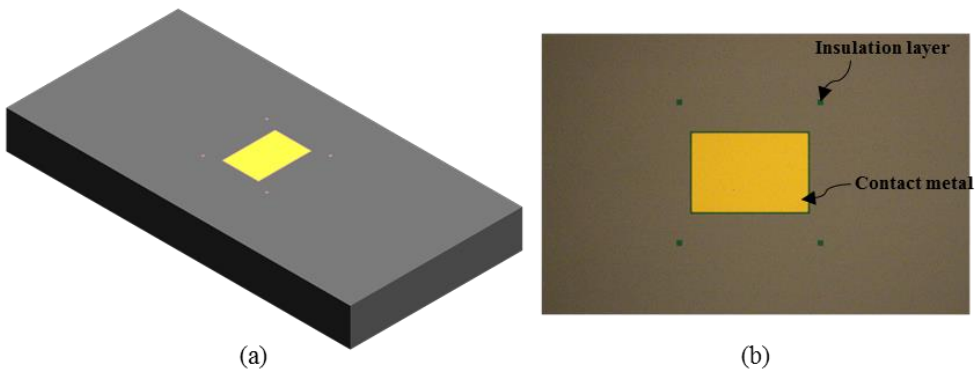

Figure 3.5. (a) Schematic and (b) fabrication result of insulation layer and contact metal formation process.

Then, the 1st DRIE process was carried out to define the spring pattern (Figure 3.1 S.c). The thickness of the spring is equal to the thickness of the device layer of the SOI substrate. The average thickness of device layer at top, center, bottom, right, and left points of the substrate was measured as 11.77 μm. Oxygen plasma treatment was carried out to remove the PERs (post etch residues) generated during the 1st DRIE process. Next, diluted HF (hydrofluoric acid) treatment was proceeded to eliminate the native oxide created during the oxygen plasma treatment (Figure 3.1

S.d). 1:30 BHF (buffered hydrofluoric acid) solution was used and the process time was controlled to be 1 minute to minimize the damage to the exposed BOX (buried oxide) layer. This process should be done right before the 1st anodic bonding process because native oxide film may be formed if left for a long time. Figure 3.6 shows the (a) schematic and (b) fabrication results of the 1st DRIE and post cleaning process.

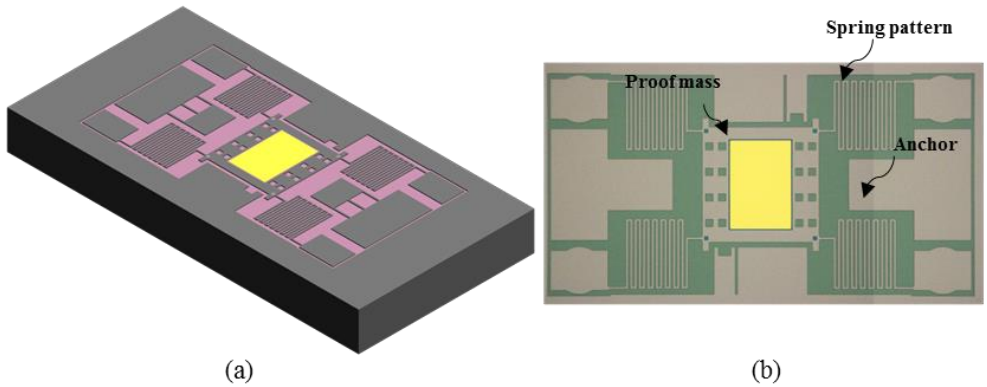

Figure 3.6. (a) Schematic and (b) fabrication result of the 1st DRIE and post cleaning process.

TABLE 3.2. Runsheet for SOI substrate.

#	**Process**	**Process detail**
10	Wafer preparation - CMP & Cleaning	Wafer: 450-1-12.5 μm SOI (silicon-on-insulator) SSP * Thickness of the device layer determines the thickness of the spring.
20	TEOS deposition - Insulation layer	Equip.: P-5000 / PECVD / Target thickness: 4000 Å
30	Photolithography - Insulation layer	Equip.: MA6-III (SUSS) / TSA / PR: AZ4620 (5 μm thick-5000 rpm / 40 s) / Soft bake: 100 °C for 180 s / Exposure: 150 mJ / no PEB / Contact: Soft contact / Develop: 280 sec
40	TEOS dry-etching - Insulation layer	Equip.: P-5000 / Target etch depth: > 4000 Å / Etching mask: AZ4620 PR
50	PR removal - Insulation layer	Acetone immersion in ultrasonicator (10 min) → IPA (5 min) → QDR (5 min) → SRD → Ashing (550 W x 10 min)
60	Photolithography - Contact metal mold	Equip.: MA6-III (SUSS) / TSA / PR: DNR-L300 (40) (4 μm thick-4000 rpm / 40 s) / Soft bake: 90 °C for 90 s / Exposure: 70 mJ / PEB: 100 °C for 90 s / Contact: Soft contact / Develop: 70 sec
70	E-beam evaporation - Contact metal	Equip.: ULVAC ei-5 (ULVAC) / E-beam evaporation / Cr 150Å + Au 6850Å
80	PR removal - Contact metal	Lift-off process
90	Photolithography - 1st DRIE (Spring)	Equip.: MA6-III (SUSS) / TSA / PR: DNR-L300 (30) (2 μm thick-2000 rpm / 40 s) / Soft bake: 100 °C for 90 s / Exposure: 200 mJ / PEB: 100 °C for 90 s / Contact: Soft contact / Develop: 60 sec
100	Silicon dry-etching - 1st DRIE (Spring)	Equip.: AMS 200 I-Speeder (ALCATEL) / Target etch depth: > 20 μm / Etching mask: DNR-L300 PR
110	PR removal - 1st DRIE (Spring)	Acetone immersion with agitation (10 min) → IPA (5 min) → SPM (10 min) and ashing → QDR (5 min)
120	Surface treatment - Native oxide removal	For SOI substrate only: - 1:30 BHF immersion (1 min) to remove native oxide created during ashing

3.4. Bonded substrate & packaging

The fabricated SOI and base glass substrates were cleaned and then anodically bonded together in a vacuum condition. The reason for applying vacuum condition in this bonding process is to keep the pressure in the space between SOI and base glass substrates similar to the chamber pressure in the subsequent DRIE process. In the bonding process, a small piece of aluminum foil was used to apply the bonding voltage to the device layer of the SOI substrate. Figure 3.7 shows the schematic of such bonding process. This bonding method was applied in the packaging bonding process as well.

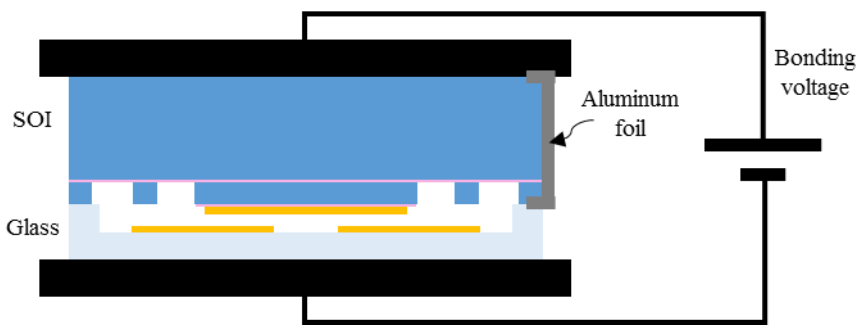

Figure 3.7. Schematic of anodic bonding process using aluminum foil.

Then, sandblast process was performed to create the cavities through the base substrate. The depth of the blasted-cavity was set deep enough to penetrate the device layer of SOI substrate. These cavities provide space for electrical connection between signal lines and the outer electrode of the base glass. Then CMP process was proceeded to adjust the thickness of the proof mass (Figure 3.1 B.a). To obtain 10 g threshold, the thickness of the proof mass was adjusted to 180 μm. Next, the proof mass was formed with the 2nd DRIE process (Figure 3.1 B.b). Since the BOX

layer acts as an etch stop layer, the spring structures remained undamaged throughout the etching process. One important thing to note is that the BOX layer will immediately tear when the substrate is taken out from the DRIE process chamber. This is because sudden pressure change occurs across the BOX layer when the substrate is taken out. If further DRIE is performed after this, silicon etching gas would enter through the torn gaps and will damage the spring structures. Therefore, the 2nd DRIE process should be completed at once, i.e., without taking out the substrate from the DRIE chamber before completely etching the handling layer. Figure 3.8 shows the (a) schematic and (b) fabrication results of the 2nd DRIE process.

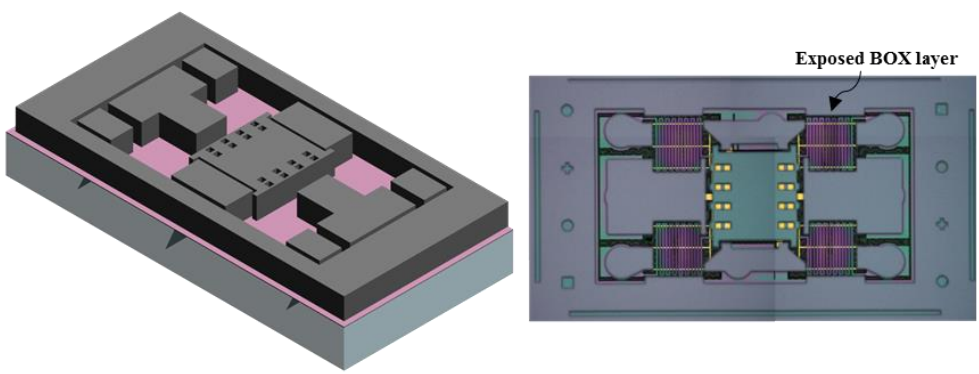

Figure 3.8. (a) Schematic and (b) fabrication result of the 2nd DRIE process.

Next, oxide RIE (reactive ion etching) process is proceeded to remove the exposed BOX layer and release the switch structure (Figure 3.1 B.c). Figure 3.9 shows the (a) schematic and (b) fabrication results of BOX layer removal process.

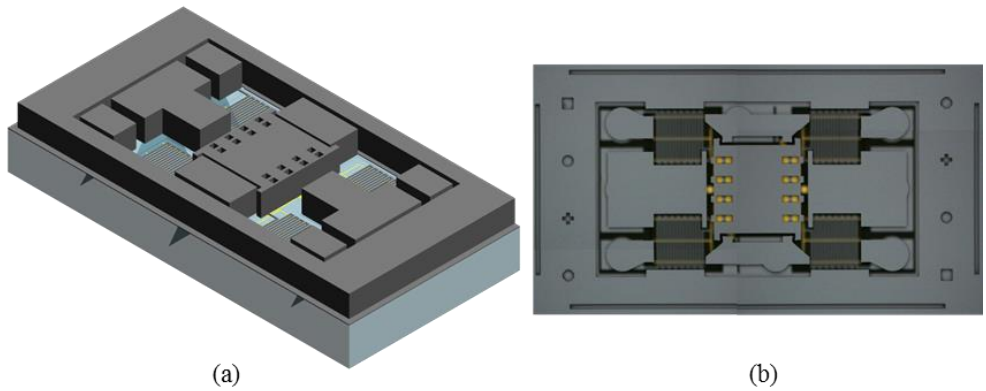

Figure 3.9. (a) Schematic and (b) fabrication result of BOX layer removal process.

SOI-glass bonded substrate was then anodically bonded with the packaging glass substrate, which contains trench for the proof mass (Figure 3.1 P.a & P.b). The bonding process was carried out in atmospheric condition to reduce the impact velocity of the contact. The depth of the package trench was set to 80 μm considering the electrostatic force generated during the anodic bonding process. Then BHF (buffered hydrofluoric acid) treatment was carried out to make the sandblasted surface of the base glass gentle. Next, shadow evaporation process was carried out on the bottom surface of the base glass to form aluminum electrodes that connect through the glass via (Figure 3.1 P.c). Figure 3.10 shows the (a) schematic and (b) fabrication results of package bonding and shadow evaporation process. Next, to reduce the resistance between aluminum and silicon interface, thermal annealing process was carried out at 340 °C for 4 hours. Finally, the fabricated switches were individualized through the dicing process. The size of the switch was measured as 2150 × 4240 × 1180 μm^3 (width × length × height).

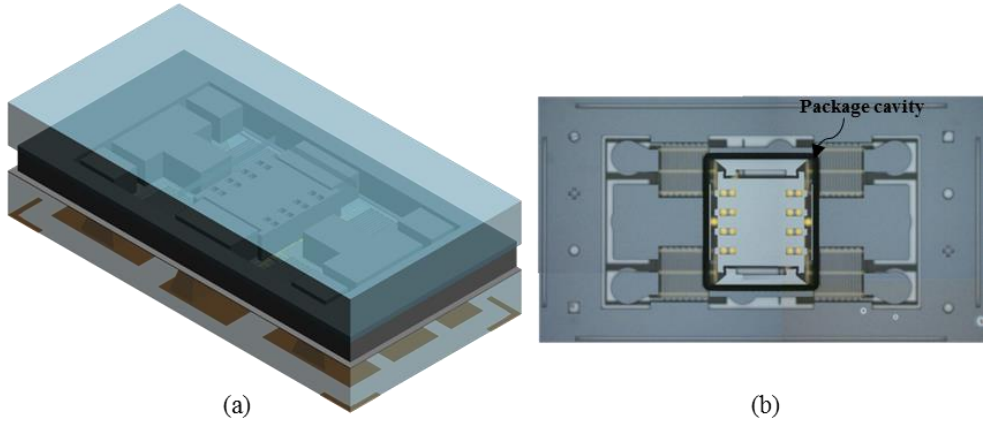

Figure 3.10. (a) Schematic and (b) fabrication result of package bonding and shadow evaporation process.

TABLE 3.3. Runsheet for SOI-base glass substrate.

#	**Process**	**Process detail**
10	Wafer preparation - Cleaning	For both of the fabricated substrates: - ACE (5 min) → IPA (5 min) → QDR (5 min) → SRD
20	Wafer bonding	Equip.: Wafer bonder (EV620) / Temp. max.: 340 °C / Vol. max.: 300 V / Tool force: 1000 N / Chamber pressure: 1e-02 Torr
30	Sandblast	- Sandblasting process on the base glass side. - After the complete penetration of the glass substrate, additional sandblasting process is necessary to expose the device layer of the SOI substrate out.
40	CMP	- CMP process on the SOI side (handling layer). - The polishing thickness must be calculated before CMP. - The mass of the proof mass is determined in this step. - To attain a specific threshold acceleration, one should consider the fabrication values such as etched glass and thicknesses of the insulation layer and metal layers. - Target thickness of proof mass: 180 μm (device + handling layers)
50	Cleaning	SPM (10 min) → QDR (5 min) → SRD
60	TEOS deposition - 2nd DRIE (Device)	Equip.: P-5000 / Target thickness: > 2.5 μm (Experimental etch ratio of TEOS and Si in the DRIE equip.: TEOS : Si = 1:85)
70	Photolithography - 2nd DRIE (Device)	Equip.: MA6-III (SUSS) / BSA (Back Side Alignment) / PR: DNR-L300 (30) (2 μm thick-2000 rpm / 40 s) / Soft bake: 100 °C for 90 s / Exposure: 200 mJ / PEB: 100 °C for 90 s / Contact: Soft contact / Develop: 60 sec
80	TEOS dry-etching - 2nd DRIE (Device)	Equip.: P-5000 / Target etch depth: > 2.5 μm / Etching mask: DNR-L300 PR
90	Silicon dry-etching - 2nd DRIE (Device)	Equip.: AMS 200 I-Speeder (ALCATEL) / Target depth: > 180 μm / Etching mask: TEOS (2.5 μm) - Exposed handling layer of SOI should be removed completely. - Over-etching is necessary in the consideration of loading effect in DRIE.
100	Oxide mask and BOX removal - 2nd DRIE (Device)	Equip.: P-5000 / Target etch depth: > 2.5 μm / Etching mask: none (complete removal)

TABLE 3.4. Runsheet for package glass substrate.

#	**Process**	**Process detail**
10	Wafer preparation - Cleaning	Wafer: 500 μm-thick borosilicate glass (Poly-Si deposited on the both sides) / Poly-Si thickness : 4000 Å Cleaning: SC-1, SC-2, SPM
20	Photolithography - PKG cavity	Equip.: MA6-III (SUSS) / TSA / PR: DNR-L300 (30) (2 μm thick-2000 rpm / 40 s) / Soft bake: 100 °C for 90 s / Exposure: 200 mJ / PEB: 100 °C for 90 s / Contact: Soft contact / Develop: 60 sec
30	Poly-Si RIE - PKG cavity	Equip.: AMS 200 I-Speeder (ALCATEL) / Target etching depth: > 4000 Å / Etching mask: DNR-L300 (30)
40	PR removal - PKG cavity	Acetone immersion in ultrasonicator (5 min) → SPM (10 min) → QDR (5 min) → SRD
50	Glass wet-etching - PKG cavity	Etchant: HF 49 wt% @ R.T. / Target etch depth: 80 μm / Etch mask: Poly-Si 0.4 μm / Etch rate: about 6 μm/min / Cleaning: QDR (20 min) → SRD
60	Poly-Si wet-etching - PKG cavity	Etchant: KOH @ 80 °C Target etch depth: > 4000Å / Etch rate: 11 nm/min Cleaning: QDR (5 min) → SRD

TABLE 3.5. Runsheet for packaging and thermal treatment.

#	**Process**	**Process detail**
10	Wafer preparation - Bonding surface treatment	Bonded substrate - Oxygen plasma treatment (Equip.: TEPLA 1 / Recipe: RF power 350 W, Oxygen 3 ml / min, Time: 15 min) Package glass substrate - SPM (10 min) → QDR (5 min) → SRD
20	Wafer bonding	Equip.: Wafer bonder (EV620) / Temp. max.: 340 °C, Vol. max.: 300 V / Tool force: 1000 N / Chamber pressure: 780 Torr * Slice of aluminum foil is used to apply the bonding voltage to the handling layer of SOI wafer.
30	BOE treatment	BOE (6:1) immersion for 10 min → cleaning Cleaning: DIW cleaning for 2 hrs → manual drying * Manual drying is necessary since the released structure would break during SRD process.
40	Shadow evaporation	Thermal evaporation / Al > 6000 Å
50	Thermal treatment	Equip.: Wafer bonder (EV620) / Temp. max.: 340 °C, / Time: 4 hrs / Chamber pressure: atmospheric

3.5. Fabrication results

Figure 3.11 shows the SEM (scanning electron microscope) and optical images of the fabricated MEMS switches. The brighter part of the silicon in Figure 3.11 (d) is the part where the silicon and the package glass are not bonded, while the darker part is the boned part. The average value of initial switching gap was 6.3905 μm. The dimension of spring was measured with SEM equipment (S-4800, Hitachi). The average width and thickness of the spring were 11.38 and 11.77 μm, respectively (Figure 3.11 (b) and (c)). According spring constant was calculated as 3.29 N/m, which is lower than the designed value of 4.52 N/m. The mass of the proof mass was assumed to be the same as the design value of 307.38 μg. This is because the dimensions of the proof mass are very large relative to the fabrication error. The threshold acceleration calculated with the above values was 6.98 g. The drop in threshold acceleration was mainly due to the reduced spring constant. The accuracy of the spring pattern must be improved to accurately match the designed threshold acceleration value. Table 3.6 summarizes the designed and fabricated (average) values of the proposed MEMS acceleration switch.

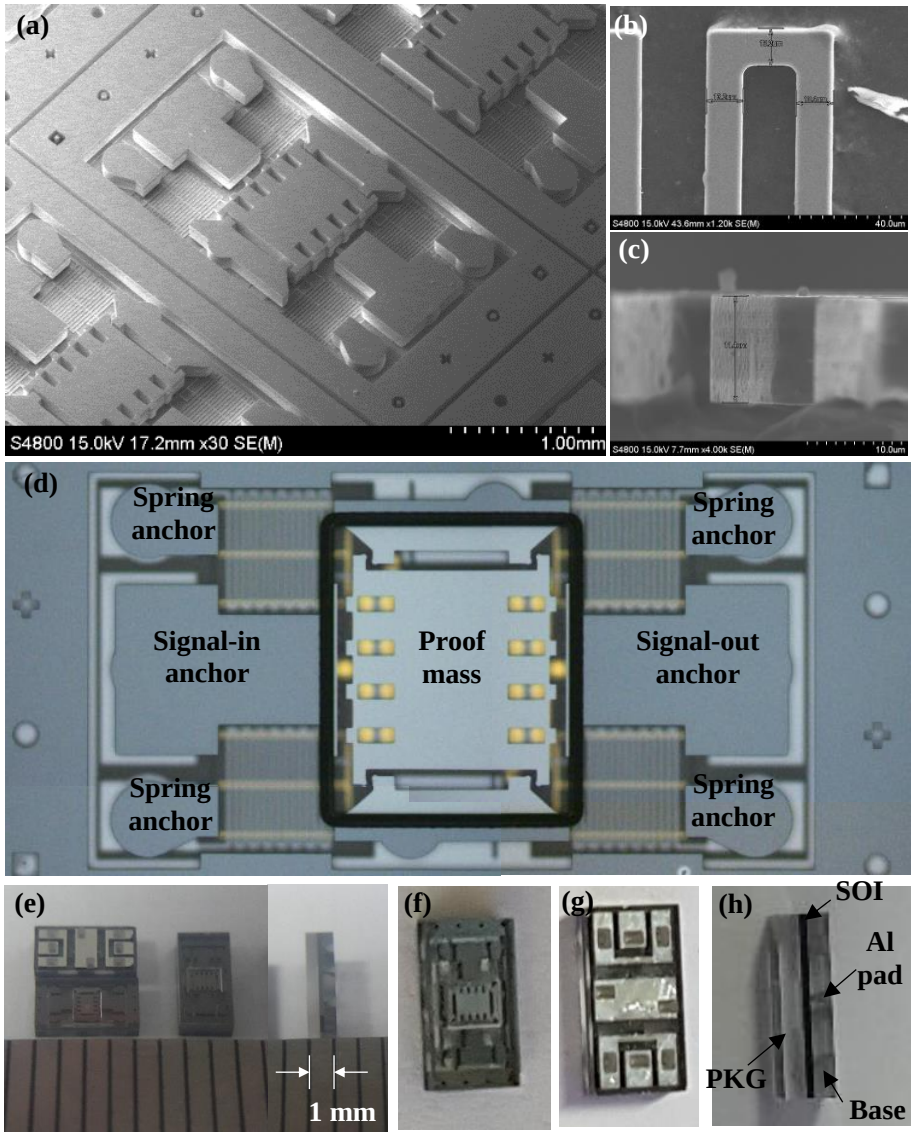

Figure 3.11. SEM images before packaging ((a), (b), and (c)) and optical images after packaging ((d), (e), (f), (g), and (h)); (a) perspective view, (b) serpentine spring (top view), (c) spring thickness, (d) top view (microscope), (e) size comparison with ruler (ruler marking spacing: 1 mm), (f) top view, (g) bottom view, and (h) side view of the of the packaged switch.

TABLE 3.6. Designed and fabricated values of the proposed MEMS switch.

Parts	Designed	Fabricated (average)
Base glass trench (μm)	8.5	8.355
Ni bias line thickness (nm)	100	96.8
Au signal line thickness (nm)	700	696.3
Au contact metal (nm)	700	692.9
Insulation layer (nm)	500	475.1
Initial gap (μm)	6.5	6.390
Thickness of the proof mass (μm)	180	180
The proof mass (μg)	307.38	307.38
Spring width (μm)	15.0	13.38
Spring thickness (μm)	12.5	11.77
Calculated spring constant (N/m)	4.52	3.29
FEM simulated spring constant (N/m)	4.46	3.19
Calculated threshold acceleration (g)	9.76	6.98
FEM simulated threshold acceleration (g)	9.62	6.76

The height profiles of the free-hanging proof masses were measured in $\hat{x}$- and $\hat{y}$-axes to see if the residual stress exists in the spring structure. Three switches were

selected and height differences were measured as shown in Figure 3.12. In Figure 3.12, points 1, 2, 3, 4, and 7 are for the proof mass and point 5 and 6 are for the anchor. Under the gravitational acceleration of 1 g, the proof mass moved downward about 1.05 μm and the resulting spring constant was calculated to be 3.01 N/m, which agrees well with the calculated spring constant above. Table 3.7 shows the summarized measurement results. The average height difference between the midpoints of the sides of the proof mass were 0.26 μm, which means that one side of the proof mass would come down 0.13 μm ahead than the other. This would results in 2% error in threshold acceleration value since the initial gap was 6.390 μm. The tilting angles of the proof mass in $\hat{x}$- and $\hat{y}$-axes were less than 0.05° and it was shown that the fabricated spring structure barely contains residual stress.

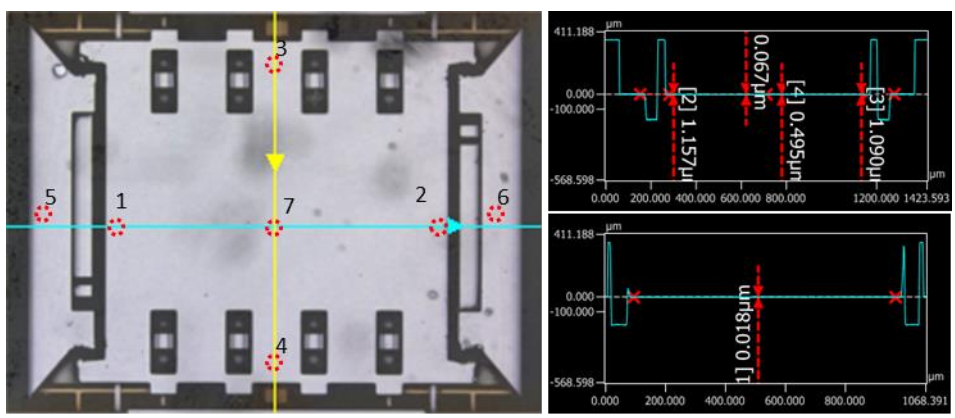

(a) (b)

Figure 3.12. Height profile measurement results of the fabricated MEMS switches under 1 g acceleration condition. Blue and yellow lines in (a) indicates the scanning line in $\hat{x}$- and $\hat{y}$-axes, respectively. Measured values are shown in (b).

TABLE 3.7. Height profiles of free-hanging proof masses.

Measuring points	1 & 2 (Horizontal tilting angle)	3 & 4 (Vertical tilting angle)	5 & 7	6 & 7
Sample 1	0.495 μm (0.035°)	0.018 μm (0.001°)	1.157 μm	1.19 μm
Sample 2	0.242 μm (0.017°)	0.652 μm (0.046°)	0.924 μm	0.963 μm
Sample 3	0.04 μm (0.002°)	0.113 μm (0.007°)	1.04 μm	1.06 μm
Average	0.26 μm (0.018°)	0.26 μm (0.018°)	1.04 μm	1.07 μm
STDEV	0.23 μm (0.0016°)	0.34 μm (0.024°)	0.12 μm	0.11 μm

4. Characterization of low-g MEMS acceleration switch

4.1. DC operation test & lifecycle test

Electrostatic operation tests were conducted for 32 samples and the operation voltages were measured as shown in Figure 4.1. The analytic pull-in voltage ($V_{pull-in}$) was calculated (Equation 4.1 [58]) with the measured dimensions and its value was 8.32 V. According to this, the switches should operate at 9 V, when the voltage was increased by 1 V. However, the majority of the switches operated at the voltage of 7 V. The difference between the analytic and measured value is thought to be the effect of the gravitational force (1 g). From the height profile measurement, it was revealed that the proof mass moves down about 1.05 μm under the gravitational acceleration. This would reduce the electrode gap (g) from 7.08 to μm 6.03 μm, which would reduce the pull-in voltage from 8.32 V to 6.54 V. Note that the electrode gap is the sum of the initial gap and thickness of insulation layer, contact metal, and signal line. In this situation, the fabricated switches should operate at 7 V. Note that the electrode gap is the sum of initial gap and thickness of the contact metal. The facing area (A) between the electrodes is 548,000 μm^2.

$$V_{pull-in} = \sqrt{\frac{8kg^3}{27\varepsilon A}} \qquad \text{(Equation 4.1)}$$

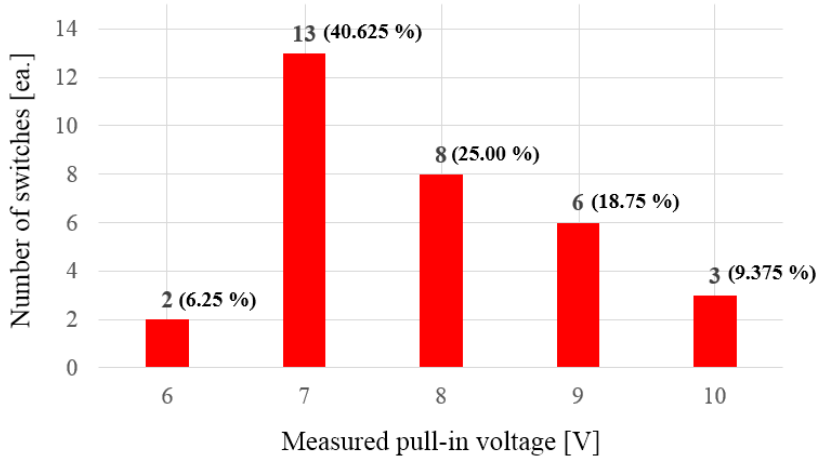

Figure 4.1. Measured operation voltages of the fabricated MEMS switches.

Figure 4.2 shows the variation of the spring constant and the pull-in voltage (under gravitational force condition) according to the thickness and width of spring structure. The range of thickness of the polished device layer was set from 10.5 to 15.5 μm. The variation in spring width was set from 12.0 to 14.5 μm. For each of thickness-width combination, spring constant was calculated using Equation 2.3. The minimum and maximum spring constants were obtained as 1.72 N/m and 5.22 N/m, respectively. Using these spring constants, the pull-in voltages, calculated by considering the gravitational acceleration, ranged between 4.8 V to 8.36 V. Since the variation of the spring constant is directly related to the uniformity of the operating characteristic of the switch, it is important to precisely control the dimensions of the spring pattern. For this, the accuracy and uniformity of the device layer CMP and the 1st DRIE process have to be enhanced in the future.

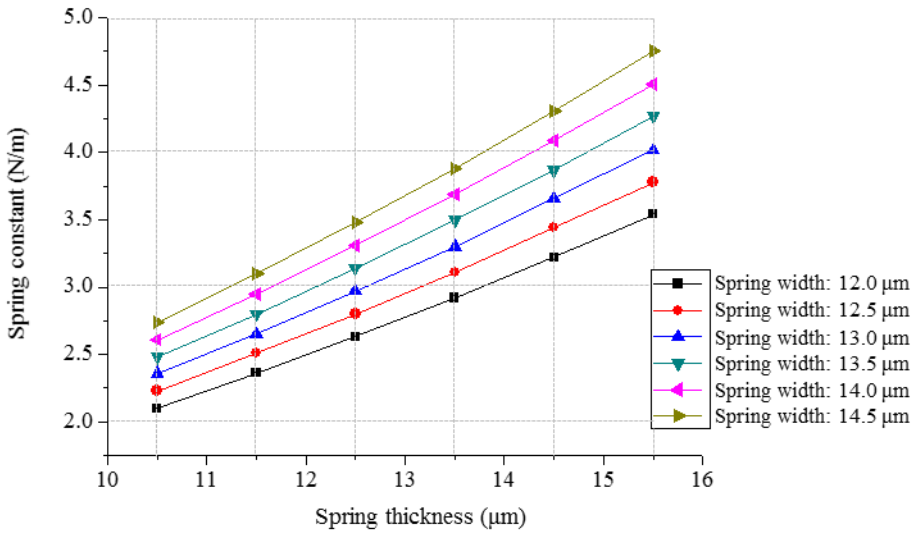

(a)

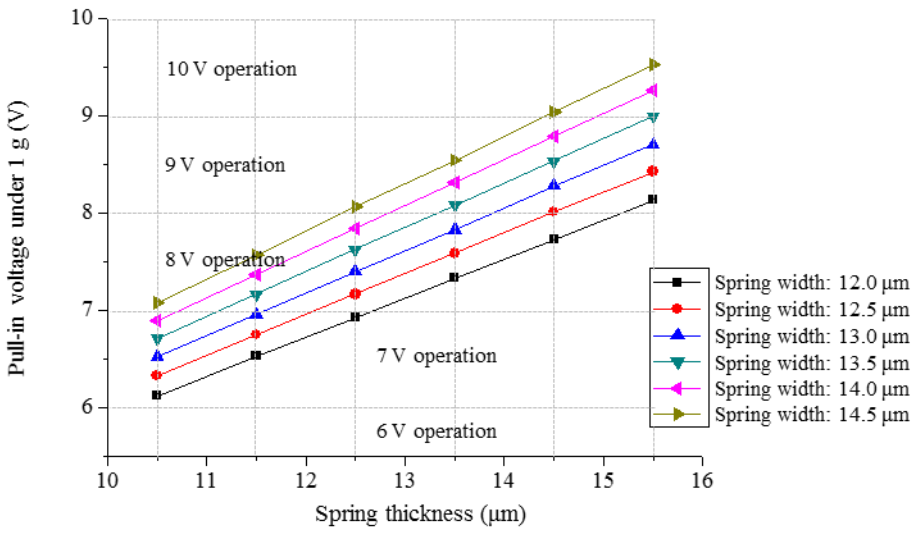

(b)

Figure 4.2. (a) Variation of spring constant and (b) pull-in voltage according to the thickness and width of the serpentine spring structure.

Figure 4.3 shows the estimated contact resistances ($R_{contact}$) at different contact forces. Contact force was calculated as the difference between the electrostatic force and the restoring force. The contact resistance was reduced as the

operation voltage is increased. The minimum contact resistance was estimated as low as 8.5 Ω at the operation voltage of 14 V. The corresponding contact force was 284 μN. After then, no further decrease in contact resistance was observed.

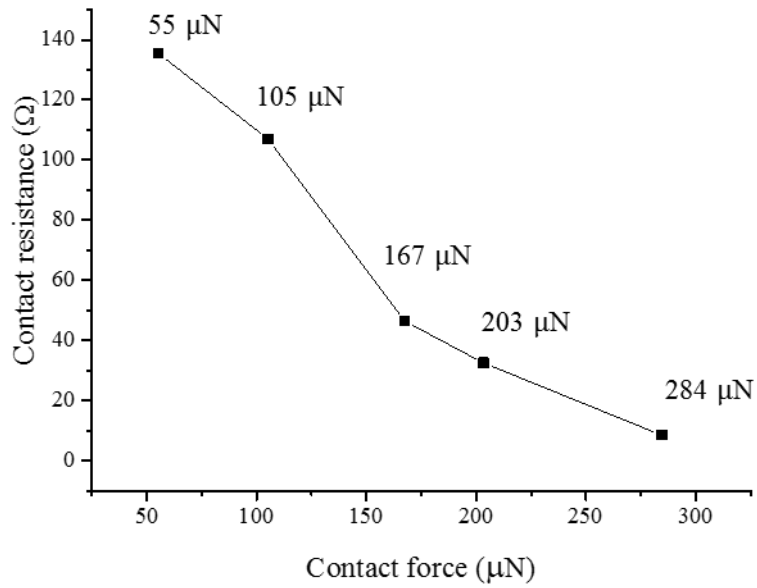

Figure 4.3. Estimated contact resistance according to the contact force.

The reason for the high contact resistance is thought be the result of the PERs (post etch residues) generated during the 2nd DRIE and oxide removal processes. According to T. Maruyama et al., the fluorocarbon polymer is generated and hardened on the metal surface by plasma during SiO_2 etching process. This metallic polymer is known not to be removed by O_2 plasma treatment [59]. During the fabrication process of the present study, the situation similar to described above occurs during the etching of the BOX layer of the SOI substrate (Figure 4.4).

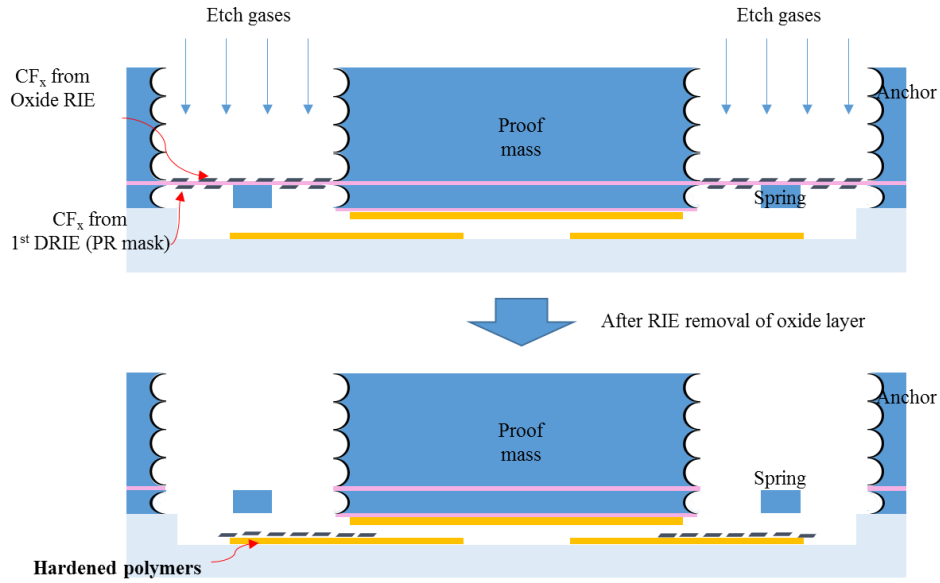

Figure 4.4. PERs (post etch residues) transferred to the metal surface during the 2nd DRIE process.

To confirm whether this phenomenon occurred, we examined the surface of the signal lines using EDX (energy dispersive x-ray spectroscopy). The results are shown in Figure 4.5. As a result of EDX measurement, it was confirmed that a large amount of carbon (C) and fluorine (F) were present on the surface of signal lines. The reason why the contact resistance is lowered as the contact force increases is that the polymers are compressed as the stronger force is applied and the effective contact area is increased accordingly. It should be noted that by using the load resistor with higher resistance in the readout circuit (such as in Figure 1.6, 4.7 or 4.14), one can obtain high output voltage regardless of the switch resistance.

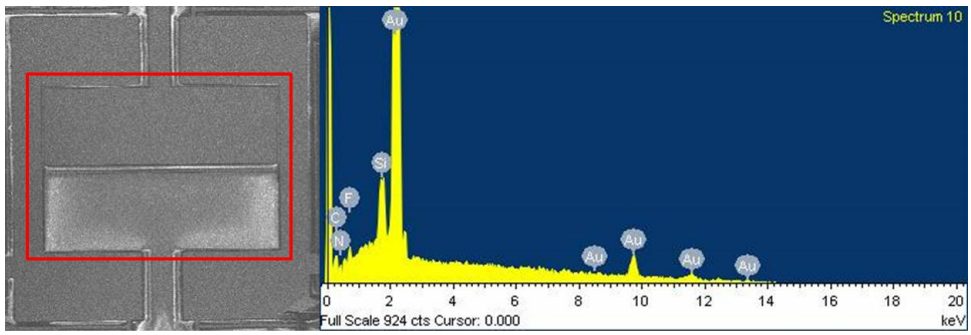

(a) (b)

Figure 4.5. EDX examination result of signal line patterned on the base glass substrate.

Next, lifecycle test was carried out. The fabricated sample was put into ceramic package and wire-bonded for electrical connection. Figure 4.6 shows the experimental scenes. A circuit using a microprocessor and transistor was constructed as shown in Figure 4.7. When the transistor turns on, the operation voltage (V_{op}) is fed to the operation electrode, and the MEMS switch is turned on. The status of MEMS switch was detected with the voltage across the load resistance (R_{Load}).

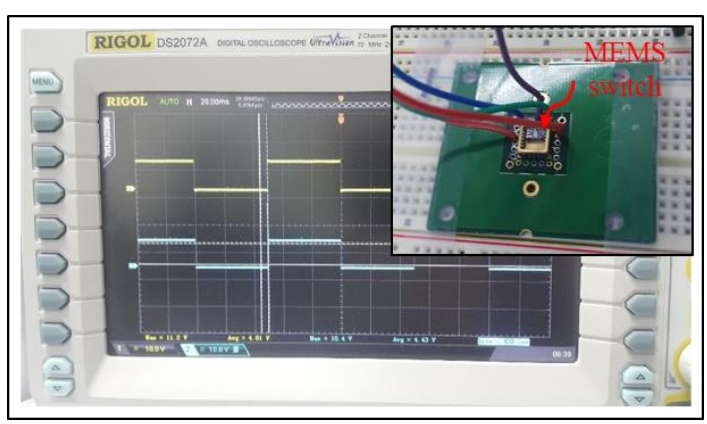

Figure 4.6. Experimental scene of the lifecycle. Yellow and blue lines on the oscilloscope indicate the operation and sensing voltages, respectively. Inset shows the fabricated switch in the ceramic socket with wire connection.

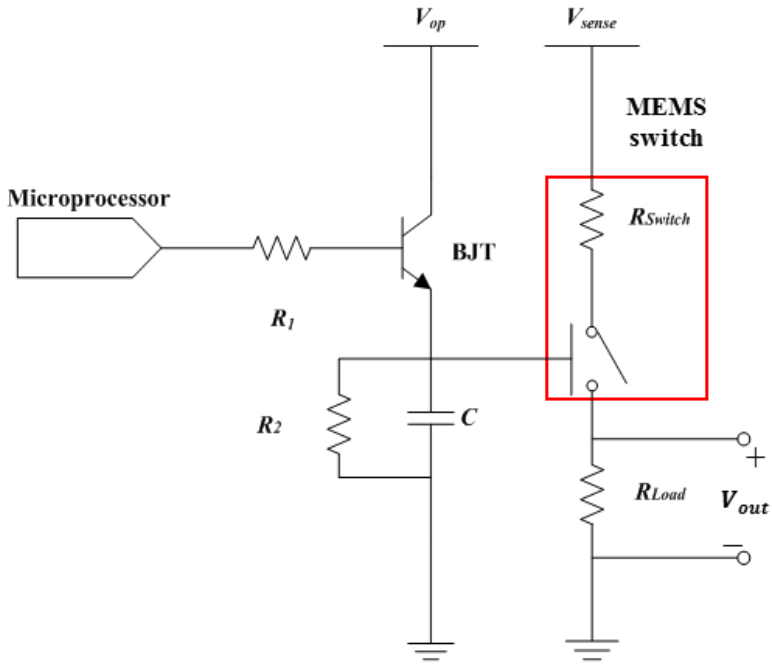

Figure 4.7. Circuitry for the lifecycle test.

From the lifecycle test, it was revealed that the fabricated MEMS switch could repeat operation over 10,000 cycles. Figure 4.8 shows some cycles at the beginning of the test. An operation voltage of 10 V was used in the experiment and the value of load resistance was measured as 219.7 Ω. The output voltage (V_{out}) was measured to be about 2 V when the sensing voltage of 5 V was applied. The switch resistance was then calculated by the voltage distribution and the resulting value was 329.5 Ω. Since the line resistance was as high as 150 Ohm, the contact resistance was then estimated to be 179.5 Ω.

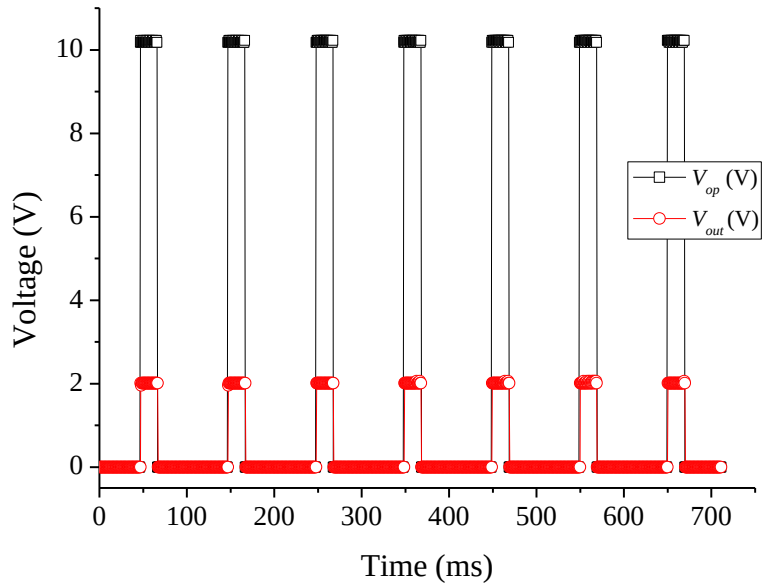

Figure 4.8. Lifecycle experiment result of the fabricated MEMS switch. Black square and red circle indicate the operation and output voltages, respectively.

Figure 4.9 is an enlarged view of the first switching-on period shown in Figure 4.8. Since the sampling time of the oscilloscope was 600 μs, the response time could not be obtained accurately, but it was shown that the response time was shorter than 1.2 ms. Figure 4.10 shows the variation of the contact resistance with the repeated operations. At the beginning of the test, the contact resistance was at the level of 190 Ω. However, although there was some fluctuation, the contact resistance was stabilized at about 150 Ω after 4,000 cycles.

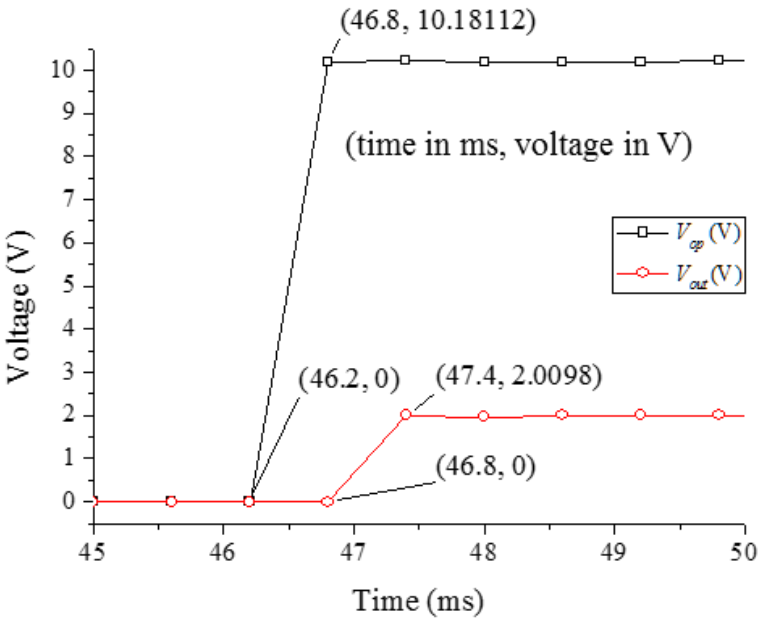

Figure 4.9. Enlarged view of the first switching (turning on) in Figure 4.8.

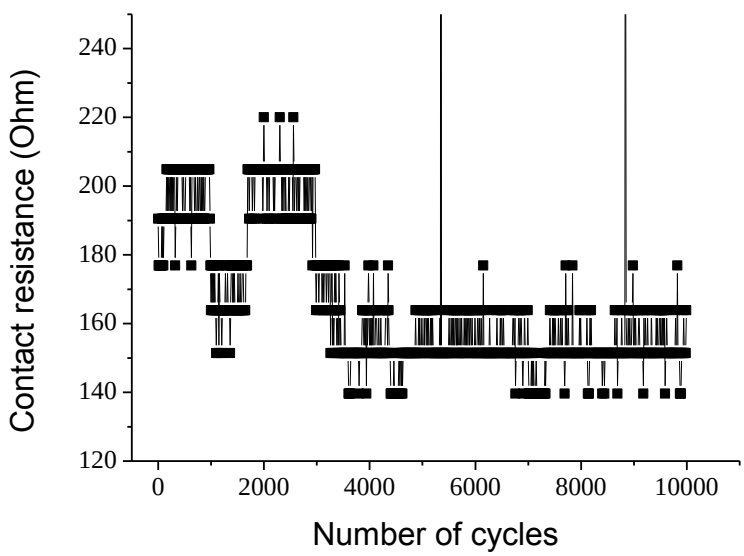

Figure 4.10. Variation of the contact resistance with the repeated operations.

4.2. Rotation-table experiments

Rotation-table experiments were conducted with the help of Microinfinity, Suwon, Korea. Figure 4.11 shows a specially manufactured socket for mounting the switch on the rotation-table. At the bottom of the upper case of the socket, there is a bumper pad, and this pad gently pushes the switch downward to make contact between switch's electrodes and socket pins.

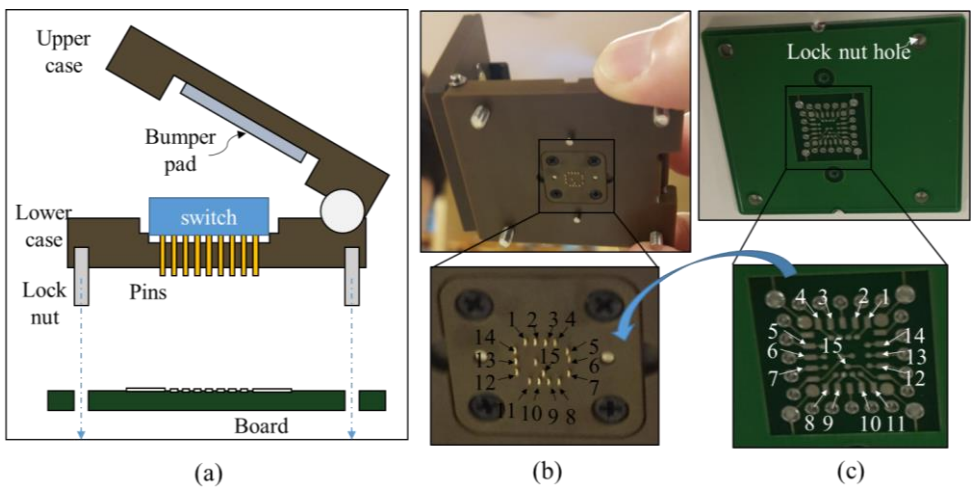

Figure 4.11. (a) Side view schematic of switch socket and board, (b) switch socket, and (c) printed circuit board.

The socket and the PCB are designed and manufactured to be able to receive and exchange the electrical signals by engaging with the switch fabricated above. Figure 4.12 shows (a) the topside (case opened) and backside of the socket and (b) the backside of the fabricated switch. Note that the orange-circled numbers denote pin map of the socket.

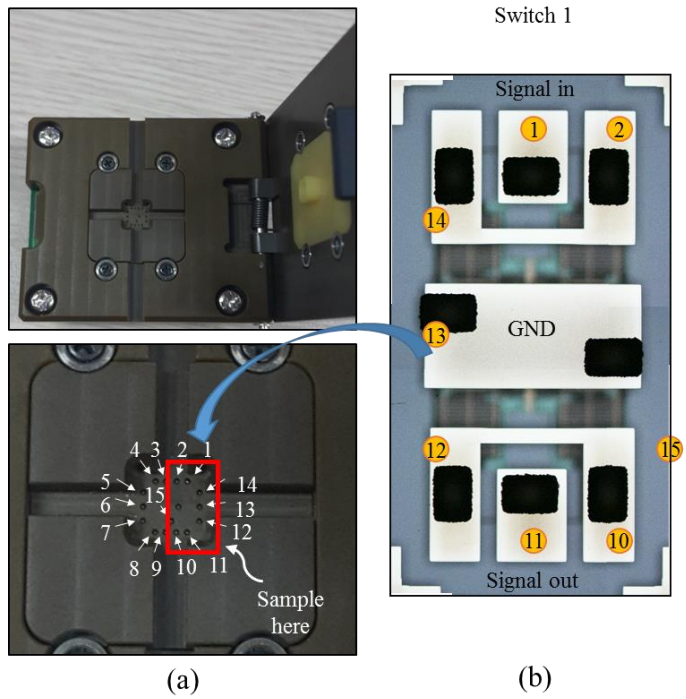

Figure 4.12 (a) Switch socket and (b) electrode of the fabricated switch.

The threshold acceleration of the fabricated switch was measured throughout the rotation-table experiment. A commercial accelerometer (ADXL326, Analog Devices) was installed at the same position with the MEMS switch to check the actual acceleration. Figure 4.13 shows the schematic of rotation-table experiment and the experimental scene. Note that the switch case and board were erected vertically for $\hat{z}$-axis movement of the proof mass.

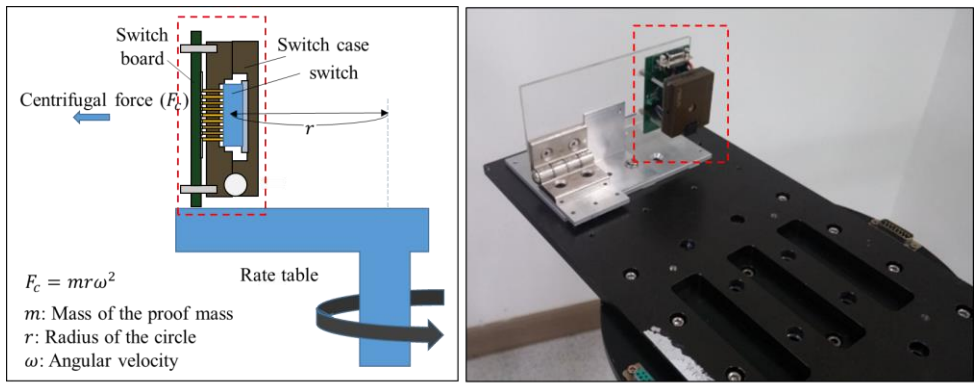

Figure 4.13. (a) Rotation-table test schematic and (b) experimental scene.

To observe the operation of the MEMS switch, sensing circuit was constructed as shown in Figure 4.14. Dashed red square indicates the MEMS acceleration switch. Signal-in and signal-out anchors of the switch were connected to signal-in and signal-out ports shown in Figure 4.14, respectively. When the switch turns on, the voltage divider circuit is constructed and the switch's state can be determined with the voltage level at the output. The output voltage (V_{out}) can be expressed in terms of the sensing voltage ($V_{sensing}$), load resistance (R_{load}), and the switch resistance (R_{switch}) as shown in Equation 4.2.

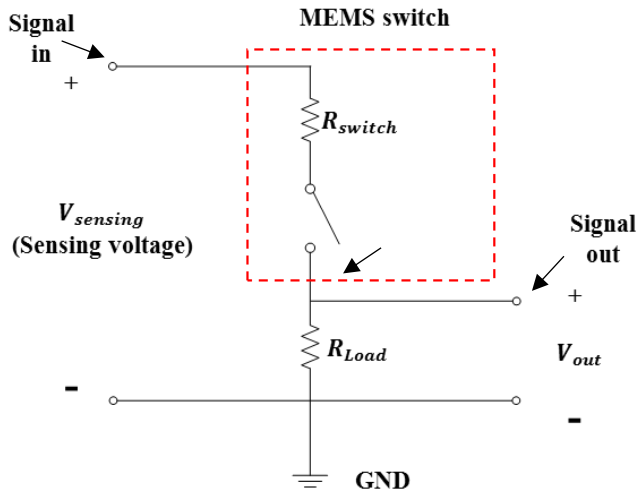

Figure 4.14 Sensing circuitry for MEMS acceleration switch.

$$V_{out} = V_{sensing} \frac{R_{load}}{R_{load} + R_{switch}} \quad \text{(Equation 4.2)}$$

The setup values used in the experiment are shown in Table 4.1. The values of sensing voltage and the load resistance were 5.057 V and 1.51 MΩ, respectively. It is preferred to set the value of the load resistance sufficiently high in order to obtain a constant output voltage regardless of the switch resistance value. The distance (r) between the MEMS switch and the center of the revolution was measured as 0.215 m. The rotation-table was accelerated with the average angular acceleration (α) of 35.95 rad/s^2 for 0.568 s to reach the final angular velocity (ω_{fin}) of 20.42 rad/s. The final centrifugal force [51] ($F_{c,fin}$) can be calculated with Equation 4.3 and the obtained value was 27.55 μN, which corresponds to the acceleration of 9.14 g.

$$F_{c,fin} = mr\omega_{fin}^2 \quad \text{(Equation 4.3)}$$

TABLE 4.1. Setup values used in the rotation-table experiment.

Parts	Symbol	Quantity	Value
Sensing out circuitry	$V_{sensing}$	Sensing voltage	5.057 V
	R_{load}	Load resistance	1.51 MΩ
Rotation-table	r	Radius of revolution	0.215 m
	α	Angular acceleration	35.95 rad/s^2 (or 2060 deg/s^2)
	ω_{fin}	Final angular velocity	20.42 rad/s
	t_r	Rising time of acceleration	0.568 s
	$F_{c,fin}$	Final centrifugal force	27.55 μN
	-	According final g-level	9.14

The measured output voltage at the on state was 5 V and it was revealed that the current flowing through the switch is about 3.3 μA. From the experiment, it was revealed that the fabricated switch operates when the applied acceleration exceeds 6.61 g (Figure 4.15).

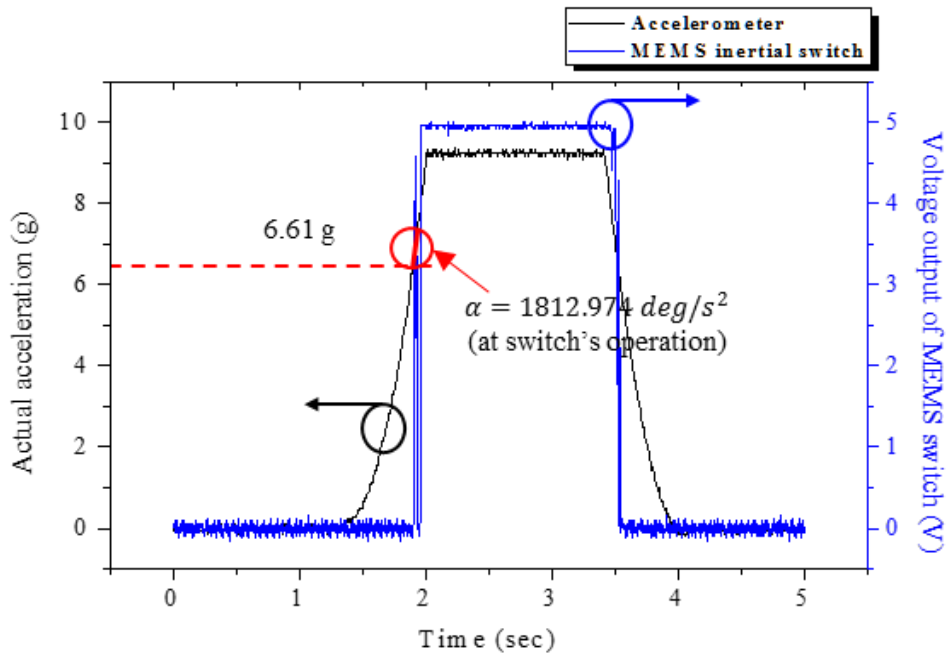

Figure 4.15. Actual acceleration (black line) and the voltage output of the fabricated MEMS switch (blue line).

Figure 4.16 shows a result of repeated rotation-table test with increased acceleration values. Both the output voltages of accelerometer and acceleration switch were read using oscilloscope in sync and the acceleration level was converted from the accelerometer's output voltage referring to Table 4.2. Table 4.2 lists commercial accelerometer's output voltage and corresponding acceleration levels calibrated in Microinfinity.

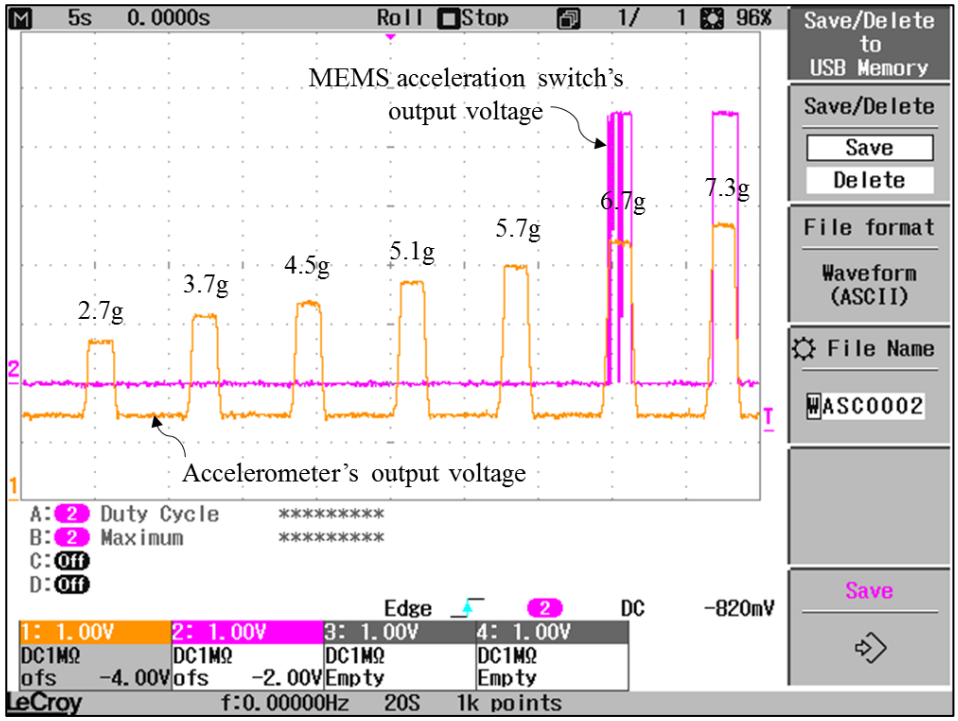

Figure 4.16. Result of the repeated rotation-table experiment with increased acceleration values.

Note that one horizontal and vertical side of the square represented by a grey dotted line in oscilloscope display correspond to 2 second and 1 Volt, respectively. Similar to the experimental result in Figure 4.15, the switch started operating when the input acceleration was about 6.7 g, but the resistance of the switch was found to vary greatly due to the lack of extra contact force. When the input acceleration was raised to 7.3 g, however, the switch showed reliable contact. In order to validate the measurements, nine switches were selected for additional test. The average and standard deviation of threshold acceleration of nine switches were measured as 6.53 g and 0.08 g, respectively.

TABLE 4.2. Lookup table for output voltage and applied acceleration.

Output voltage (V)	Corresponding acceleration (g)	Output voltage (V)	Corresponding acceleration (g)
1.5	0.00	4.5	6.82
1.7	0.45	4.7	7.27
1.9	0.91	4.9	7.73
2.1	1.36	5.1	8.18
2.3	1.82	5.3	8.64
2.5	2.27	5.5	9.09
2.7	2.73	5.7	9.55
2.9	3.18	5.9	10.00
3.1	3.64	6.1	10.45
3.3	4.09	6.3	10.91
3.5	4.55	6.5	11.36
3.7	5.00	6.7	11.82
3.9	5.45	6.9	12.27
4.1	5.91	7.1	12.73
4.3	6.36	7.3	13.18

4.3. Effect of the off-axis force on the operating acceleration

The error between the calculated (6.98 g) and the measured threshold acceleration (6.61 g) was 5.3 %. The main reason for this error is thought to be the tangential acceleration generated during the rotation-table experiment. As the rotation-table starts to rotate, acceleration occurs not only in the centrifugal direction but also in the tangential direction of the rotating circle. The Euler force [60], which occurs due to this tangential acceleration, acts in the lateral direction of the proof mass and can be expressed as Equation 4.4.

$$F_{Euler} = m\mathrm{a}_{Euler} = -m\frac{d\boldsymbol{\omega}}{dt} \times \boldsymbol{r} = -mr\alpha \qquad \text{(Equation 4.4)}$$

where a_{Euler} is the Euler acceleration or transverse acceleration. This lateral force will not only move but also tilt the proof mass because the springs are attached at the bottom of the proof mass. When the proof mass is tilted, the initial switching gap is reduced and the threshold acceleration will be also reduced. To verify this, we have simulated how much the initial switching gap is reduced due to the Euler force. The temporary value of angular acceleration was calculated using angular velocities at 0.01 s before and 0.01 s after the switch's operation. The resulting Euler force was calculated as 2.091 μN and the according reduction in the initial switching gap was simulated as 0.236 μm (Figure 4.17). The revised initial gap was 6.153 μm and the threshold acceleration of the switch was also revised to 6.512 g, which agrees very well with the previous measurement.

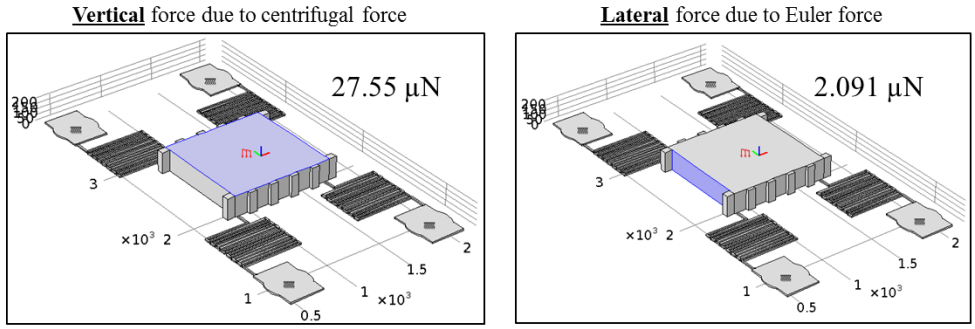

(a) (b)

Figure 4.17. Simulation setting: (a) centrifugal force and (b) Euler force acting on the proof mass during the rotation-table experiment.

To confirm whether the previous assumption is correct, the rotation-table experiment was repeated with different angular acceleration. In this experiment, we used another switch to verify that the same phenomenon occurs or not. Figure 4.18 shows the result of the rotation-table experiment with the angular acceleration (α) value of 117.462 deg/s^2 (at contact), or 2.05 rad/s^2, equivalently. All experimental conditions were kept the same as before and shown in Table 4.1, except for the angular acceleration and final g-level. To minimize the effect of Euler acceleration on the switch, the rotation-table was rotated with the angular acceleration as low as 117.462 deg/s^2. The according tangential force was calculated to be 1.3548E-07 N (Equation 4.4), and the displacement of the proof mass in the $\hat{z}$-direction was simulated to be about 15.3 nm, or 0.0153 μm, equivalently. In this case, it is assumed that this measure will be very similar to the original threshold acceleration of the switch because the reduction of the initial switching is very small.

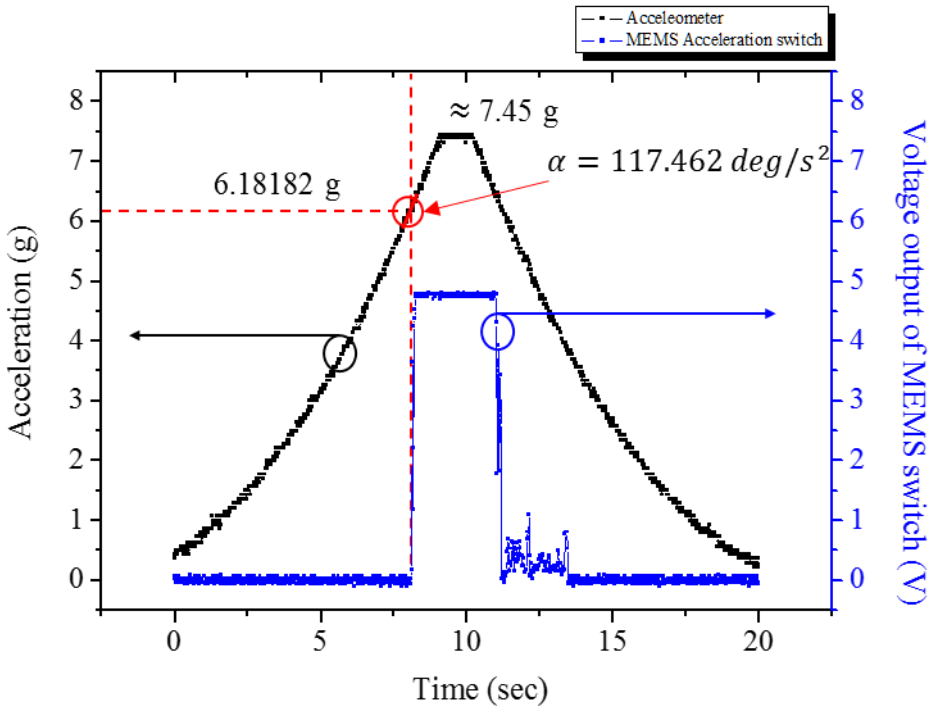

Figure 4.18. Rotation-table experiment result of another sample (angular acceleration = 117.462 deg/s^2, final g-level ≈ 7.45 g).

Figure 4.19 shows the result of operating the same switch with increased angular acceleration up to 877.723 deg/s^2. When assigned to the experimental values shown in Table 4.1, the angular acceleration of 877.723 deg/s^2 was calculated to generate a tangential force of 1.0124 μN. In this experiment, it was confirmed that the operating acceleration of the switch is lowered by the increased angular acceleration (i.e., tangential force).

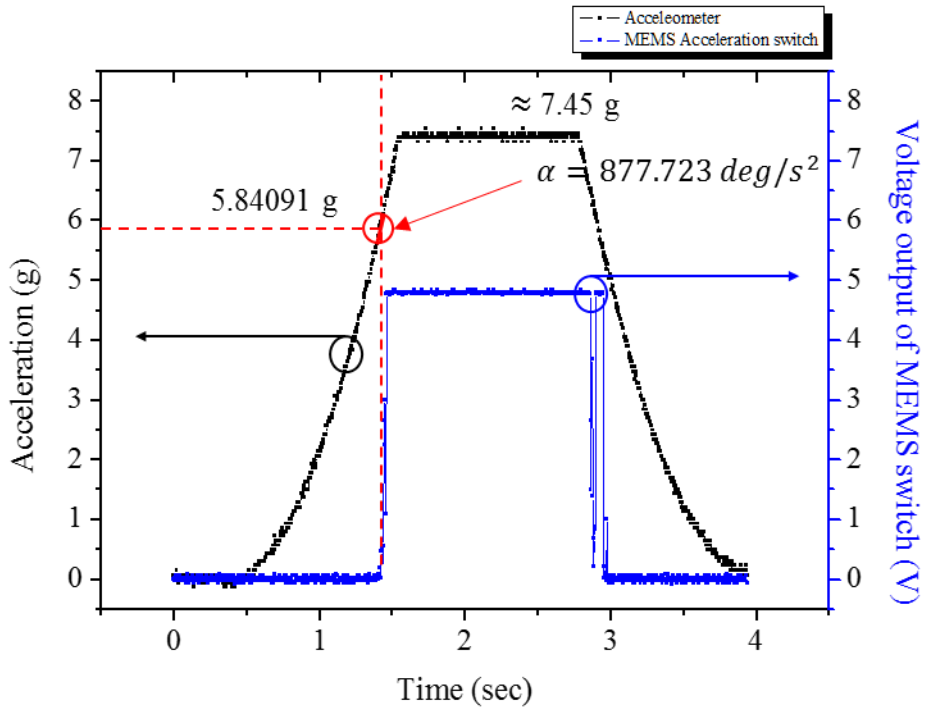

Figure 4.19. Rotation-table experiment result of another sample (angular acceleration = 877.723 deg/s^2, final g-level ≈ 7.45 g).

Figure 4.20 shows the result of experiment in which the angular acceleration is kept the same as in the experiment in Figure 4.19 and the final g-level is set to 6.31 g, which is similar to the original threshold acceleration of the tested switch. The operating acceleration of the switch was measured at 5.84 g as the same in the previous experiment. However, it was confirmed that the contact characteristics of the switch are very unstable in the section where the acceleration level is maintained at the final g-level (angular acceleration = 0). This is due to the fact that there is not enough extra force that helps the contact of the metals. Therefore, it can be seen that the acceleration slightly higher than the threshold acceleration is required for stable contact of the acceleration switch.

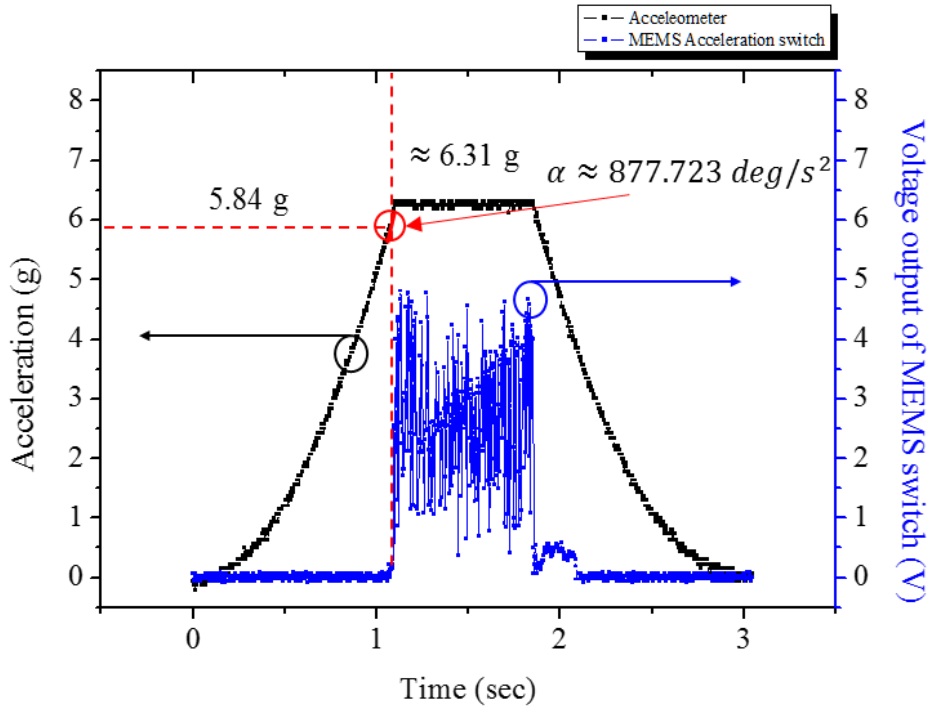

Figure 4.20. Rotation-table experiment result of another sample (angular acceleration ≈ 877.723 deg/s^2, final g-level ≈ 6.31 g).

Figure 4.21 shows the result of the rotation-table experiment in which the angular acceleration was increased to 1744.123 deg/s^2. As expected, the higher angular acceleration increased the tangential force, causing the switch to operate at a slightly lower value than the experiments before. The operating acceleration of the switch lowered to 5.75 g in this experiment. The tangential force generated on the rotation-table is a relatively small force at the μN level, but it is important to analyze it because a larger force can be applied in actual applications.

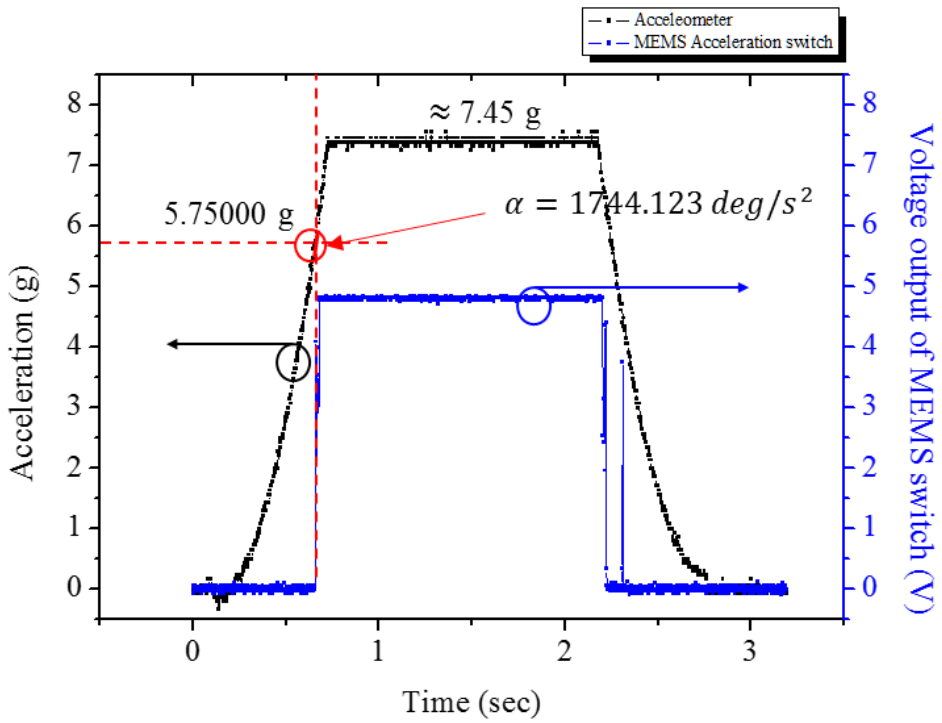

Figure 4.21. Rotation-table experiment result of another sample (angular acceleration = 1744.123 deg/s^2, final g-level ≈ 7.45 g).

Based on the results of the above experiments, we modeled the operating acceleration of the switch as to the off-axis force. Firstly, it should be reminded that the threshold acceleration of the switch (a_{th}) is the acceleration value at which the switch operates without disturbance (i.e., assuming no errors). Assuming that the error (ε, in g/μN) between the threshold and operating acceleration is proportional to the off-axis force ($F_{off-axis}$, in μN), the operating acceleration of the switch can be modeled as:

$$a_{operating,modeled} = a_{th} + \varepsilon F_{off-axis} \qquad \text{(Equation 4.5)}$$

To find out the values of threshold acceleration (a_{th}) and error due to the off-

axis force (ε), least squares method was used in this study. The least squares method is a kind of regression analysis used for data fitting when there are more equations (or measurements, i.e. data points) than unknowns. Least squares means that the overall solution minimizes the sum of the squares of the residuals made in the results of every single equation. A residual (r), which is the difference between an observed value and the fitted value of a model equation, can be equated as:

$$r = a_{operating,observed} - a_{operating,modeled} \quad \text{(Equation 4.6)}$$

$$r = a_{operating,observed} - (a_{th} + \varepsilon F_{off-axis}) \quad \text{(Equation 4.7)}$$

The overall sum of squared residuals is then defined as:

$$\sum_{i=1}^{n} r_i^2 = \sum_{i=1}^{n} [a_{operating,observed} - (a_{th} + \varepsilon F_{off-axis})]^2 \quad \text{(Equation 4.8)}$$

The minimum of the sum of squares is found by setting the gradient to zero, that is $\partial r / \partial a_{th} = 0$ and $\partial r / \partial \varepsilon = 0$. Two simultaneous equations are obtained from the previous equations and the resulting threshold acceleration (a_{th}) and error (ε) is 6.16325 g and -0.22693 g/μN, respectively. Thus the modeled operating acceleration is

$$a_{operating,modeled} = 6.16325 - 0.22693 F_{off-axis} \quad \text{(Equation 4.9)}$$

where the $F_{off-axis}$ is in the unit of μN. Figure 4.22 shows the calculation and

observed results of error due to off-axis force and the operating acceleration. To estimate the spring constant, the proof mass and initial gap was assumed to be the average measured values shown in Table 3.1 and their values are 307.38 μg and 6.39 μm, respectively. With the obtained threshold acceleration value above, the spring constant was estimated to be 2.90718 N/m. Referring to Figure 4.2, where the variation of spring constant due to the variation of the spring dimensions is plotted, this value is in the reasonable range.

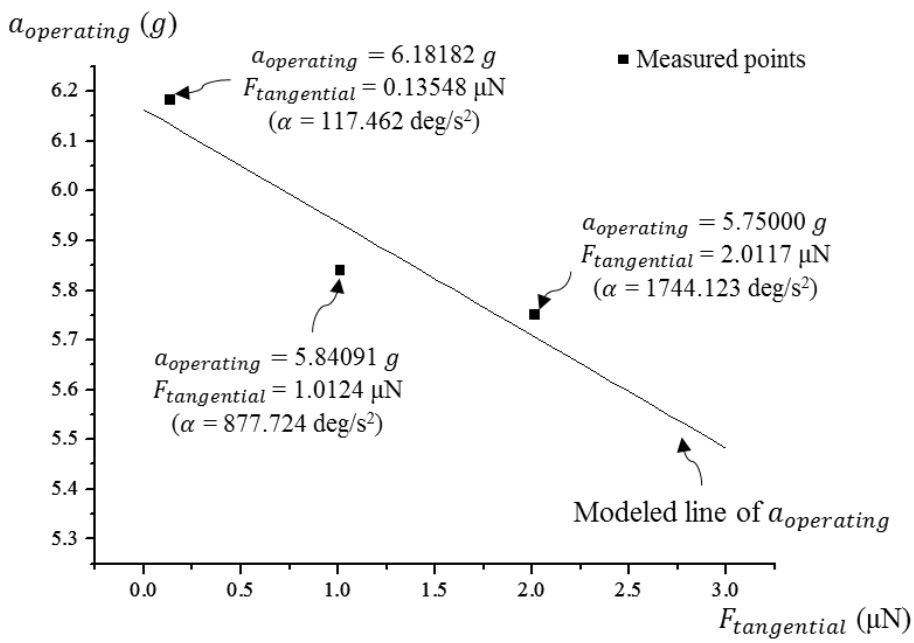

Figure 4.22. Observed (points) and modeled (line) operating acceleration of the tested MEMS acceleration switch.

Table 4.3 summarized the results of three experiments above and the calculation result. Note that the angular acceleration was calculated using the changes in angular velocities at 0.01 s before and 0.01 s after the switch's operation. Tangential forces for each angular velocity were calculated using Equation 4.4 and the $\hat{z}$-axis

displacement of the proof mass was obtained using FEM simulation. We calculated the narrowed gap and compared the measured values with the calculated values of the operating acceleration. As can be seen in Figure 4.22 and Table 4.3, the relationship between the operating acceleration and the off-axis force, which was modeled using the least squares method, is in good agreement with the measurement results. Also, the analysis results above are in good agreement with the above-described phenomenon, which relates the off-axis force and the change in the operating acceleration. It is expected that this analysis can also be used in applications where the off-axis force is greater than μN level.

TABLE 4.3. Summary of three experiments and calculations.

	Experiment 1 (Figure 4.18)	Experiment 2 (Figure 4.19 & 4.20)	Experiment 3 (Figure 4.21)
Angular acceleration (deg/s^2)	117.462	877.723	1744.123
Tangential force (μN)	0.1355	1.0124	2.0117
Simulated $\hat{z}$-axis displacement (μm)	0.0153	0.1145	0.2275
Narrowed initial gap (μm)	6.3747	6.2755	6.1625
Operating acceleration (modeled) (g)	6.13250	5.93350	5.70672
Operating acceleration (observed) (g)	6.18182	5.84091	5.75000
Error (%)	0.79779	-1.5853	0.75263

4.4. Heating test

To verify the thermal stability of the fabricated switch, we heated the switch on the hot plate. The temperature was elevated up to 80 °C and the process time was 6 hours. After the heating, the switch was electrostatically operated. The heated switch operated normally and this is natural result because the heat treatment is carried out at 340 °C for 4 hours at the last step of fabrication process. This annealing process is proceeded to lower the resistance between aluminum and silicon interface. Figure 4.23 shows (a) optical images of the bottom of the proof mass and (b) top of the signal line after the switch was annealed at 340 °C for 4 hours. No trace of deformation was found in the gold pattern on the silicon side or on the glass side.

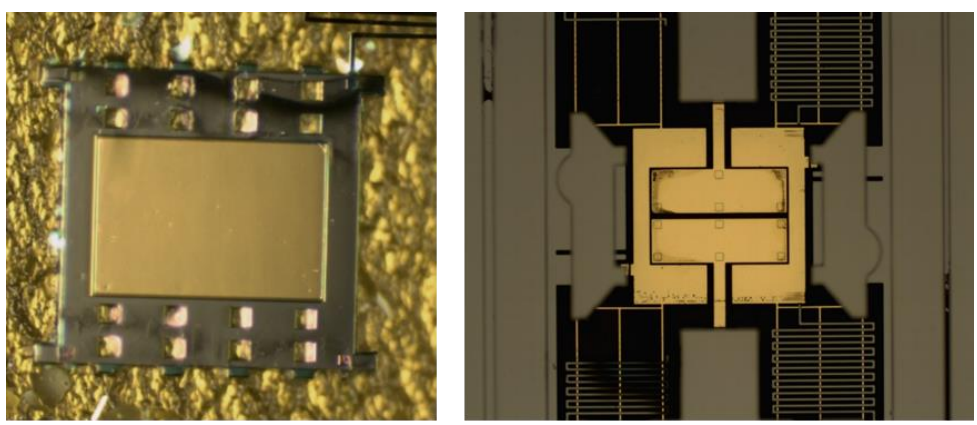

(a) (b)

Figure 4.23. (a) Optical image of the bottom of the proof mass and (b) signal lines on base glass substrate after annealing process (340°C for 4 hours).

4.5. Sealing test

In order to confirm the degree of sealing, leak tests shown in MIL-STD-883E was referred. The method 1014.9, of which its purpose is to determine the effectiveness of the seal (hermeticity) of microelectronic and semiconductor devices, was used. Condition D method (penetrant dye gross leak) was used for gross leak test and condition A method (tracer gas helium fine leak) was used for fine leak test method. If large leak path exists in the device, the helium gas would be released rapidly during the time in which the device is being moved from the helium bomb chamber to the detector chamber. In this case, helium may not be detected by the detector. Therefore, the gross leak test was carried out first to confirm that there is no large leak path in the sample. Figure 4.24 shows the test schematic of penetrant dye test and the experimental scenes.

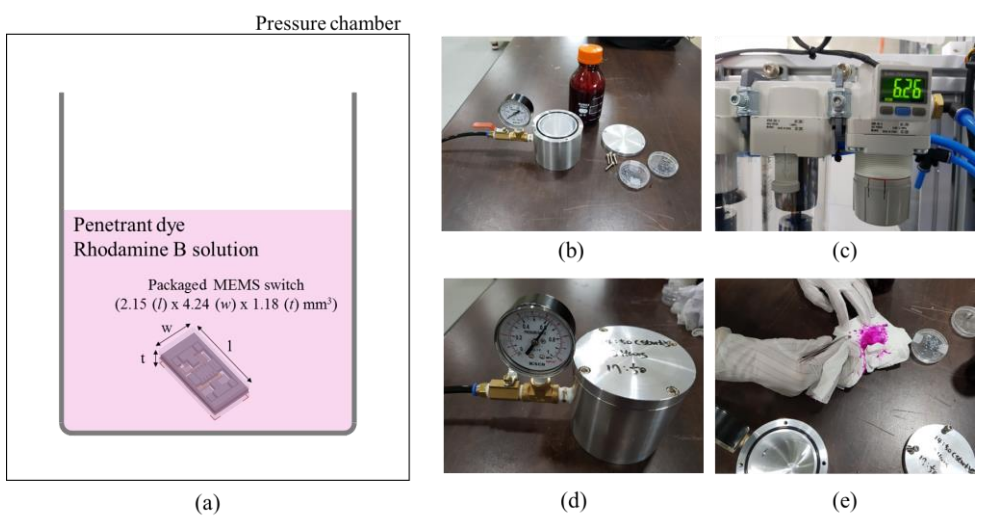

Figure 4.24. (a) Schematic of penetrant dye gross leak test and experimental scenes: (b) experiment preparation, (c) pressurization, (d) maintain for 3 hours, and (e) taking back the samples.

Rhodamine B was used as a penetrant dye and the inside of the pressure chamber was pressurized to 105 psia (or 90 psi or 0.62 MPa, equivalently). The pressurized environment was maintained for 3 hours. After then, the tested samples were cleaned and examined under the UV light source. Figure 4.25 shows a fluorescence images of untested, tested / uncleaned, and tested / cleaned samples, respectively. As can be seen in the figure, the samples that were put into the penetrant dye test showed a clear fluorescence response. On the other hand, the samples that were not put into the experiment and the samples that were cleaned after the experiment showed no fluorescence reaction. The total of number of 10 samples were tested, none of which failed the gross leak test.

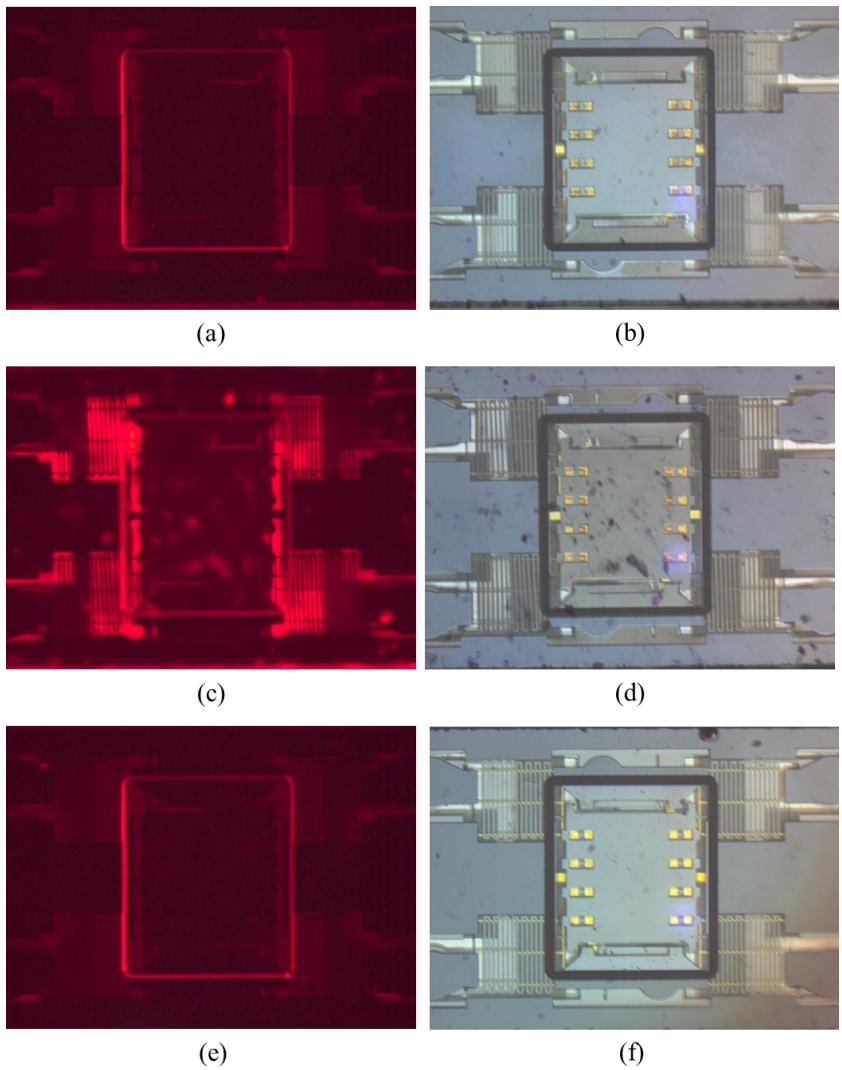

Figure 4.25. Fluorescence and optical images of ((a) and (b)) untested, ((c) and (d)) tested / uncleaned, and ((e) and (f)) tested / cleaned samples, respectively.

For the samples undergone the gross leak test, helium leak test was carried out. Figure 4.26 shows the test schematic of helium leak test and Figure 4.27 shows the experimental scenes. The helium chamber was pressurized up to 75 psia (60 psi or 0.41 MPa, equivalently). The pressurized environment was maintained for 2 hours. After then, the helium-pressurized samples were moved to helium detection chamber. For detection of helium, mass spectrometer (HELIOT 901W1 (ULVAC)) was used.

The helium detecting pressure was set below 0.4 Pa and all the samples (10 ea.) passed the fine leak test as they showed helium leak rates less than the reject limit shown in MIL-STD-883E, which is 5.8×10^{-8} atm cc/s He. The helium leak test results of 10 samples are plotted in Figure 4.28. The average and standard deviation of the helium leak rates of 10 samples were 1.78×10^{-8} atm cc/s He and 5.65×10^{-9} atm cc/s He, respectively. The author would like to show thank to TTASKO, Si-heung si, Korea, for helping the sealing tests.

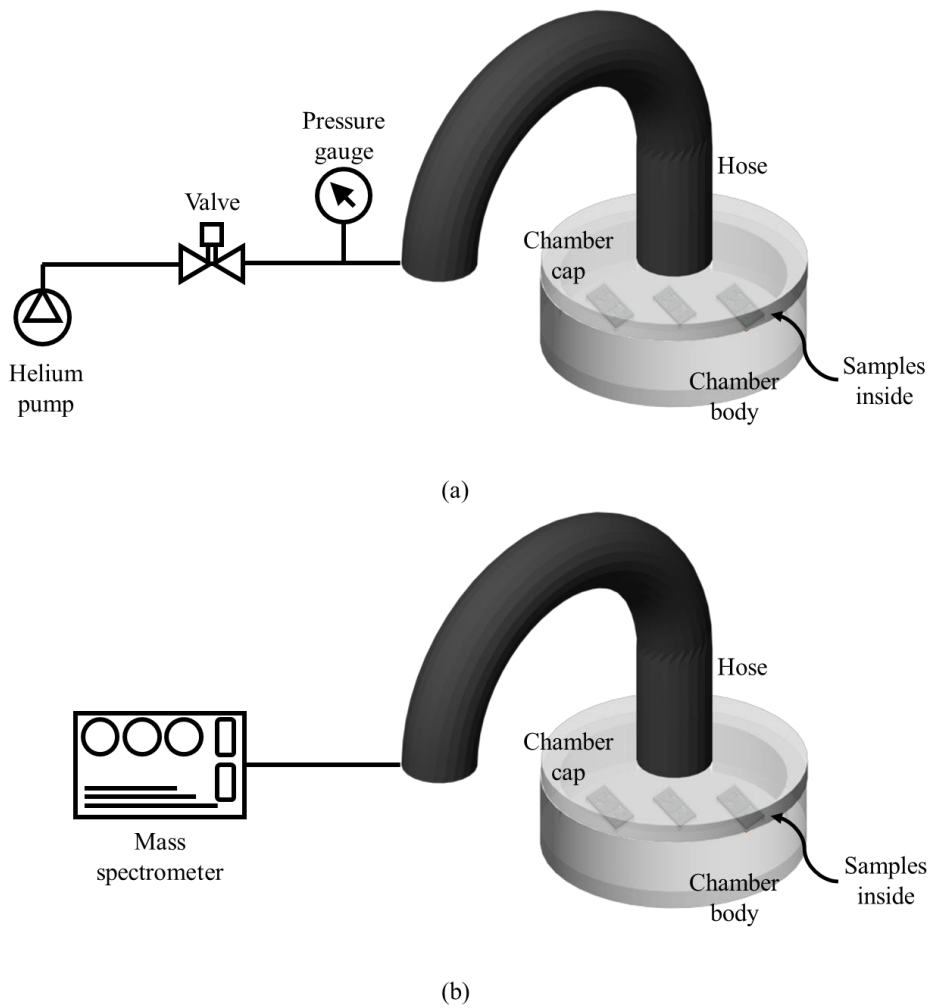

Figure 4.26. Schematic of the helium leak test: (a) helium bombing & maintaining pressure (valve) and (b) helium leak detecting using mass spectrometer.

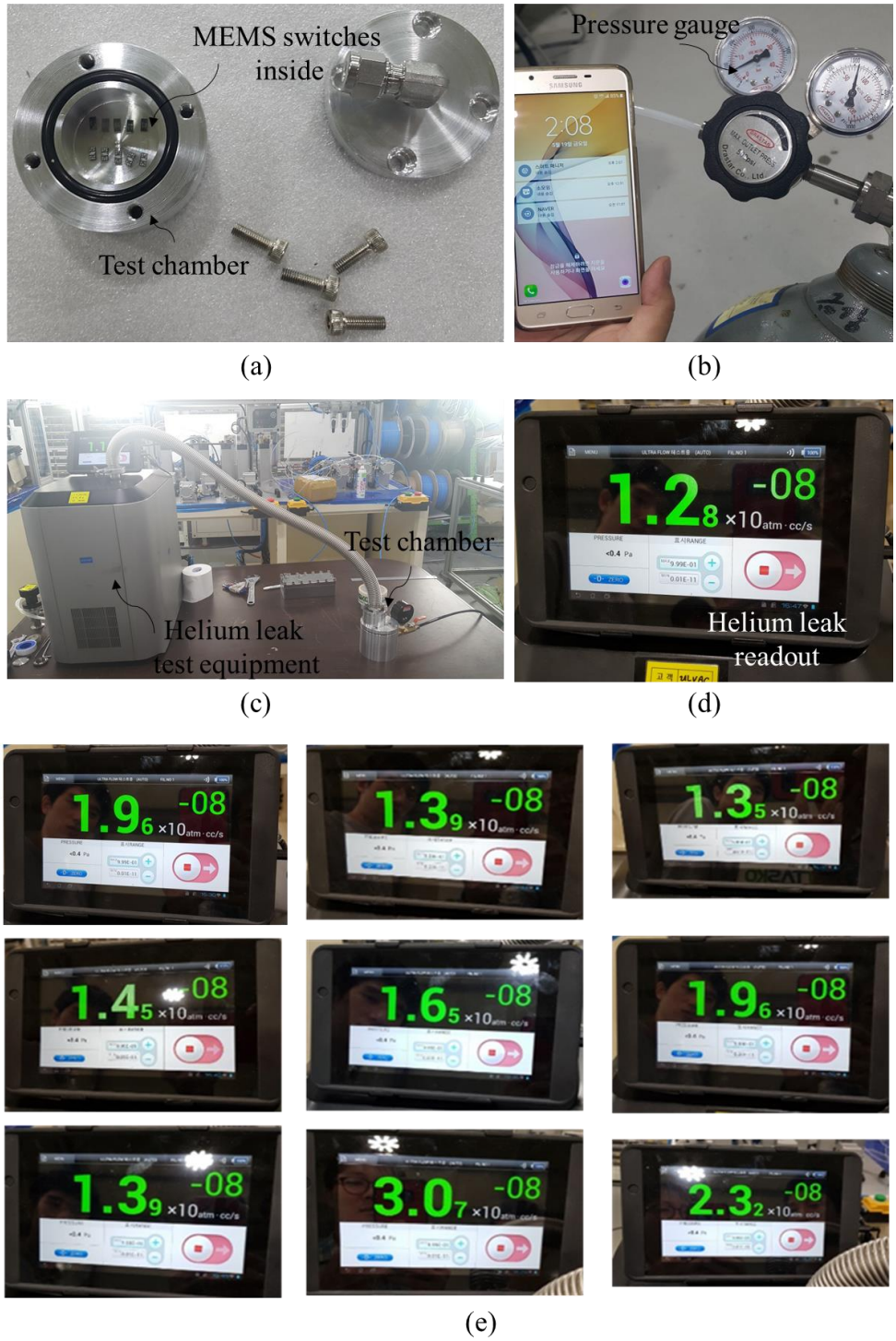

Figure 4.27. Experimental scenes of helium leak test: (a) experiment preparation, (b) pressurization and maintenance, (c) helium detection, (d) measured helium leak rate, and (e) results of the rest 9 samples.

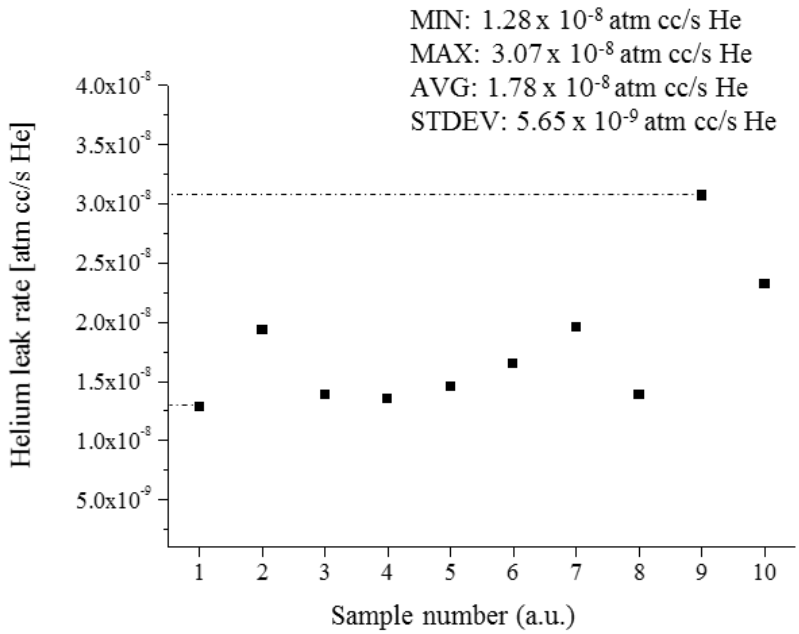

Figure 4.28. Helium leak test results of the tested 10 samples.

4.6. High-g test & drop impact test

The circuit shown in Figure 4.14 was reconstructed and the high-g experiment was conducted using a spin coater. Table 4.4 shows detailed setup values used in the test. RPM was raised to 2320 in 1 s and maintained for 10 s. For high-g test, acceleration of approximately 300 g was applied in sequence to $\pm\hat{x}$-, $\pm\hat{y}$-, and $\pm\hat{z}$-axes, in sequence, respectively. Before and after the spinning, the operation voltage and the resistance of the switch were changed from 8.36 V to 8.41 V (0.6% increase) and 70.65 Ω to 66.21 Ω (6.69% decrease), respectively.

TABLE 4.4. Setup values used in the high-g test.

Parts	Symbol	Quantity	Value
Sensing out circuitry	$V_{sensing}$	Sensing voltage	5.08 V
	R_{load}	Load resistance	985 Ω
Rotation-table	r	Radius of revolution	0.05 m
	α	Angular acceleration	242.95 rad/s^2
	RPM	Rotation per minute	2320
	t_r	Rising time of acceleration	1 s
	$F_{c,fin}$	Final centrifugal force	0.907 mN
	-	According final g-level	300.84

Figure 4.29 shows the drop test schematic of a packaged micro-machined system [61]. The equivalent acceleration applied to the MEMS acceleration switch during the drop collision is calculated as shown in Equation 4.10.

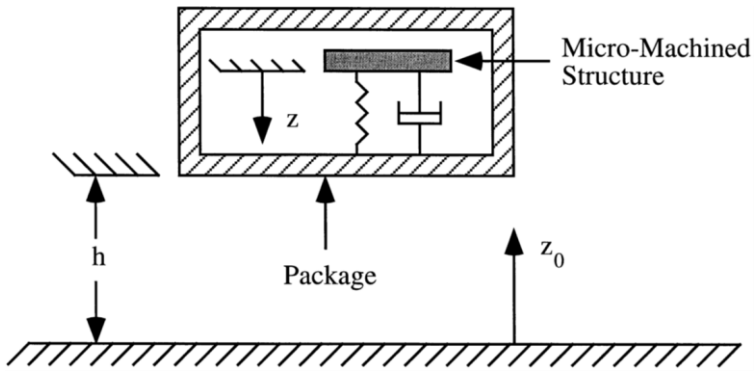

Figure 4.29. Schematic of drop impact test for a packaged micro-machined system [61].

$$\bar{a} \equiv \frac{a}{g} = \sqrt{\frac{kh}{2mg}}\, d_r(\zeta, r) \qquad \text{(Equation 4.10)}$$

where $\bar{a},\ g,\ h,\ m,\ k,\ r,\ \zeta$ are the equivalent acceleration in g, the gravitational acceleration, drop height, mass of the proof mass, spring constant, coefficient of restitution, and damping ratio, respectively. In Equation 4.10, $d_r(\zeta, r)$ is given by Equation 4.11 according to the value of the damping ratio (ζ):

$$d_r(\zeta, r) = \begin{cases} \dfrac{2(1+r)e^{\frac{-\zeta arcsin\sqrt{1-\zeta^2}}{\sqrt{1-\zeta^2}}}}{1+e^{-\frac{\zeta\pi}{\sqrt{1-\zeta^2}}}} & for\ \zeta < 1 \\ \dfrac{2(1+r)}{e} & for\ \zeta = 1 \\ 2(1+r)e^{\frac{-\zeta arcsinh\sqrt{\zeta^2-1}}{\sqrt{\zeta^2-1}}} & for\ \zeta > 1 \end{cases} \qquad \text{(Equation 4.11)}$$

Assuming the fabricated switch has damping ratio of 0.1 and the coefficient of restitution to be 0.5, impact characteristic (i.e., equivalent acceleration) according to

the drop height can be obtained as shown in Figure 4.30. Table 4.5 shows the calculation values for this test. For the developed switch, the equivalent acceleration generated by 1 m drop was calculated to be about 1100 g.

TABLE 4.5. Calculation values for drop impact test.

Symbol	Quantity	Value
$\bar{a}$	Equivalent acceleration in g	-
g	The gravitational acceleration	9.80665 m/s^2
m	The proof mass	3.0738E-07 kg
k	Spring constant	3.19 N/m
r	Coefficient of restitution	0.5
ζ	Damping ratio	0.1
Q-factor	Q-factor	5

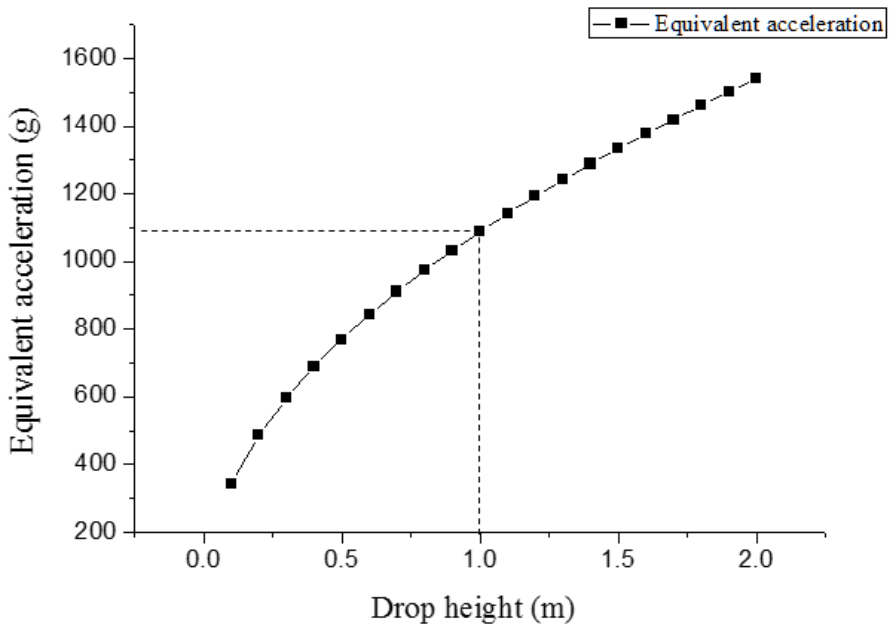

Figure 4.30. Drop heights and equivalent accelerations in g-level (ξ=0.01, CoR=0.5).

The switch was dropped at the height of 1 m to ensure durability against shocks over 1000 g. The switch was dropped three times to ensure the effectiveness of the impact test results. After that, the dropped switch was mounted on the rotation-table and the rotation-table experiment was performed. Figure 4.31 shows the result of the drop impact test using the sample used in the previous chapter 4.3. The switch operated at the same acceleration value at which it operated previously, and the impact resistance of the switch was confirmed. Through the high-g test and the drop impact test, it was confirmed that the displacement-restricting structures installed in all directions of the proof mass safely protect the switch from the external impacts. Table 4.6 summarizes overall environmental test result of the developed MEMS acceleration switch in this study. Comparison against the pre-reported low-g MEMS switches are also provided to show that the MEMS acceleration switch developed in this study is the first low-g (below 10 g) MEMS acceleration switch of which its

thermal, sealing, high-g, and impact characteristics were successfully characterized altogether.

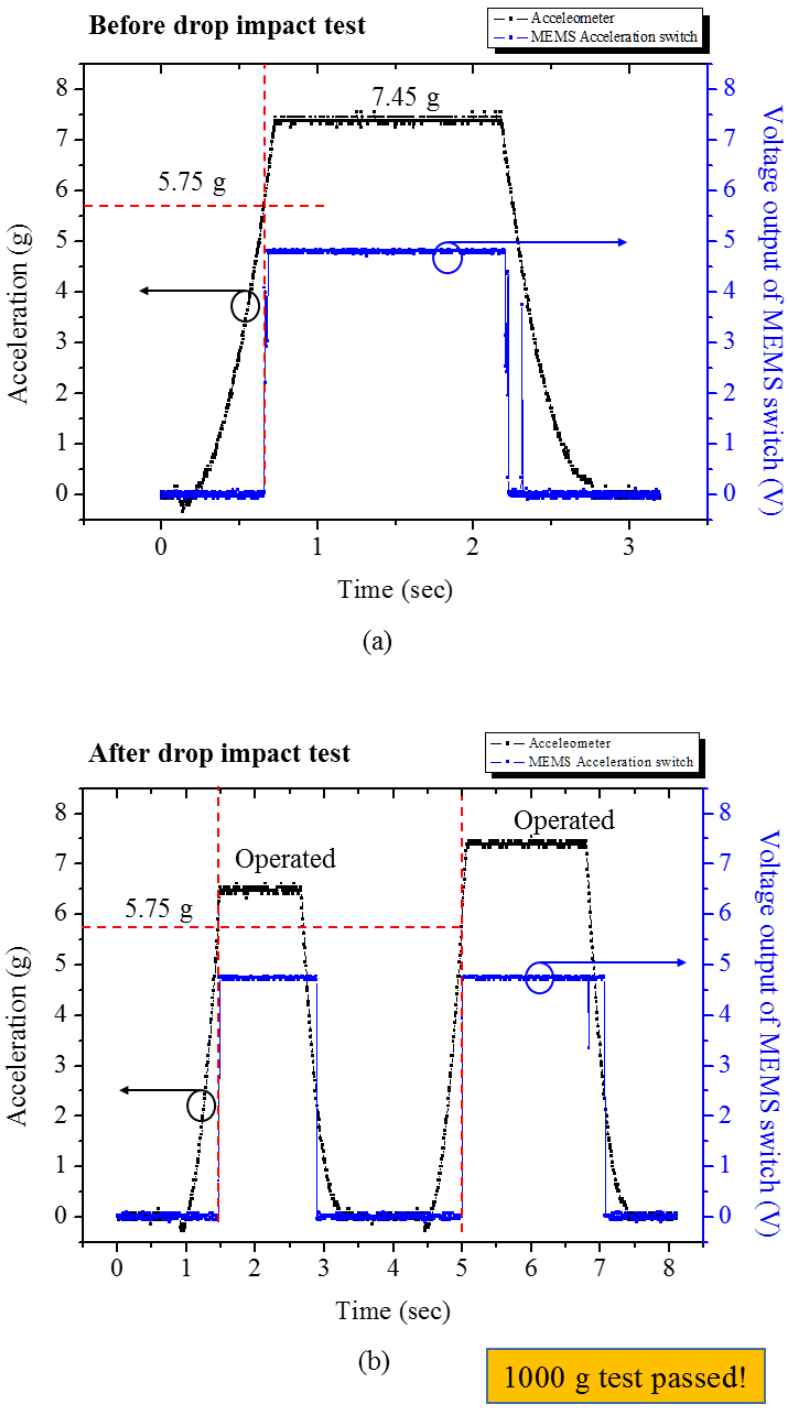

Figure 4.31. Rotation-table experiment results: (a) before and (b) after drop-impact test over 1000 g.

Table 4.6. Comparison between reported low-g MEMS switches and the switch developed in this study.

	[18] Wang et al., 2013	[33] Kim et al., 2014	[45] Xiong et al., 2015	This study 2017
Threshold acceleration	32 g	2.0 ~ 17.25 g	7.42 g	≈ 6.5 g
Operating direction	Horizontal	Horizontal	Vertical	Vertical
Structural material	Ni (electroplated)	Silicon	Silicon	Silicon
Contact surface	Ni (PR mold)	Silicon (DRIE)	Au	Au
Self-test capability (electrical)	X	O	X	O
Displacement -restricting structure	O	X	X	O
Stress-free structure	NA	NA	NA	O
Lifecycle test	> 1,000 cycles	NA	NA	> 10,000 cycles
Thermal stability	NA	NA	NA	O MIL-STD-810G (80 ℃ storage, hot temperature)
Sealing test	NA (not certain on the wafer-level package)	NA (unpackaged)	NA (unpackaged)	O MIL-STD-883E Condition D (gross) & A(fine)

High-g test result	X	NA	NA	O (300 g for all directions)
Impact test	O (up to 800 g)	NA	NA	O (> 1,000 g)
Notes	- Weak to thermal problems - Stress control issues - Difficult to control contact surface	- Operation voltage needed for threshold tuning - Difficult to control contact surface	- Double-BOX SOI - Complex fabrication - Vulnerable to off-axis impact - No stopper structure	

5. Conclusion

In this paper, low-g MEMS acceleration switch with threshold acceleration below 10 g was developed. The structural material of the switch is single-crystalline silicon, which has high thermal stability and is helpful to obtain stress-free structure. To attain uniform contact characteristic, vertical operation type is selected. Also, operation electrode and displacement-restricting structures were added for electrical self-test capability and high impact resistance, respectively. In the design of switch, serpentine spring was used for low spring constant with small footprint. Theoretical analyses and simulations were carried out to confirm the force-displacement-stress and modal characteristics of the proposed switch. One SOI (silicon-on-insulator) and two glass substrates were used in the fabrication process and the issues were addressed in detail. As the results of the fabrication, the average proof mass, initial gap, and the spring constant of the fabricated switches were 307.38 μg, 6.39 μm, and 3.29 N/m, respectively. To show that the fabricated switch does not suffer from stress problems, height profiles of the free-hanging proof masses were measured. From the results, the tilting angles of the proof mass in $\hat{x}$- and $\hat{y}$-axes were less than 0.05°. The calculation result revealed that the change in the operating acceleration due to this tilting is about 2%. The reason for tilting is thought to be fabrication errors in spring width and thickness.

For fabricated samples, electrostatic operation tests were carried out for 32 samples. In this experiment, voltage was increased by 1 V and over 40% of the samples operated at the voltage of 7 V. The effect of the gravitational acceleration was considered in the calculation and it was revealed that the fabricated switches have operating accelerations similar to the fabricated value. The contact resistance

decreased with the increase of the contact force and the minimum contact resistance was estimated to be about 8.5 Ω when the contact force was 284 μN. No further decrease was observed and reason for high contact resistance is thought to be the effect of PERs (post etch residues) generated upon the contact surface during the 2nd DRIE process. After that, lifecycle test was carried out to show that the switch could repeat operation over 10,000 cycles. In the lifecycle test, contact force of 55 μN was applied and contact resistance was saturated at about 150 Ω as the operation cycles exceed 4,000. The response time of the switch was measured with oscilloscope and revealed to be shorter than 1.2 ms. The fabricated switch was tested in the rotation-table and the switch operated at 6.61 g. The error between the calculated (6.98 g) and the measured threshold acceleration (6.61 g) was 5.3 %. Error analysis was carried out in the consideration of tangential force generated during the rotation-table experiment. From the experimental values, the tangential force was calculated as 2.091 μN and the resulting reduction in the initial switching gap was simulated as 0.236 μm, which would reduce the operating acceleration of the switch. The reduced threshold acceleration thus was estimated to be 6.512 g, which agrees well with the measured threshold acceleration value of 6.61 g. To validate the effect of the off-axis force on the operating acceleration, rotation-table experiments that generate different tangential forces were carried out. The tangential forces were calculated from the value of the angular acceleration when the switch operated. The least squares method was used to model the relationship between the error due to the off-axis force and the operating acceleration of the switch. As a result of the analysis, it was first verified that the off-axis force would change the operating acceleration of the low-g MEMS acceleration switch.

Environmental tests were carried out next. Firstly, the fabricated switches were

heated at 80 °C over 6 hours on the hot plate and the tested switches successfully operated after heating test. After that, sealing tests were carried out for both gross and fine leak test. Penetrant dye test using Rhodamine B solution was carried out for gross leak test and tracer gas helium leak test was carried out for fine leak test. In both of the test, 10 samples were put into the experiments and every sample passed both of the tests, showing no traces of infiltration and helium leak rates lower than 5.8×10^{-8} atm cc/s He. From the leak test results, it was shown that the fabricated switches are hermetically packaged. The sealing test results satisfy the sealing standards shown in MIL-STD-883E method D and A. To verify the high-g durability and the impact resistance, high-g test and drop impact tests were performed. As a result of the high-g test, the switch has successfully sustained high acceleration of 300 g in the $\pm\hat{x}$-, $\pm\hat{y}$-, and $\pm\hat{z}$-axes. The drop impact test showed that the switch could operate normally even after receiving high shock as high as 1000 g. The acceleration switch developed throughout this study is the first low-g (below 10 g) MEMS acceleration switch of which its heat, hermeticity, high-g, and impact resistance characteristics were successfully verified altogether. The author believes that the switch developed in this study has the best potential to be applied to the safety arm unit compared to the others reported so far.

References

[1] L. Zimmermann, J. P. Ebersohl, F. Le Hung, J. Berry, F. Baillieu, P. Rey, B. Diem, S. Renard, and P. Caillat, "Airbag application: a microsystem including a silicon capacitive accelerometer, CMOS switched capacitor electronics and true self-test capability," Sensors and Actuators A: Physical, vol. 46, pp. 190-195, 1995.

[2] M. Mori, "Fast response micro-safing sensor for air bag systems," SAE Technical Paper 0148-7191, 1999.

[3] T. Matsunaga and M. Esashi, "Acceleration switch with extended holding time using squeeze film effect for side airbag systems," Sensors and Actuators A: Physical, vol. 100, pp. 10-17, 2002.

[4] D. R. Ciarlo, "A latching accelerometer fabricated by the anisotropic etching of (110) oriented silicon wafers," Journal of Micromechanics and Microengineering, vol. 2, p. 10, 1992.

[5] C. Özgen, "A TACTICAL GRADE MEMS ACCELEROMETER," MIDDLE EAST TECHNICAL UNIVERSITY, 2010.

[6] A. Ongkodjojo and F. E. Tay, "Optimized design of a micromachined G-switch based on contactless configuration for health care applications," in Journal of Physics: Conference Series, 2006, p. 1044.

[7] L. Currano, C. Becker, G. Smith, B. Isaacson, and C. Morris, "3-axis acceleration switch for traumatic brain injury early warning," in Micro Electro Mechanical Systems (MEMS), 2012 IEEE 25th International Conference on, 2012, pp. 484-487.

[8] R. S. Johnston, L. F. Dietlein, C. A. Berry, J. F. Parker, and V. West, "Biomedical results of Apollo," 1975.

[9] M. Voshell, "High acceleration and the human body," 28th November, 2004.

[10] H. C. Ohanian and J. Market, "Physics for Engineers and Scientists Vol. 1," ed: McGraw Hill, 2007.

[11] D. ReVelle and W. Edwards, "Stardust—An artificial, low-velocity “meteor” fall and recovery: 15 January 2006," Meteoritics & Planetary Science, vol. 42, pp. 271-299, 2007.

[12] G. Bibel, Beyond the black box: the forensics of airplane crashes: JHU Press, 2008.

[13] C. Y. Huan, H. Jaafar, and N. A. M. Yunus, "Classification on MEMS Accelerometer and Device Application," in The Second International Conference on Technological Advances in Electrical, Electronics and Computer Engineering (TAEECE2014), 2014, pp. 215-225.

[14] (25 May). WD® SHIPS SLIM, ENERGY-EFFICIENT HARD DRIVE FOR ULTRABOOK™ DEVICES. Available: https://www.wdc.com/about-wd/newsroom/press-room/2012-04-11-wd-ships-hard-drive-for-ultrabook-devices.html

[15] E. F. Taylor and J. A. Wheeler, Spacetime physics: Macmillan, 1992.

[16] N. Yazdi, F. Ayazi, and K. Najafi, "Micromachined inertial sensors," Proceedings of the IEEE, vol. 86, pp. 1640-1659, 1998.

[17] L. J. Currano, S. Bauman, W. Churaman, M. Peckerar, J. Wienke, S. Kim, M. Yu, and B. Balachandran, "Latching ultra-low power MEMS shock sensors for acceleration monitoring," Sensors and Actuators A: Physical, vol. 147, pp. 490-497, 2008.

[18] Y. Wang, Q. Feng, Y. Wang, W. Chen, Z. Wang, G. Ding, and X. Zhao, "The design, simulation and fabrication of a novel horizontal sensitive inertial micro-switch with low g value based on MEMS micromachining technology," Journal of Micromechanics and Microengineering, vol. 23, p. 105013, 2013.

[19] R. J. H. Mcardle Edward P, "Safety arming device for explosive missiles," ed: Google Patents, 1960.

[20] S.-J. Oh, S.-G. Jang, and H.-S. Cha, "Research on the Ejection Gas Generator to Improve Ejecting Performance," Journal of the Korean Society for Aeronautical & Space Sciences, vol. 41, pp. 383-390, 2013.

[21] H.-S. Cha, S.-J. Oh, and Y.-J. Lee, "A Study for Reduction of Ignition Peak Pressure of Gas Generator," in Proceedings of the Korean Society of Propulsion Engineers Conference, 2010.

[22] M. T. Cagle, "Historical Monograph: Development, Production, and Deployment of the Nike Ajax Guided Missile System, 1945–1959," US Army Ordnance Missile Command, Redstone Arsenal, AL, US, 1959.

[23] T. W. Eagles, "Optimal trajectories for low altitude, high acceleration ICBM interception," 1968.

[24] R. L. Garwin, "Technical Aspects of Ballistic Missile Defense," in APS Forum on Physics and Society, 1999.

[25] (2016, July, 2nd). What is the acceleration of a Patriot missile? Available: https://www.quora.com/What-is-the-acceleration-of-a-Patriot-missile

[26] N. M. Barbour, "Inertial navigation sensors," DTIC Document2010.

[27] K. Froyum, S. Goepfert, J. Henrickson, and J. Thorland, "Honeywell micro electro mechanical systems (MEMS) inertial measurement unit (IMU)," in

Position Location and Navigation Symposium (PLANS), 2012 IEEE/ION, 2012, pp. 831-836.

[28] W.-r. Nie, Z.-w. Xi, W.-q. Xue, and Z.-j. Zhou, "Study on inertial response performance of a micro electrical switch for fuze," Defence Technology, vol. 9, pp. 187-192, 2013.

[29] C. H. Robinson, R. H. Wood, M. R. Gelak, T. Q. Hoang, and G. L. Smith, "Ultra-miniature electro-mechanical safety and arming device," ed: Google Patents, 2013.

[30] C. H. Robinson, R. H. Wood, A. Bayba, and D. Hollingsworth, "MEMS safety and arming device for OICW," DTIC Document2001.

[31] L.-j. NIU, K.-l. SHI, X. ZHAO, and R. ZHAI, "Application of MEMS on Fuzes [J]," Journal of Detection & Control, vol. 6, p. 014, 2008.

[32] S. Michaelis, M. Wycisk, and J. Binder, "Additive electroplating technology as a post-CMOS process for the production of MEMS acceleration-threshold switches for transportation applications," Journal of Micromechanics and Microengineering, vol. 10, p. 120, 2000.

[33] H. Kim, Y.-H. Jang, Y.-K. Kim, and J.-M. Kim, "MEMS acceleration switch with bi-directionally tunable threshold," Sensors and Actuators A: Physical, vol. 208, pp. 120-129, 2014.

[34] S. Jang, J. Hwang, and Y.-K. Kim, "Anti-stiction method for mems acceleration switch employing an additional mass structure," in Micro Electro Mechanical Systems (MEMS), 2016 IEEE 29th International Conference on, 2016, pp. 950-953.

[35] W. D. Frobenius, S. A. Zeitman, M. H. White, D. D. O'Sullivan, and R. G. Hamel, "Microminiature ganged threshold accelerometers compatible with

integrated circuit technology," IEEE Transactions on electron devices, vol. 19, pp. 37-40, 1972.

[36] T. Tønnesen, O. Lüdtke, J. Noetzel, J. Binder, and G. Mader, "Simulation, design and fabrication of electroplated acceleration switches," Journal of Micromechanics and Microengineering, vol. 7, p. 237, 1997.

[37] M. Wycisk, J. Binder, S. Michaelis, and H.-J. Timme, "New sensor-on-chip technology for micromechanical acceleration-threshold switches," in Asia Pacific Symposium on Microelectronics and MEMS, 1999, pp. 112-120.

[38] H. Cai, G. Ding, Z. Yang, Z. Su, J. Zhou, and H. Wang, "Design, simulation and fabrication of a novel contact-enhanced MEMS inertial switch with a movable contact point," Journal of Micromechanics and Microengineering, vol. 18, p. 115033, 2008.

[39] Y. Gerson, D. Schreiber, H. Grau, and S. Krylov, "Meso scale MEMS inertial switch fabricated using an electroplated metal-on-insulator process," Journal of Micromechanics and Microengineering, vol. 24, p. 025008, 2014.

[40] Q. Zhang, Z. Yang, Q. Xu, Y. Wang, G. Ding, and X. Zhao, "Design and fabrication of a laterally-driven inertial micro-switch with multi-directional constraint structures for lowering off-axis sensitivity," Journal of Micromechanics and Microengineering, vol. 26, p. 055008, 2016.

[41] Q. Xu, Z.-Q. Yang, B. Fu, Y.-P. Bao, H. Wu, Y.-N. Sun, M.-Y. Zhao, J. Li, G.-F. Ding, and X.-L. Zhao, "Design and Optimization of a Stationary Electrode in a Vertically-Driven MEMS Inertial Switch for Extending Contact Duration," Sensors, vol. 17, p. 527, 2017.

[42] J. S. Go, Y.-H. Cho, B. M. Kwak, and K. Park, "Snapping microswitches with adjustable acceleration threshold," Sensors and Actuators A: Physical, vol. 54, pp. 579-583, 1996.

[43] Z. Guo, Q. Zhao, L. Lin, H. Ding, X. Liu, J. Cui, Z. Yang, H. Xie, and G. Yan, "An acceleration switch with a robust latching mechanism and cylindrical contacts," Journal of Micromechanics and Microengineering, vol. 20, p. 055006, 2010.

[44] G. M. Siouris, Missile guidance and control systems: Springer Science & Business Media, 2004.

[45] Z. Xiong, F. Zhang, Y. Pu, B. Tang, J. Yang, and C. Wang, "Silicon-based, low-g microelectromechanical systems inertial switch for linear acceleration sensing application," Micro & Nano Letters, vol. 10, pp. 347-350, 2015.

[46] M. K. Thompson, "MIL-STD-810G environmental engineering considerations and laboratory tests," ed: USA: Department of Defense USA Press, 2000: 8-10.

[47] K. E. Petersen, "Silicon as a mechanical material," Proceedings of the IEEE, vol. 70, pp. 420-457, 1982.

[48] B. Persson, O. Albohr, U. Tartaglino, A. Volokitin, and E. Tosatti, "On the nature of surface roughness with application to contact mechanics, sealing, rubber friction and adhesion," Journal of Physics: Condensed Matter, vol. 17, p. R1, 2004.

[49] N. McGruer, G. Adams, L. Chen, Z. Guo, and Y. Du, "Mechanical, thermal, and material influences on Ohmic-contact-type MEMS switch operation," in Micro Electro Mechanical Systems, 2006. MEMS 2006 Istanbul. 19th IEEE International Conference on, 2006, pp. 230-233.

[50] O. Rezvanian, M. Zikry, C. Brown, and J. Krim, "Surface roughness, asperity contact and gold RF MEMS switch behavior," Journal of Micromechanics and Microengineering, vol. 17, p. 2006, 2007.

[51] S. S. Rao and F. F. Yap, Mechanical vibrations vol. 4: Prentice Hall Upper Saddle River, 2011.

[52] R. Tirumala and D. B. Go, "An analytical formulation for the modified Paschen's curve," Applied Physics Letters, vol. 97, p. 151502, 2010.

[53] G. K. Fedder, "Simulation of microelectromechanical systems," University of California at Berkeley, 1994.

[54] L. Mol, L. Rocha, E. Cretu, and R. Wolffenbuttel, "Squeezed film damping measurements on a parallel-plate MEMS in the free molecule regime," Journal of Micromechanics and Microengineering, vol. 19, p. 074021, 2009.

[55] J. A. Collins, Failure of materials in mechanical design: analysis, prediction, prevention: John Wiley & Sons, 1993.

[56] K. Sooriakumar, W. Chan, T. S. Savage, and C. Fugate, "A comparative study of wet vs. dry isotropic etch to strengthen silicon micro-machined pressure sensor," Electrochem. Soc. Proc, vol. 27, pp. 259-265, 1995.

[57] C. Howard, "Recent developments in submarine vibration isolation and noise control," in Proceedings of the 1st Submarine Science Technology and Engineering Conference, 2011.

[58] S. D. Senturia, Microsystem design: Springer Science & Business Media, 2007.

[59] T. Maruyama, N. Fujiwara, K.-i. Siozawa, and M. Yoneda, "Analysis of fluorocarbon deposition during SiO2 etching," Japanese journal of applied physics, vol. 35, p. 2463, 1996.

[60] G. R. Fowles and G. L. Cassiday, Analytical mechanics: Saunders College, 1999.

[61] G. Li and F. Shemansky, "Drop test and analysis on micro-machined structures," Sensors and Actuators A: Physical, vol. 85, pp. 280-286, 2000.

Abstract (Korean)

전자기파 잡음에 영향을 받는 가속도계와 달리 가속도 스위치는 기계적 힘에 의해서만 동작한다. 따라서 안전이 중요한 군사 응용들에서는 가속도 스위치를 가속도계와 함께 사용하여 입력 가속도의 진위를 판단할 수 있다. 이러한 군사 응용들에 사용되기 위한 가속도 스위치는 열, 응력 등의 문제를 가지고 있지 않아 균일한 동작 특성을 가져야 하며, 외부 환경 요소로부터 영향을 받지 않도록 밀봉되어야 한다. 또한, 높은 가속도 입력이나 충격에 파손되지 않아야 군사 응용에 적합하게 사용될 수 있다. 본 연구는 미사일의 냉각 발사 체계(Cold-launching system)에서 사용되는 10 g 수준의 사출 가속도에 동작할 수 있는 점화안전장치용 MEMS 가속도 스위치를 개발하였다. 개발된 스위치는 높은 열 안정성과 스트레스 없는 구조를 구현하기 위하여 단결정 실리콘을 구조재로 사용하였으며, 스위치의 동작 특성에 큰 영향을 미치는 접촉 표면의 개선에 유리하도록 수직 구동형 방식을 채택하였다. 제안된 스위치의 공정은 하나의 SOI (Silicon-on-Insulator) 기판과 베이스 및 패키지용으로 사용될 두 장의 유리 기판 공정으로 구성된다. 스위치는 최종적으로 상압 상태에서 양극 접합 공정을 통해 접합되고 마지막으로 다이싱 공정을 통해 개별화 된다. 개별화된 단일 스위치의 크기는 2,150 x 4,240 x 1,180 μm^3 의 크기를 가진다. 본 연구를 통해 개발된 스위치는 관성 질량의 과도한 변위로 인한 스프링의 파손을 막기 위하여 모든 방향으로 변위 제한 구조를 가지고 있으며, 정전 구동 전극을 내부에 가지고 있어 높은 신뢰도가 요구되는 군사 응용에 적용되기 전 정전 반복 구동 실험을 통하여 동작 특성을 확인할 수 있다. 본 연구에서 설계된 공정 과정을 통해 제작된 스위치들은 307.38 μg, 6.39 μm, 그리고 3.29 N/m의 평균 관성 질량, 초기 간격 및 스프링 상수를 가지는 것으로 나타났다. 3차원 프로파일러 장비를 이용하여 관성 질량의 초기 자세를 확인하였으며, 측정 결과 제작된 스위치의 스프링은 응력 문제를 겪지 않음을 확인하였다. 정전

구동 실험을 통하여 스위치의 풀인 전압과 저항-접촉력 특성을 확인하였으며, 스위치의 최소 접촉 저항은 284 μN의 접촉력에서 8.5 Ω으로 나타났다. 반복 구동 실험 테스트를 또한 진행하였으며, 제작된 스위치는 10,000 이상 실패 현상 없이 반복 구동에 성공하였다. 반복 구동 실험에는 약 55 μN의 접촉력을 사용하였으며 실험 도중 스위치의 접촉 저항은 동작 횟수가 4,000 회를 초과함에 따라 약 150 Ω 수준으로 포화되었다. 제작된 스위치의 응답 속도는 Step input에 대해 1.2 ms보다 짧은 것으로 측정되었다. 제작된 스위치의 열 내구도를 확인하기 위하여 스위치를 80 ° C 에서 6 시간 동안 가열한 후 반복 구동 실험을 수행하였으며, 가열된 스위치는 200 회 이상 구동에 성공하였다. 이는 스위치 제작의 마지막 단계에서 4시간동안 340° C 의 어닐링 (Annealing) 공정을 거치게 되기 때문에 당연한 결과이다. 회전 테이블을 이용한 가속도 인가 실험에서 스위치는 6.61 g에서 작동하였다. 이 값은 스위치의 제작 치수들 측정하여 계산한 임계 가속도와 비교 분석되었고, 회전 테이블에서 발생하는 접선 가속도의 영향을 고려한 오차 분석을 수행하였다. 실험값으로부터 관성질량에 접선방향으로 작용하는 힘은 2.091 μN으로 계산되었고, 스위치의 초기 간격이 이에 따라 0.236 μm 감소하게 되는 것으로 전산모사되었다. 이에 따라 감소된 스위치의 임계 가속도는 6.51 g로 추정되었으며, 이는 6.61 g에 측정된 동작 가속도 값과 잘 일치한다. 이 분석의 타당성을 검증하기 위하여 또 다른 스위치를 이용하여 회전 테이블 테스트를 수행하였다. 최소 자승법을 이용하여 타축 방향 입력 힘에 의한 동작 가속도의 변화 양상을 분석하였으며 측정된 가속도 값과 분석을 통해 모델링 된 동작 가속도 값의 오차는 서로 다른 각가속도 (즉 서로 다른 타축 방향 입력 힘) 값에 대하여 잘 일치하였다. 한편, 제작된 스위치의 밀봉 특성을 확인하기 위하여 임의로 선택한 10개의 스위치를 gross 및 fine 실험에 투입하였다. Gross 누출 검사를 위해 Rhodamine B 용액을 이용한 침투 염료 시험을 실시하였으며, Fine 누출 실험을 위해 추적 가스 헬륨 누출 시험을 실시하였다. 투입된 모든 샘플들이 두 테스트 모두를 통과하였으며 헬륨 누출도는 군사 응용에서 0.05 cm^3 보다 작은 패키지

부피를 가지는 소자에 허용하는 한계인 $5.8x10^{-8}$ atm cc/s He보다 낮은 누출도를 보였다. 10개의 샘플들이 보인 헬륨 누출도의 평균과 표준편차는 각각 $1.78x10^{-8}$ atm cc/s He, $5.65x10^{-9}$ atm cc/s He이었다. 또한 스위치에 설치된 변위 제한 구조물의 유효성을 검증하기 위해 고가속(High-g) 시험 및 낙하 충격 시험을 수행하였다. 변위 제한 구조물은 관성질량이 고가속 시험에서 과도한 거리를 이동할 때 스프링에 인가되는 응력에 의해 스프링이 파손되는 것을 방지한다. 또한 낙하 충격 시험에서는 변위제한 구조물이 외부 충격에 의해 관성질량이 가속될 수 있는 거리를 제한함으로써 관성질량과 주변 구조물 사이의 충격에 의한 파손 현상을 방지하게 된다. 고가속 시험에서 제작된 스위치는 ±x, ±y, 그리고 ±z 방향으로의 300 g 입력 가속도를 받은 후에도 성공적으로 동작하였다. 또한 1 m 높이에서의 3회 낙하 충격을 겪은 후에도 동작 전과 같은 입력 가속도 값에서 동작하여 1000 g 이상의 내충격성을 가지고 있는 것으로 나타났다. 최종적으로, 본 연구를 통해 개발된 스위치는 10 g 이하의 낮은 임계가속도를 가지는 MEMS 가속도 스위치들 중 최초로 응력 문제, 열 내구성, 밀봉도 및 내충격 특성을 모두 검증한 스위치임을 확인하였다. 앞서 언급된 환경 실험들은 부분적으로 군사 응용 규격을 만족하며, 이에 본 연구에서 개발된 MEMS 가속도 스위치는 현재까지 보고된 저임계가속도 MEMS 스위치들보다 점화 안전 장치 등의 군사 응용에 사용되기에 가장 적합한 스위치라 할 수 있다.

주요어 : MEMS (Microelectromechanical Systems), Acceleration Switch, Inertial Switch, Low-g, Low Threshold Acceleration, Ignition Safety Device.
학 번 : 2013-30974